AFOSR-TR- 89-0139

(2)

Department of Mechanical and Aerospace Engineering
Rutgers — The State University of New Jersey
New Brunswick, NJ 08903

Report RU-TR-172-MAE-F

Theoretical Investigation of 3-D Shock Wave-Turbulent Boundary Layer Interactions Part VII

Doyle D. Knight

Interim Report for Period 1 October 1987 to 30 September 1988
Approved for Public Release — Distribution Unlimited

Air Force Office of Scientific Research
Building 410
Bolling AFB
Washington, DC 20332

November 1988

SECURITY CLASSIFICATION OF THIS PAGE

REPORT DOCUMENTATION PAGE

1a REPORT SECURITY CLASSIFICATION: Unclassified	1b RESTRICTIVE MARKINGS
2a SECURITY CLASSIFICATION AUTHORITY	3 DISTRIBUTION / AVAILABILITY OF REPORT: Approved for Public Release Distribution Unlimited
2b DECLASSIFICATION / DOWNGRADING SCHEDULE	
4 PERFORMING ORGANIZATION REPORT NUMBER(S): RU-TR-172-MAE-F	5 MONITORING ORGANIZATION REPORT NUMBER(S): AFOSR-TR- 89-0139

6a NAME OF PERFORMING ORGANIZATION: Dept. Mech. Aero. Eng. Rutgers University	6b OFFICE SYMBOL (If applicable)	7a NAME OF MONITORING ORGANIZATION: Air Force Office of Scientific Research
6c ADDRESS (City, State, and ZIP Code): P.O. Box 909, MAE Piscataway, NJ 08855-0909		7b ADDRESS (City, State, and ZIP Code): Building 410 Bolling AFB Washington, DC 20332
8a NAME OF FUNDING / SPONSORING ORGANIZATION: Air Force Off. Scien. Res	8b OFFICE SYMBOL (If applicable): AFOSR/NA	9 PROCUREMENT INSTRUMENT IDENTIFICATION NUMBER: AFOSR-86-0266
8c ADDRESS (City, State, and ZIP Code): Building 410, Bolling AFB Washington, DC 20332		10 SOURCE OF FUNDING NUMBERS: PROGRAM ELEMENT NO. 61102F; PROJECT NO. 2307; TASK NO A1; WORK UNIT ACCESSION NO.

11 TITLE (Include Security Classification)
Theoretical Investigation of 3-D Shock-Wave-Turbulent Boundary Layer Interactions -- Part VII

12 PERSONAL AUTHOR(S)
Doyle Knight

13a TYPE OF REPORT: ~~Technical~~ ANNUAL	13b TIME COVERED: FROM 87/10/1 TO 88/9/30	14 DATE OF REPORT (Year, Month, Day): 88/11/15	15 PAGE COUNT: 75

16 SUPPLEMENTARY NOTATION

17 COSATI CODES		
FIELD	GROUP	SUB-GROUP
	20.04	

18 SUBJECT TERMS (Continue on reverse if necessary and identify by block number)
High speed flows; viscous-inviscid interactions; Boundary layer interactions; computational fluid dynamics; Navier-Stokes equations; turbulence.

19 ABSTRACT (Continue on reverse if necessary and identify by block number)

This research describes continuing efforts in the analysis of 3-D shock wave/turbulent boundary layer interactions. A significant research activity in 3-D hypersonic shock turbulent interactions is initiated to further develop and validate the theoretical model. The quasiconical free interaction principle is examined by simulation of two geometries - 17.5 deg sharp fin and (30,60) swept compression corner (Mach 3) - selected to obtain similar shock strengths. The comparison with experimental data is good. It is confirmed that the differences caused by the particular geometry of the model appear only behind the inviscid shock wave. Continuing research on 3-D turbulent interaction control is focused on the effect of bleed and the simulation of flows past the double-fin configuration. The effect of suction is examined on a strong (fin angle=20 deg, Mach 3) and a weak interaction (8 deg, Mach 3). The overall effect of bleed is remarkably modest. Two double-fin configurations ($4^\circ \times 4^\circ$ and $8^\circ \times 8^\circ$, Mach 3) are simulated. A study of the computed flowfield indicates that the first is a weak interaction. In contrast, the 8×8 configuration displays an interesting separated flowfield. An analysis of viscous and inviscid effects in a sharp fin and a swept corner flow indicates that the physics of both geometries are governed primarily by inviscid (pressure) effects. Viscous effects are of lower magnitude but are not restricted to the sublayer region.

20 DISTRIBUTION / AVAILABILITY OF ABSTRACT: ☒ UNCLASSIFIED/UNLIMITED ☐ SAME AS RPT ☐ DTIC USERS	21 ABSTRACT SECURITY CLASSIFICATION: Unclassified
22a NAME OF RESPONSIBLE INDIVIDUAL: LEN SAKELL	22b TELEPHONE (Include Area Code): 202 767 4935 / 22c OFFICE SYMBOL: NA

DD FORM 1473, 84 MAR — 83 APR edition may be used until exhausted. All other editions are obsolete.

SECURITY CLASSIFICATION OF THIS PAGE: Unclassified

Preface

This report presents the research accomplishments for FY88[1] (1 October 1987 to 30 September 1988) of the investigation entitled "Theoretical Investigation of Three-Dimensional Shock-Wave Turbulent Boundary Layer Interactions".

The research has benefited from the assistance of several individuals, including Drs. James Wilson, Jim McMichael and Len Sakell (Air Force Office of Scientific Research) and Dr. C.Horstman (NASA Ames Research Center). The interactions with S. Bogdonoff, D.Dolling, A. Ketchum and G. Settles are acknowledged.

[1] Fiscal Years (FY) refer to the Federal fiscal year

Contents

I Objectives 4

I-1 Develop and Validate Theoretical Model(s) for 3-D Shock Wave–Turbulent Boundary Layer Interaction 4

I-2 Determine the Physical Structure of 3-D Turbulent Interactions for Selected Geometries 4

I-3 Investigate Methods of Control and Modification of 3-D Turbulent Interactions 5

I-4 Examination of Inviscid and Viscous Effects in 3-D Turbulent Interactions . . 5

II Research Accomplishments for FY88 6

II-1 Research Task No. 1: Develop and Validate Theoretical Models for the 3-D Shock Wave-Turbulent Boundary Layer Interactions 6

II-2 Research Task No. 2: Determination of Physical Structure of 3-D Turbulent Interactions for Specific Geometries 7

II-2.1 Results for the 17.5 deg Fin 8

II-2.2 Results for the (30,60) Swept Compression Corner 8

II-2.3 Comments on Quasiconical Similarity 9

II-3 Research Task No. 3: Investigate Methods of Control and Modification of 3-D Turbulent Interactions 10

II-3.1 Effect of Bleed 10

II-3.2 Double shock interactions 12

II-4 Research Task No. 4: Examination of inviscid and viscous effects in 3-D turbulent interactions 12

III Research Program for FY89 (1 October 1988 - 30 September 1989) 14

III-1 Research Task No. 1: Develop and Validate Theoretical Models for 3-D Shock Wave-Turbulent Boundary Layer Interactions 14

III-2 Research Task No. 3: Investigate Methods for Control and Modification of 3-D Turbulent Interactions 14

III-3 Research Task No. 4: Examination of Inviscid and Viscous Effects in 3-D Turbulent Interactions 15

IV Publications and Scientific Interactions 16

IV-1 Written Publications – Cumulative Chronological List 16

V List of Personnel and Degrees Awarded 18

V-1 Personnel: 1 October 1987 - 30 September 1988 18

V-2 Degrees Awarded: 1 October 1987 - 30 September 1988 18

VI References 19

VII Papers 38

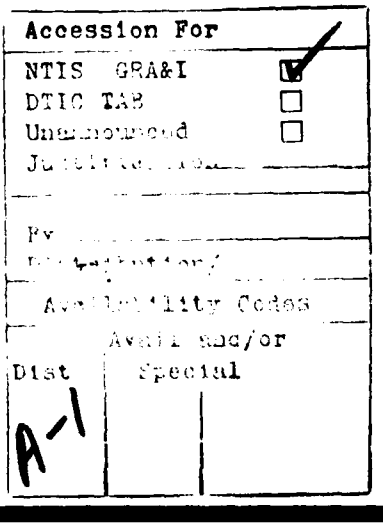

I Objectives

The research program for FY88 is characterized by two major themes, namely, i) the continuation of the research effort in supersonic shock wave-turbulent boundary layer interaction, and ii) the initiation of a significant research activity in 3-D hypersonic shock wave-turbulent boundary layer interaction. The basic four objectives, outlined in the original proposal [1] and described below are pertinent for both supersonic as well as hypersonic research activity.

I-1 Develop and Validate Theoretical Model(s) for 3-D Shock Wave–Turbulent Boundary Layer Interaction

One of the fundamental steps in the understanding of complex 3-D shock wave-turbulent boundary layer interactions involves the development and validation of accurate theoretical models. Numerical effort has progressed from the simplified calculations of the pre-supercomputer years [2,3] to the current complex simulations requiring significantly more computer resources. The Reynolds-averaged full three-dimensional compressible Navier-Stokes equations [4] are typically utilized with turbulence incorporated through a model such as the two-equation Jones-Launder [5] or the algebraic Baldwin-Lomax [6] model. This complexity is necessary to adequately resolve the several fluid dynamic effects that play critical roles in 3-D turbulent interactions including boundary layers, shock waves, turbulence and viscous-inviscid interactions. Recently published results utilizing the above two eddy viscosity models have shown overall good agreement with experimental observations on simplified 3-D geometries such as the sharp fin [7] and the swept compression corner [8,9]. This validation, achieved by comparison with experimental observations, is a continuous element of the research.

The success of the theoretical approach has led to the inception of a new activity, that of modeling three-dimensional *hypersonic* shock wave-turbulent boundary layer interaction ('3-D hypersonic turbulent interactions') in FY88. This represents an extension of previous activity which was focused on supersonic flows.

I-2 Determine the Physical Structure of 3-D Turbulent Interactions for Selected Geometries

Closely related to the task of developing and validating the theoretical model is that of determining the structure of such flow fields. Over the past several years, significant progress has been achieved in obtaining an overall picture of the flowfield for the sharp fin and the swept corner. The author has collaborated with C.C. Horstman (NASA Ames Research), B.Shapey and S.Bogdonoff (Princeton University) in this endeavor. Based on the analysis of flows past the sharp fin [7] and the swept corner [9], the overall flowfield is observed to be inviscid and rotational over a major portion of the interaction domain except within a narrow region adjacent to the surface where the effects of turbulent mixing are significant. For both configurations (Figs. 1 and 2), the principal flow feature is a large vortical structure aligned with the corner in agreement with the flowfield models of Token [10] and Kubota and Stollery [11]. A three-dimensional surface of separation (Fig. 1) emanates from the line of coalescence (separation), and spirals into the vortical center. A second surface, emanating

from upstream, intersects the plate at the line of divergence (attachment), and defines the extent of the fluid entrained into the vortical structure.

For the current year, the primary goals are (Section II-2):

- To reaffirm the validity of the theoretical model consisting of the Reynolds-averaged three-dimensional Navier-Stokes equation in mass averaged variables in conjunction with the algebraic turbulence model of Baldwin and Lomax. This aspect is closely linked to Research Task No. 1 above.
- To provide three-dimensional flow visualization to explore the interaction flow structure.
- To examine numerically the validity of the quasiconical free interaction principle.

I-3 Investigate Methods of Control and Modification of 3-D Turbulent Interactions

The understanding of the flowfield structure of 3-D turbulent interactions provides the opportunity for investigation of methods for control and modification of the interaction flowfields. Specifically, large vortical structures such as those displayed in Figs. 1 and 2 are clearly undesirable in typical applications such as inlets where 3-D turbulent interactions are common. Improvements in the control of such interactions may lead, for example, to improved aircraft performance. Continuing research efforts (Section II-3) focus on bleed (suction) and generation of opposing vorticity by mounting another symmetric fin on the plate (Fig. 3).

I-4 Examination of Inviscid and Viscous Effects in 3-D Turbulent Interactions

Computed results have indicated that the flow structure for the sharp fin and the swept corner are not only remarkably similar but also that *the calculated flowfields are relatively insensitive to the turbulence model employed.* This conclusion is derived from the fact that two different models successfully predicted overall flow features even though eddy viscosity values from the two models differed significantly in the major portion of the boundary layer outside of the viscous sublayer region. The fourth research task is therefore to analyse viscous-inviscid effects in such interactions to further enhance understanding of the inherent physics.

II Research Accomplishments for FY88

The research program follows the basic tasks outlined in the original proposal submitted to Dr. James Wilson on 4 April 1986. Four specific research tasks were outlined for FY88 [12], namely, 1) Development and validation of theoretical models for 3-D shock wave-turbulent boundary layer interactions, 2) Determination of physical structure of 3-D turbulent interactions for specific geometries, 3) Investigation of methods for control and modification of 3-D turbulent interactions and 4) Examination of inviscid and viscous effects in 3-D turbulent interactions.

The overall research program is closely coordinated with the computational research of Dr. C.C. Horstman (NASA Ames Research Center) and the experimental research of Prof. S. Bogdonoff (Princeton University). Drs. Knight, Horstman and Prof. Bogdonoff meet frequently to select specific 3-D shock wave-turbulent boundary layer interactions for detailed study. Separate, independent computations are then performed for the configuration by Drs. Knight and Horstman, and the calculated flowfields are relatively compared with the experimental measurements of Prof. Bogdonoff. This close collaboration between theory and experiment is a critical element of the success of the program.

For the purposes of the following discussion, it is useful to note the general orientation of the physical (x, y, z) axes:

Streamwise direction: x

$\perp$ to plate: y

Spanwise direction: z

II-1 Research Task No. 1: Develop and Validate Theoretical Models for the 3-D Shock Wave-Turbulent Boundary Layer Interactions

A new activity in modeling three dimensional *hypersonic* shock wave-turbulent boundary layer interaction ('3-D hypersonic turbulent interactions') is initiated during FY88. This represents an extension of previous activity which was focused on supersonic flows. A principal objective of this research is the determination of the sensitivity of the computed flowfields in 3-D hypersonic turbulent interactions to the turbulence model employed. Recent experimental and theoretical results at Mach 3 have shown that simple turbulence models (i.e., zero equation and two equation eddy viscosity models) are capable of accurate simulation of a variety of 3-D turbulent interactions [7,8,9], while failing to accurately reproduce the limiting 2-D turbulent interaction [13]. The success in analysing flows past the sharp fin and the swept corner is generally attributed to the nature of the interaction. Specifically, the flowfields investigated are observed to be essentially inviscid and rotational, except in a small fraction of the turbulent boundary layer adjacent to the surface where the effects of turbulence are significant. The absence of reverse flow may also be a factor [14].

A combined experimental and computational research project has been initiated with Dr. C.C. Horstman (NASA Ames Research Center) to examine the 3-D hypersonic turbulent interaction generated by a sharp fin. The selection of this configuration is motivated by several factors. First, through the recent collaborative experimental and theoretical effort involving the principal investigator, NASA Ames Research Center and Princeton Gas Dynamics Laboratory [9] a detailed understanding of the flowfield structure of the 3-D sharp fin turbulent

interaction at Mach 3 has evolved. Second, a series of 3-D sharp fin experiments are planned at hypersonic speeds (Mach 7 and 10) at NASA Ames Research Center in FY89[2]. Efforts to date have focused on the determination of the grid for the calculations. The activity for FY89 is discussed in Section III.

II-2 Research Task No. 2: Determination of Physical Structure of 3-D Turbulent Interactions for Specific Geometries

As mentioned earlier, the current understanding of the flowfield for both the sharp fin and the swept corner is that it is inviscid and rotational over a majority of the interaction domain, except within a narrow region adjacent to the surface where the effects of turbulent mixing are significant, and dominated by a single vortical structure.

Kimmel [15] performed a series of experiments to investigate the effect of the shock generating geometry on the interaction. Three configurations were selected, namely, the sharp fin, swept compression corner and the semicone. The geometrical characteristics were selected to obtain similar shock strengths. Specifically, the sharp fin angle $\alpha = 17.5\,\text{deg}$, the angle of compression and sweep for the swept corner $\alpha = 30\,\text{deg}$ and $\lambda = 60\,\text{deg}$, and the semicone half angle $\gamma = 20\,\text{deg}$ generate equal strength shocks in the free stream. Each configuration was examined at Reynolds numbers of 1.6×10^5 and 9.1×10^5. For the lower Reynolds number, detailed surface pressure and kerosene-lampblack flow visualization was performed. At the higher Reynolds number, experimental data include both surface pressure and kerosene-lampblack flow visualization, and boundary layer profiles of pitot pressure, static pressure and yaw angle.

The three configurations exhibited conical similarity, with the flow surface and flowfield variables exhibiting two distinct regions. The first region, extending from upstream to a point downstream of the shock system, displayed a 'quasi-conical free interaction'. In this region, for example, the experimental pressure distribution, displayed along a line normal to the inviscid shock, was virtually identical for the three configurations *despite their significant geometrical differences.* A second region, downstream of the first region and denoted the 'model dominated region', showed no similarity of profiles.

The explanation for the quasi-conical free interaction is not clear. It is anticipated that all three flowfields display a large vortical structure. The sharp fin at $\alpha = 17.5\,\text{deg}$ is intermediate to a series of computed flows ($\alpha = 10$ and $20\,\text{deg}$) which have displayed a large vortical structure [7]. The swept compression corner at $(\alpha, \lambda) = (30, 60)\,\text{deg}$ is close to the previous computation of Knight *et al* [8] at $(\alpha, \lambda) = (24, 60)$. The semicone, however, has not been computed previously. It is unclear, however, why this vortical structure should yield nearly identical pressure distributions in the quasi-conical free interaction region.

To achieve the primary objectives of this task, both the 17.5 deg sharp fin and the (30, 60) swept corner have been computed in FY88. The results are briefly described below. Further details may be found in [16].

[2] Horstman, Private communication

II-2.1 Results for the 17.5 deg Fin

The results are first compared with experiment. Boundary layer survey data is available at sixteen (16) locations exhibited in Fig. 4. The computed and experimental surface pressure are displayed in Fig. 5 at $z_s = 9.6\delta_\infty$ with z_s denoting the distance from the model apex along the inviscid shock trace. Overall features of the measured distribution are predicted by the computation. Upstream influence (determined by initial pressure rise) is underpredicted in the computation. The plateau region, observed by several previous investigators, between separation and attachment is adequately reproduced by the computation though the flatness of the plateau region is not well resolved. The computed and experimental pressure rise after the shock wave and the downstream pressure level differ by less than 7%. The shallower computed pressure gradient is assumed largely due to inadequate grid resolution in the interaction region.

Typical results of the experimental and computational boundary layer profiles of pitot pressure, yaw angle and static pressure at station 12 are shown in Fig. 6. Good agreement is observed in the boundary layer for pitot pressure, yaw angle and static pressure. The computed pitot pressure does not resolve the small overshoot associated with the compression fan outside the boundary layer. The computed static pressure continues to increase toward the inviscid region while the measured data slightly decreases.

The measured surface streamline patterns for the 17.5 deg fin are displayed in Fig. 7. The computed result is shown in Fig. 8. The computation predicts qualitatively all of the main features revealed by the experiment. A line of coalescence is formed outside of the inception zone near the model apex. The lines of upstream influence and coalescence are approximately straight rays from a virtual origin. The computation underpredicts the angle of the line of upstream influence and line of coalescence by 14.5% and 15.5% respectively. This underprediction has also been observed previously [7] for other fin angles. A divergence line is seen near the fin which divides the fluid flowing over to that being entrained into the vortical structure. The surface streamlines between the line of coalescence and the line of divergence (attachment) converge asymptotically with the line of coalescence. No secondary separation [17] is observed.

The flow structure is examined with exhaustive sets of particle traces. For the purpose of brevity, only a few are selected for presentation. Fig. 9 displays traces of particles released at the upstream end of the computed domain at $y = 0.5\delta_\infty$. For illustration, the line of coalescence is also displayed. The streamlines roll into a large vortical structure with particles near the fin surface pitching down and away from the fin beneath the vortical core. The orientation of the vortical structure is counterclockwise as viewed from the base of the fin leading edge. Particles released from upstream at $y = 1.1\delta_\infty$ are displayed in Fig. 10 with the line of coalescence. The fluid particles at this height are not entrained into the vortical structure and simply flow over the interaction. Additional extensive particle traces are consistent with these features.

II-2.2 Results for the (30,60) Swept Compression Corner

The surface pressure at $z_s = 10\delta_\infty$ of the (30,60) swept corner is displayed in Fig. 11. The computed results underpredict upstream influence. The plateau pressure level, the rapid pressure rise after the shock wave and the sharp peak ("corner pressure") near the model corner

are accurately predicted. The slight drop at the end of the plateau region is not adequately resolved. The location of the maximum pressure predicted by computation is upstream of that measured. This indicates that the extent of the computed results underpredict the size of the interaction region. The computed final pressure level is about 10% below the measured value.

The computed and measured contour plots for the flowfield static pressure is shown in Fig. 12. Overall, good agreement is obtained between computation and experiment. Although the slope of the upstream foot of the λ-shock structure is accurately predicted by the computation, the large gradients in the compression waves are smoothed out. The computation shows that both the front and the rear foot of the λ-shock are approximately planar within the accuracy of the numerical interpolation. The two systems of the compression waves merge at about $y = 2.0\delta_\infty$.

The measured and computed surface streamlines are shown in Figs. 13 and 14 respectively. As in the fin case, all of the qualitative features of the surface flow visualization are predicted by the computation. The computed upstream influence and line of coalescence are in reasonable agreement with experiment with relative underprediction of about 10%. The divergence line (attachment) is located on the model surface. The analysis of the surface pattern is similar to that provided for the sharp fin above.

Computed mean streamlines are displayed in Figs. 15 and 16. In Fig. 15, three sets of streamlines are shown, the first released within the computational sublayer near the wall, the second and third sets released at $y = 0.5\delta_\infty$ and $y = 1.2\delta_\infty$ respectively. The overall flow structure is somewhat similar to that for the sharp fin. The first set of particles form the line of coalescence, the second set is entrained into the vortical structure while the the third set is lifted by the model and moves downstream along the corner surface. Fig. 16 displays a side view of the previous plot with only the second and third sets. Other sets of traces are consistent with the above results.

II-2.3 Comments on Quasiconical Similarity

For the purposes of discussion, the surface pressure of the two models are compared in Fig. 17. The experimental data is superimposed. The experiment clearly shows that the upstream portion of the surface pressure is almost identical for the interaction generated by the two models. The differences caused by the particular geometry of the model appear only behind the inviscid shock wave. The computed surface pressure of the two interactions also shows some similarity upstream of the shock wave.

The flowfield structure is investigated using the particle tracing technique and MOVIE.BYU color graphics software. In Fig. 18, two flow ribbons and two flow stream surfaces of the 17.5 deg fin interaction flowfield are displayed. The red surface is the 'surface of separation' which emanates from the line of coalescence and rises from the flat plate into the vortical core. The blue surface is called 'surface of attachment' which intersects the flat plate at the line of divergence. The lower ribbon begins to turn near the model apex and moves below the surface of separation twisting along the way. The upper flow ribbon which is originally above the surface of attachment is not entrained into the vortical structure and moves downstream almost parallel to the fin surface. The overall flowfield structure is apparent. Particles originating between the plate and the surface of attachment are entrained into the vortical structure

while those originating above the surface of attachment flow over the vortical structure.

II-3 Research Task No. 3: Investigate Methods of Control and Modification of 3-D Turbulent Interactions

As indicated previously, the motivation for this research task lies in the existence of an undesirable large vortical structure in 3-D turbulent interactions. Several techniques may be appropriate for flow control including 1) bleed (suction) to remove low energy fluid in the boundary layer, 2) generation of vorticity of opposite sign (e.g., with the symmetric double wedge configuration (Mee and Stalker [18])), 3) blowing (normal or wall-jet) to enhance the kinetic energy of particles in the boundary layer, and 4) geometrical modifications such as raising the sharp fin a finite distance above the surface[3].

The focus the present research is two-fold:

- Bleed (suction): Bleed has been traditionally employed in high speed aircraft inlets to prevent boundary layer separation. Conventional theory dictates that the effect of suction is to remove the low speed fluid in the boundary layer before it separates from the surface.

- Shock-shock Intersections: Mee and Stalker [18] have concluded from experimental observations that intersecting shocks can produce a given overall pressure rise with lesser likelihood of separation than an equivalent strength single shock interaction. Their experiments were restricted to weak interactions. This concept is unproven, however, and additional computational and experimental research is required to determine its validity.

II-3.1 Effect of Bleed

A series of computations on the 20° single fin configuration (SFC) with Mach and Reynolds numbers 3 and 9×10^5, with porous suction over a triangular region extending from the line of upstream influence to the theoretical inviscid shock location (Region I in Fig. 19) has been described in previous literature [19]. The maximum bleed corresponded to removal of approximately 25 % of the upstream boundary layer. The computed streamline structure was observed to be essentially independent of the surface bleed flow rate, although the line of coalescence moved downstream toward the theoretical inviscid shock footprint (TISF) and upstream influence was reduced. The effect of bleed was focused principally in a small fraction of the boundary layer. This represents a significant and surprising result and brings into question the efficacy of boundary layer bleed for sidewall interactions in high speed inlets. Numerical simulation of bleed on a different area - the region on the plate between the TISF and the base of the fin (Region II in Fig. 19) and performed in FY88 are described. Approximately 8% of the incoming boundary layer is bled off from the region on the flat plate extending between the theoretical inviscid shock line and the surface of the sharp fin. The influence of bleed in this region on the vortical structure is also found to be insignificant. A detailed description of the results may be found in Gaitonde and Knight [20][4].

[3] S. Bogdonoff, Private communication

[4] See Section VII

The recent experiment of Barnhart *et al* [21] with suction on a roughly rectangular area covering a strip on either side of the theoretical shock footprint (Fig. 20) on an incipiently separated configuration (8° SFC, Mach 3, $Re_{\delta_\infty} = 6.5 \times 10^5$) is not extensive enough to provide general guidelines. Nevertheless, their observation of beneficial effects of suction warrants numerical investigation. This computation is complete and results are described in [20]. Briefly, comparison with experimental data and analysis of computed results indicates that the effect of bleed is primarily to reduce the surface angularity and upstream influence. The major portion of the flow is not influenced by suction.

The overall effect of suction, based on the above computations on the strong (20 deg) and weak (8 deg) configurations, may be summarized as follows:

- Effect on surface streamlines: For the stronger interaction, the effect of bleed upstream of the shock footprint (Region I) is to reduce the surface angularity of the flow. The line of coalescence observed in the absence of bleed [7] persists although its angle with the shock footprint is significantly reduced. This reduction is proportional to bleed magnitude. Region II bleed has no effect on surface streamlines which resemble those in the absence of suction. For the weaker interaction, surface yaw angles also display lower values in presence of suction. A general statement about the effect of bleed on separation cannot be made for the weaker configuration since it is only incipiently separated even in the absence of bleed.

- Effect on surface variables: Region I bleed results in lower upstream influence and higher rate of pressure rise in the interaction although the total pressure rise remains the same. Region II bleed does not display any effect on surface pressure rise. For the weak interaction, the results are similar to those for Region I bleed on the strong interaction. In the absence of further computation, it is not possible to distinguish between the effects of upstream and downstream (of the shock footprint) bleed. The effect of all regions of bleed considered (on both the strong and the weak configuration) is to increase local skin friction drastically. It is evident that a significant drag penalty is associated with bleed.

- Effect on shock structure: Region I bleed results in a tightening of the upstream leg of the λ-shock structure as a result of reduced displacement thickness of the interaction. This reduction is evident also by the elimination of the pitot pressure overshoot observed in the interaction in the absence of bleed. Region II bleed has no effect on either the upstream or the downstream compression fans. For the weak interaction, the upstream compression fan is seen to disappear completely. This is probably due to a combination of the relatively high values of bleed utilized and the inherent weakness of the interaction.

- Effect on vortical structure: Neither bleed region has any significant effect on the vortical structure observed in the strong interaction although larger portions of the incoming boundary layer are ingested with increased bleed magnitude. Only particles whose *no bleed* trajectories pass close to the bleed region are ingested. Although no statement can be made about the effect of bleed on the vortical structure for the weaker interaction, it is observed, that particles escaping the influence of bleed follow paths similar to those in the no bleed configuration.

II-3.2 Double shock interactions

Following the conclusions of Mee and Stalker that shock-shock intersections may be capable of producing a given pressure rise with less likelihood of separation than a single shock interaction, a systematic study of symmetric double fin configurations is initiated. A calculation was performed previously [19] for the strongest intersecting shock configuration of Mee and Stalker corresponding to incoming Mach and Reynolds numbers 1.85 and 7.8×10^4 and symmetric sharp fins with angles of 5 deg each. The results indicated overall good agreement with experiment with one interesting anomaly that the computation overpredicted the extent of upstream influence by approximately 13%. This is in contrast to previous 3-D turbulent interaction studies [7] where computations have consistently underpredicted upstream influence. A more systematic study of stronger interactions is described in this research. The Mach and Reynolds numbers are 2.95 and 2×10^5 respectively for symmetric fin angles of 4 deg and 8 deg. The flow parameters are chosen after consideration of experimental facilities available at the Gas Dynamics Laboratory at Priceton University. The 4×4 configuration is a completely weak interaction for the domain under consideration. In contrast, the 8×8 configuration displays a surface flow pattern with yaw angles larger than the primary shock angle and an interesting node-like structure (whose validity is suspect) near the trailing edge of the domain. The consequent separated flow is examined with particle traces (Section VII). Particles released close to the plate but outside the sublayer follow the general pattern of the surface streamlines up to the node at which point they rise and move parallel to the center line. Particles released in the vicinity of the line of symmetry at various heights move parallel to it (as expected from the imposed boundary conditions) but rise up and away from the plate to form an arch-like trace at the downstream end of the domain. Particles released near the corner formed by the fin and the plate pitch toward the plate and yaw toward the line of symmetry straightening out as they approach it. At higher distances from the plate, particles released near the fin pitch toward the plate over the particles beneath yawing toward the centerline. The arch-like structure formed by the particles released near the centerline broadens so that the overall flow approaches the boundary layer flow (due to the fin) expected at large distances from the plate. It is anticipated that equivalent experiments will be performed in the near future.

II-4 Research Task No. 4: Examination of inviscid and viscous effects in 3-D turbulent interactions

The flowfield results using the two different turbulence models for both fin and swept corner configurations have been found to be in close agreement except for modest differences in a small fraction of the boundary layer adjacent to the surface. This relative insensitivity of the flowfield to the type of turbulence model employed in the computations suggests that the interaction is primarily an inviscid and rotational phenomenon, with viscous influence being limited to regions very close to the wall or surface. The present study was initiated to verify this hypothesis through an extensive investigation of the sharp fin and swept compression corner flowfields computed using the two different turbulence models.

The analysis of the flow past the 20 deg fin and the (24,40) swept compression corner both at Mach 3, $Re_\delta \sim 9 \times 10^5$ is complete. The actual flows were computed separately by Knight and Horstman who utilize the Baldwin-Lomax and Jones-Launder turbulence models

respectively.

The following approach is adopted in the analysis of the flowfields:

1. A numerical code is developed to integrate the mean kinetic energy equation along streamlines in the flow and to compute the contributions to the rate of change of mean kinetic energy by viscous and inviscid terms. Using this code, several streamlines originating at various y-locations within and outside the boundary layer are examined. The results for both sharp fin and swept compression corner flows indicate that although inviscid effects in general govern the dynamics of the interaction along the streamlines, viscous influence remains significant even at points considerably distant from the plate or surface.

2. A 'planewise' investigation of the interaction flowfields is carried out in order to directly determine the relative importance of viscous and inviscid contributions in various regions of the flow. The magnitudes of the viscous and inviscid terms (of the mean kinetic energy equation) are compared directly at points lying on various $y-z$ planes (for the sharp fin) and at points lying on various $x-y$ planes (for the swept compression corner). It is observed that although the interaction is governed primarily by inviscid effects, viscous influence is significant even in regions of the flow distant from the surface.

Color graphics is extensively utilized to visualize the results of this 'planewise' analysis. Figs. 21 and 22 display the magnitudes of the inviscid and viscous terms respectively for the sharp fin interaction ($\alpha = 20\,\text{deg}$, Mach 3, $Re_\delta = 9 \times 10^5$), computed with the the Baldwin-Lomax turbulence model, on a $y-z$ plane (normal to the streamwise direction) and at a location $x = 15\delta_\infty$. The inviscid (pressure) influence is concentrated towards the freestream side of the interaction (i.e. away from the fin surface). The viscous effects are concentrated to the immediate left of the region of inviscid influence. Similar results have been observed for other $y-z$ planes at various x locations. The flowfield computed using the Jones-Launder model shows similar results with regard to the concentration of inviscid influence in the flow but viscous influence is observed to be concentrated in a fraction of the boundary layer adjacent to the surfaces of the fin and the plate.

The results for the swept corner interaction computed using the Baldwin-Lomax model parallel those for the sharp fin for both viscous and inviscid terms. The flowfield computed using the Jones-launder model for this interaction agrees as far as the inviscid terms are concerned but differs with respect to the region of concentration of viscous influence.

A more complete discussion of the approach to the problem and the results of this research task is included in the attached paper titled "Viscous/Inviscid Influence in 3D Shock Wave-Turbulent Boundary Layer Interactions", submitted for the AIAA Meeting in January, 1989 and included in Section VII.

III Research Program for FY89 (1 October 1988 - 30 September 1989)

III-1 Research Task No. 1: Develop and Validate Theoretical Models for 3-D Shock Wave-Turbulent Boundary Layer Interactions

A series of computations will be performed during FY89 for the 3-D sharp fin configuration at Mach 7 at fixed Reynolds number for several fin angles α. Additional computations may be performed at Mach 10. The flow conditions will be selected to agree with the planned experiments at NASA Ames. Although the precise requirements for the number of grid points and CPU time depends on the specific case, experience has indicated that typically 100,000 grid points and 10 CYBER 205 CPU hours are required [7] for each case.

The computed results will be compared with experimental data. Present plans include measurements of surface pressure and heat transfer, surface oil film visualization, and boundary layer profiles of pitot and static pressure, velocity and turbulence fluctuations. The data and graphics postprocessing will be performed at the Rutgers College of Engineering Supercomputer Remote Access and Graphics Facility.

III-2 Research Task No. 2: Investigate Methods for Control and Modification of 3-D Turbulent Interactions

The proposed research activity is strongly dependent on the availability of experimental data and will focus on the double fin configuration and the lifted fin configuration (consisting of a fin slightly separated from the flat plate thus permitting flow bleed through the corner). The computations on the double-fin configuration utilized parameters chosen in anticipation of experiments to be performed at the Princeton Gas Dynamics Laboratory. In particular, the lengths of the fins and the spanwise separation (Fig. 3) were tentatively based on dimensions of the wind tunnel to be employed. The experimental apparatus to be actually utilized is currently in advanced stages of calibration [22]. The apparatus differs from the configuration employed in two ways:

- Model Structure: The experimental setup exhibits both vertical and horizontal planes of symmetry thus resembling more closely an inlet configuration. Horizontal symmetry is achieved by utilizing a top plate symmetric with the bottom plate. The physical domain employed for double shock interactions in Section II-3 does not possess a horizontal plane of symmetry and, consequently asymptotic 2-D boundary conditions are enforced at the top boundary.

- Dimensions: The actual dimensions of the model are currently being redetermined based on practical wind-tunnel operation constraints.

The systematic series of experiments initiated in FY87 will be continued in FY89 with close collaboration with Prof. Bogdonoff of Princeton University.

A preliminary experimental investigation into the effect of corner bleed [23] has been recently completed at the Princeton Gas Dynamics Laboratory.[5]. Although lifting the fin off

[5] S. Bogdonoff, Private communication.

the plate does not alter the components of the physical model (fin and plate) in any drastic fashion, significant complexities in grid generation and boundary conditions (e.g., under the fin) may arise. An initial investigation into the feasibility of such a computation will be carried out.

III-3 Research Task No. 3: Examination of Inviscid and Viscous Effects in 3-D Turbulent Interactions

Efforts will continue on the quantitative analysis of inviscid and viscous effects for the 3-D swept compression corner and the 3-D sharp fin flowfields. These activities will include:

- Examination of the error in the evaluation of the mean kinetic energy for the swept compression corner for $(\alpha, \lambda) = (24, 40)$ deg at Reynolds number 2.6×10^5.
- The flowfields computed to investigate the quasiconical free interaction principle (Section II-2) will be analysed for viscous-inviscid effects
- Other flow equations (e.g., the mean vorticity equation) will be examined

High resolution color graphics visualization will be employed for presentation of the results.

IV Publications and Scientific Interactions

IV-1 Written Publications – Cumulative Chronological List

1. 1 October 1981 - 30 September 1982

   (a) Knight, D., "Application of Curvilinear Coordinate Generation Techniques to the Computation of Internal Flows", in *Numerical Grid Generation - Proceedings of a Symposium on the Numerical Generation of Curvilinear Coordinates and their Use in the Numerical Solution of Partial Differential Equations*, North-Holland, New York, 1982, pp. 357-384.[6]

   (b) Knight, D., "A Hybrid Explicit - Implicit Numerical Algorithm for the Three-Dimensional Compressible Navier-Stokes Equations", AIAA Paper No. 83-0223, AIAA 21st Aerospace Sciences Meeting, January 10-13, 1983. Published in AIAA J., Vol. 22, Aug 1984, pp. 1056-1063.[7]

   (c) Visbal, M., and Knight, D., "Generation of Orthogonal and Nearly Orthogonal Coordinates with Grid Control Near Boundaries", AIAA J. Vol. 20, No. 3, March 1982, pp. 305-306. [8]

2. 1 October 1982 - 30 September 1983

   (a) Knight, D., "Calculation of a Simulated 3-D High Speed Inlet Using the Navier-Stokes Equations", AIAA Paper No. 83-1165, AIAA/SAE/ASME 19th Joint Propulsion Conference, Seattle, Washington, June 27-29, 1983.[9]

   (b) Visbal, M., and Knight, D., "Evaluation of the Baldwin-Lomax Turbulence Model for Two-Dimensional Shock Wave Boundary Layer Interactions", AIAA Paper No. 83-1697, AIAA 16th Fluid and Plasma Dynamics Conference, Danvers, Mass., July 12-14, 1983. Published in AIAA J., Vol, 22, July 1984, pp. 921-928.[10]

3. 1 October 1983 - 30 September 1984

   (a) Knight, D., "Numerical Simulation of Three-Dimensional Shock-Turbulent Boundary Layer Interaction Generated by a Sharp Fin", AIAA Paper No. 84-1559, AIAA 17th Fluid Dynamics, Plasmadynamics and Lasers Conference, June 25-27, 1984. Published in the AIAA J., Vol. 23, December 1985, pp. 1885-1891.[11]

   (b) York, B., and Knight, D., "Calculation of Two-Dimensional Turbulent Boundary Layers Using the Baldwin-Lomax Model", AIAA 23rd Aerospace Sciences Meeting, Jan 14-17, 1984. Published in the AIAA J., Vol. 23, Dec 1985, pp. 1849-1850.

4. 1 October 1984 - 30 September 1985

[6] Research sponsored by AFOSR Grant 82-0040 and 80-0072
[7] Research sponsored by AFOSR Grant 82-0040 and 80-0072
[8] Research sponsored by AFOSR Grant 80-0072 and AF Contract F-33615-C-3008
[9] Research sponsored by AFOSR Grant 82-0040
[10] Research sponsored by AFOSR Grant 82-0040
[11] Research sponsored by AFOSR Grant 82-0040

(a) Knight, D., "Modeling of Three Dimensional Shock Wave Turbulent Boundary Layer Interactions", in *Macroscopic Modeling of Turbulent Flows*, Lecture Notes in Physics, Vol. 230, Springer-Verlag, NY, 1985, pp. 177-201.

(b) Knight, D., Horstman, C., Shapey, B. and Bogdonoff, S., "The Flowfield Structure of the 3-D Shock Wave-Boundary Layer Interaction Generated by a 20 deg Sharp Fin at Mach 3", AIAA Paper No. 86-0343, AIAA 24th Aerospace Sciences Meeting, January 6-9, 1986. Published in the AIAA J., Vol. 25, Oct 1987, pp. 1331-1337.

(c) Ong, C., and Knight, D., "A Comparative Study of the Hybrid MacCormack and Implicit Beam-Warming Algorithms for a Two-Dimensional Supersonic Compression Corner", AIAA Paper No. 86-0204. Published in the AIAA J., Vol. 25, Mar 1987, pp. 401-407.

5. 1 October 1985 - 30 September 1986

(a) Knight, D., Horstman, C., Ruderich, R., Mao, M.-F., and Bogdonoff, S., "Supersonic Flow Past a 3-D Swept Compression Corner at Mach 3", AIAA Paper No. 87-0551, AIAA 25th Aerospace Sciences Meeting, January 12-15, 1987.

6. 1 October 1986 - 30 September1987

(a) Gaitonde, D., and Knight, D., "Numerical Experiments on the 3-D Shock Wave-Boundary Layer Interaction Generated by a Sharp Fin", AIAA Paper No. 88-0309, AIAA 26th Aerospace Sciences Meeting, January, 11-14, 1988.

(b) Knight, D., Raufer, D., Horstman, C., Ketchum, A., and Bogdonoff, S., "Supersonic Turbulent Flow Past a Swept Compression Corner at Mach 3: Part II", AIAA Paper No. 88-0310, AIAA 26th Aerospace Sciences Meeting, January 11-14, 1988.

7. 1 October 1987 - 1 September 1988

(a) Gaitonde, D., and Knight, D., "Numerical Investigation of Some Control Methods for 3-D Turbulent Interactions Generated by Sharp Fins", To be presented at the 27th Aerospace Sciences Meeting, Reno, Jan. 9-12 1989.

(b) Narayanswami, N., and Knight, D., "Viscous/Inviscid Effects in 3-D Shock Wave-Turbulent Boundary Layer Interactions", To be presented at the 27th Aerospace Sciences Meeting, Reno, Jan. 9-12 1989.

V List of Personnel and Degrees Awarded

V-1 Personnel: 1 October 1987 - 30 September 1988

Principal Investigator:

Prof: Doyle Knight
Department of Mechanical and Aerospace Engineering

Graduate Research Assistants working on this project:

Supported by AFOSR Grant 86-0266

Mr. Datta Gaitonde
Department of Mechanical and Aerospace Engineering

Mr. Natraj Narayanswami
Department of Mechanical and Aerospace Engineering

Supported by Other Sources:

Mr. Yan Zang
Department of Mechanical and Aerospace Engineering
Grant: Rutgers University Excellence Fellowship

V-2 Degrees Awarded: 1 October 1987 - 30 September 1988

Zang, Y., "A Numerical Investigation of 3-D Shock Wave - Turbulent Boundary Layer Interactions Generated by the Sharp Fin and Swept Compression Corner", MS Thesis, Department of Mechanical and Aerospace Engineering, October 1988.

VI References

[1] D. Knight. *Theoretical Investigations of 3-D Shock Wave-Turbulent Boundary Layer Interactions: Part VII.* Technical Report, A three Year Proposal for the Period Beginning 1 October 1986, New Brunswick, New Jersey, 4 April 1986.

[2] T. Reyhner and Hickcox. T. Combined Viscous-Inviscid Analysis of Supersonic Inlet Flowfields. *Journal of Aircraft*, 9:589–595, August 1972.

[3] S. Lubard and W. Helliwell. Calculation of the Flow on a Cone at High Angle of Attack. *AIAA Journal*, 12:965–974, July 1974.

[4] M. Rubesin and W. Rose. The Turbulent Mean-Flow, reynolds-Stress and Heat-Flux Equations in Mass Averaged Dependent Variables. *NASA TMX 62248*, March 1973.

[5] W. Jones and B. Launder. The Prediction of Laminarization with a Two-Equation Model of Turbulence. *Int. J. Heat and Mass Transfer*, 15:301–304, 1972.

[6] B. Baldwin and H. Lomax. Thin Layer Approximation and Algebraic Model for Separated Flows. *AIAA Paper 78-257*, 1978.

[7] D. Knight, C. Horstman, B. Shapey, and S. Bogdonoff. Structure of Supersonic Turbulent Flow Past a Sharp Fin. *AIAA Journal*, 25:1331–1337, October 1987.

[8] D. Knight, C. Horstman, R. Ruderich, M-F. Mao, and S. Bogdonoff. Supersonic Turbulent Flow Past a 3-D Swept Compression Corner at Mach 3. *AIAA Paper 87-0551*, 1987.

[9] D. Knight, D. Raufer, C. Horstman, A. Ketchum, and S. Bogdonoff. Supersonic Turbulent Flow Past a Swept Compression Corner. *AIAA Paper 88-0310*, 1988.

[10] K. Token. *Heat Transfer Due to Shock Wave/Turbulent Boundary Layer Interactions in High Speed Weapons Systems.* Technical Report TR-74-77, AFFDL, 1974.

[11] H. Kubota and J. Stollery. An Experimental Study of the Interaction Between a Glancing Shock Wave and a Turbulent Boundary Layer. *J. Fluid Mech.*, 116:431–458, 1982.

[12] D. Knight. *Theoretical Investigations of 3-D Shock Wave-Turbulent Boundary Layer Interactions: Part VI.* Technical Report RU-TR-171-MAE-F, Department of Mechanical and Aerospace Engineering, Rutgers University, New Brunswick, New Jersey, 1988.

[13] C. Ong and D. Knight. Hybrid Maccormack and Implicit Beam-Warming Algorithms for a Supersonic Compression Corner. *AIAA Journal*, 25:401–407, March 1987.

[14] C. Horstman and C. Hung. Computation of Three-Dimensional Turbulent Separated Flows at Supersonic Speeds. *AIAA Paper 79-0002*, 1979.

[15] R. Kimmel. *An Experimental Investigation of Quasi-Conical Shock Wave / Turbulent Boundary Layer Interactions.* PhD thesis, Aerospace and Mechanical Engineering, Princeton University, 1987.

[16] Y. Zang. *A Numerical Investigation of 3-D Shock Wave-Turbulent Boundary Layer Interactions Generated by the Sharp Fin and Swept Compression Corner.* Master's thesis, Mechanical and Aerospace Engineering, Rutgers University, 1988.

[17] A. Zheltovodov. Regimes and Properties of Three-Dimensional Separation Flows Initiated by Skewed Compression Shocks. *Zhurnal Prikladnoi Meekhaniki i Tekhnicheskoi Fiziki*, 3:116–123, May-June 1982.

[18] D. Mee and R. Stalker. Investigation of Weak Shock-Shock and Shock-Expansion Intersection in the Presence of a Turbulent Boundary Layer. *AIAA Paper 87-0549*, 1987.

[19] D. Gaitonde and D. Knight. Numerical Experiments on the 3-D Shock Wave - Boundary Layer Interaction Generated by a Sharp Fin. *AIAA Paper 88-0309*, 1988.

[20] D. Gaitonde and D. Knight. Numerical Investigation of Some Control Methods for 3-D Turbulent Interactions due to Sharp Fins. *To be presented at the 27th Aerospace Sciences Meeting, Reno, Nevada*, 1989.

[21] P.J. Barnhart, I. Greber, and W.R. Hingst. Glancing Shock Wave-Turbulent Boundary Layer Interaction with Boundary Layer Suction. *AIAA Paper 88-0308*, 1988.

[22] P. Batcho, A. Ketchum, and S. Bogdonoff. Preliminary Study of the Interactions Caused By Crossing Shock Waves and a Turbulent Boundary Layer. *To be presented at the 27th Aerospace Sciences Meeting, Reno, Nevada*, 1989.

[23] S. Bogdonoff and A. Toby. An Exploratory Study of Corner Bleed on a Three-Dimensional Shock Wave Turbulent Boundary Layer Interaction. *To be presented at the 27th Aerospace Sciences Meeting, Reno, Nevada*, 1989.

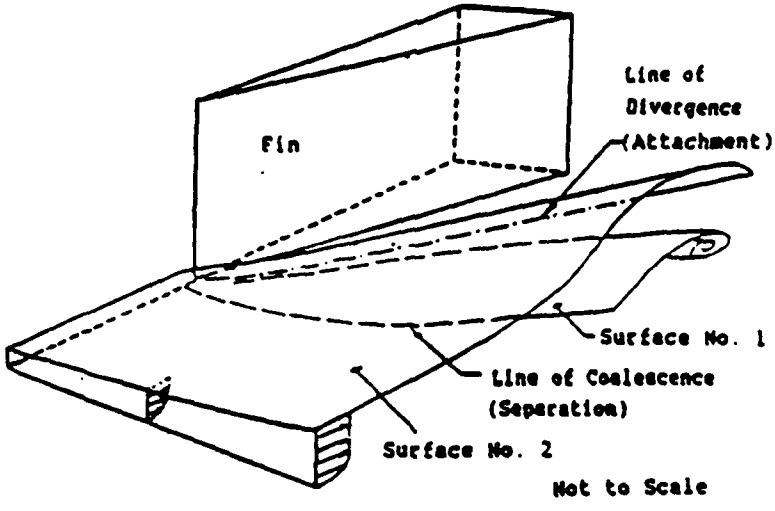

Figure 1: Flowfield for sharp fin

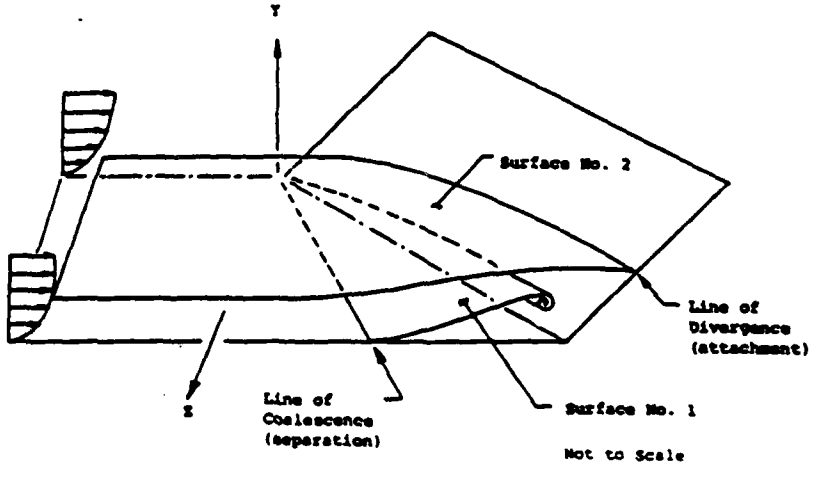

Figure 2: Flowfield for swept corner

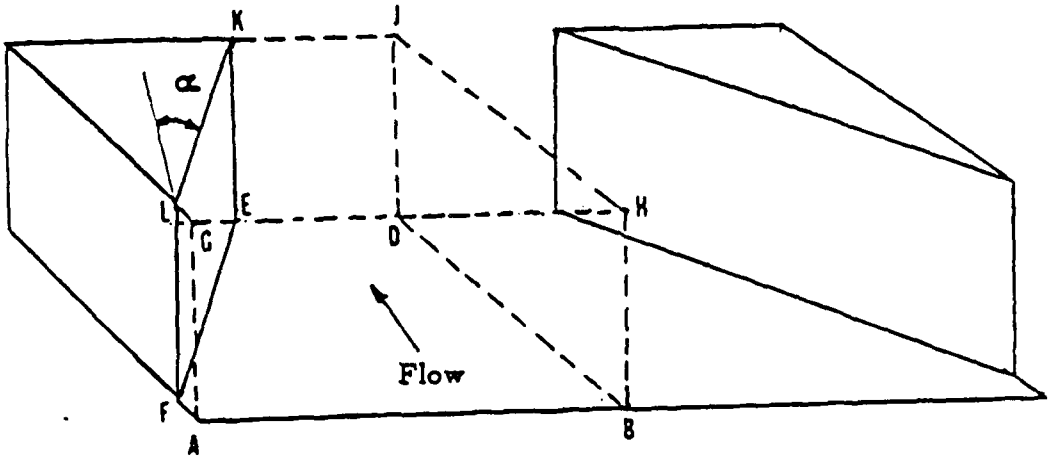

Figure 3: Double fin configuration

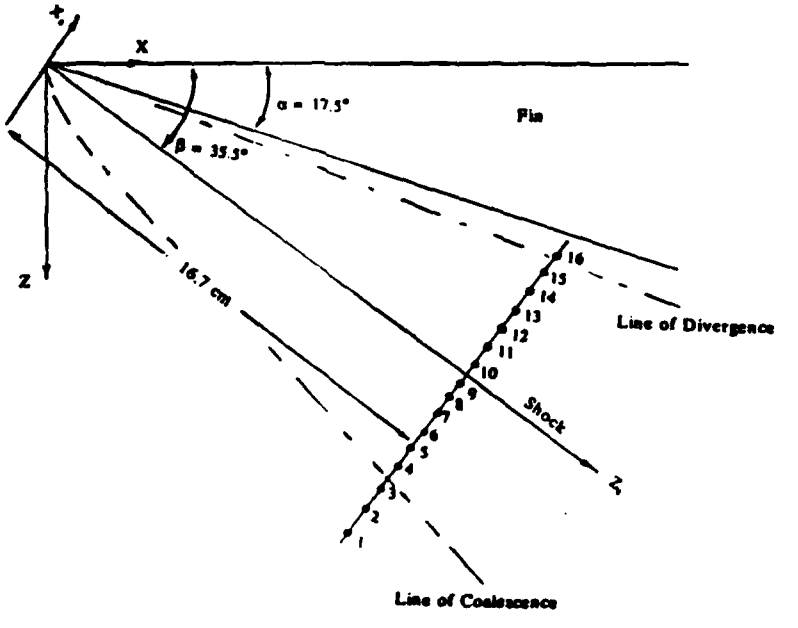

Figure 4: Location of experimental surveys — 17.5 deg fin

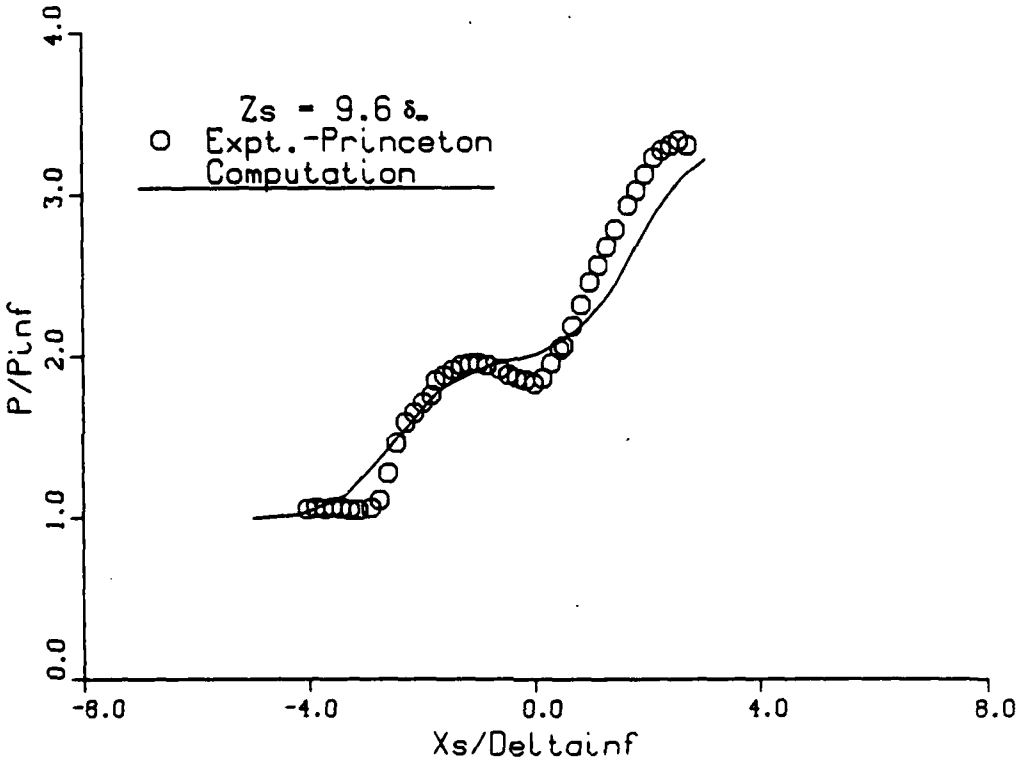

Figure 5: Surface Pressure for 17.5 deg Fin ($z_s = 9.6\delta_\infty$)

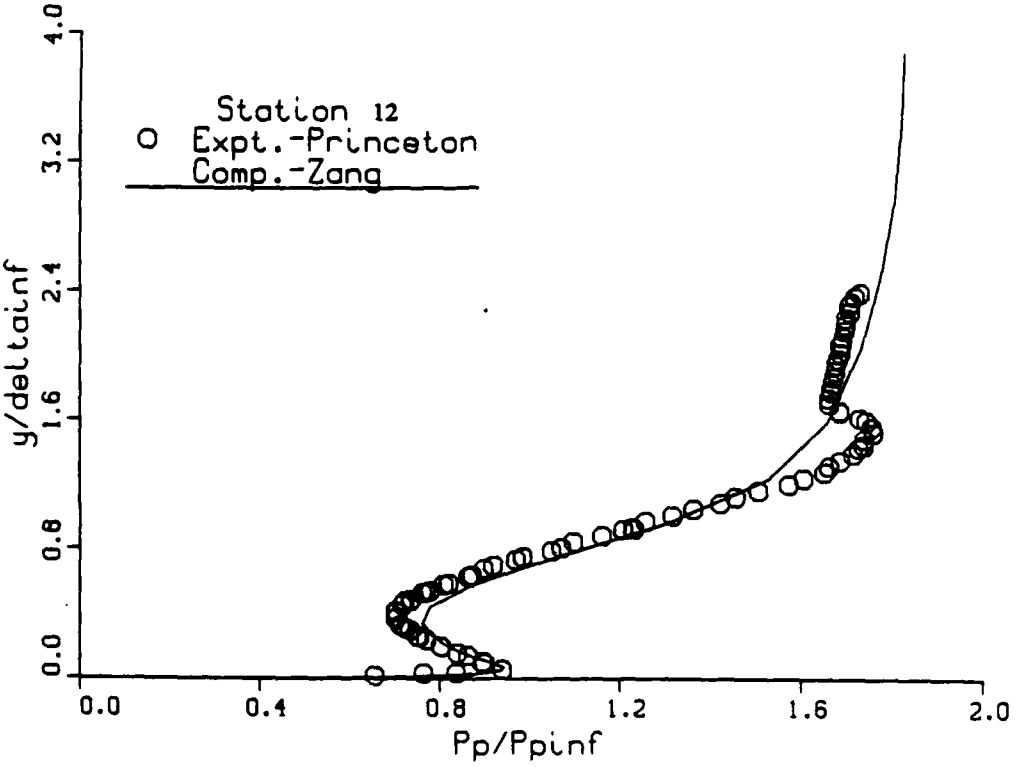

Figure 6 (a) (1 of 3): Pitot pressure at Station 12 – 17.5 deg fin

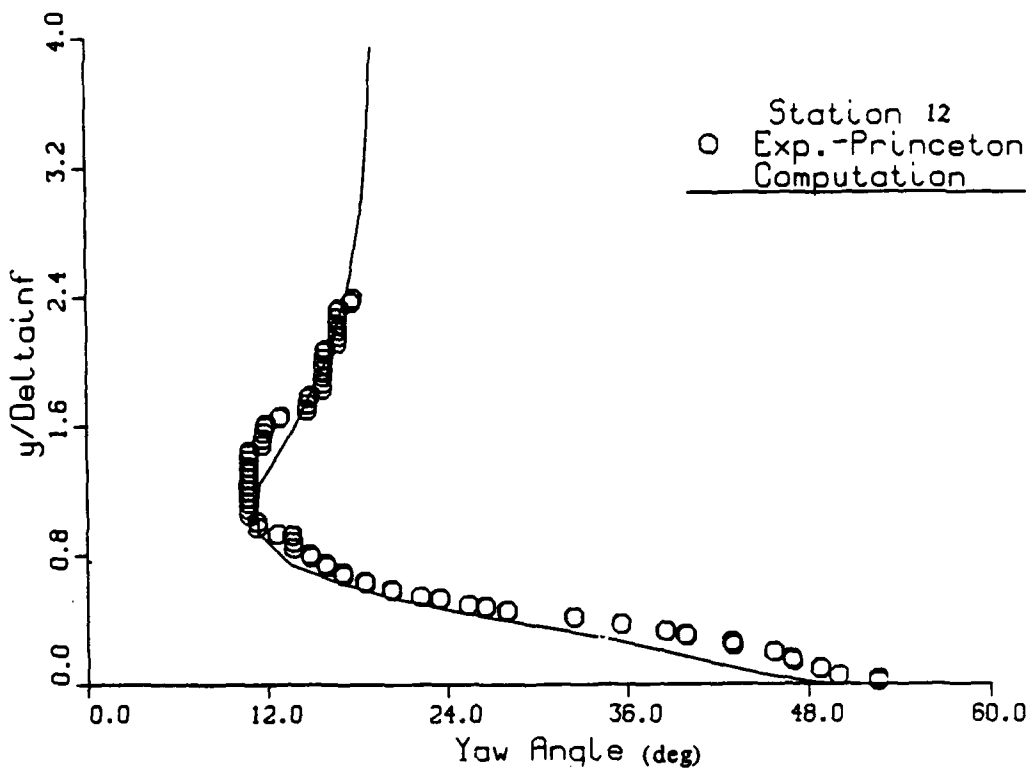

Figure 6 (b) (2 of 3): Yaw angles at Station 12 – 17.5 deg fin

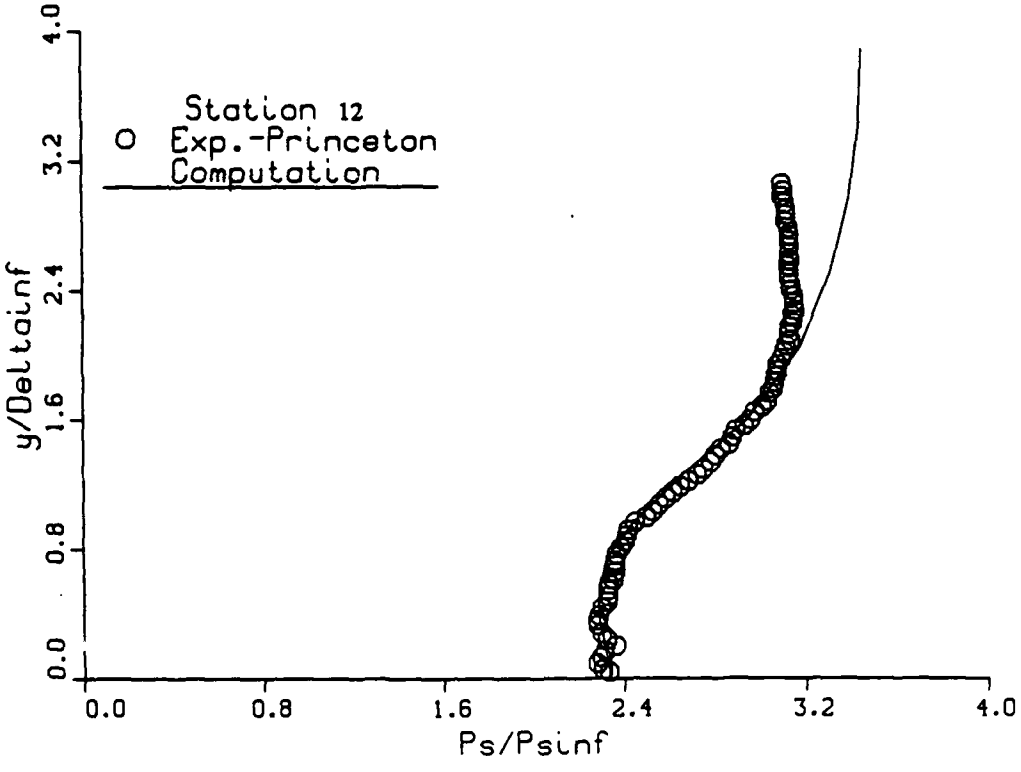

Figure 6: Static pressure comparison at Station 12 – 17.5 deg fin (3 of 3)

Figure 7: Surface streamline pattern for 17.5 deg fin — Experiment

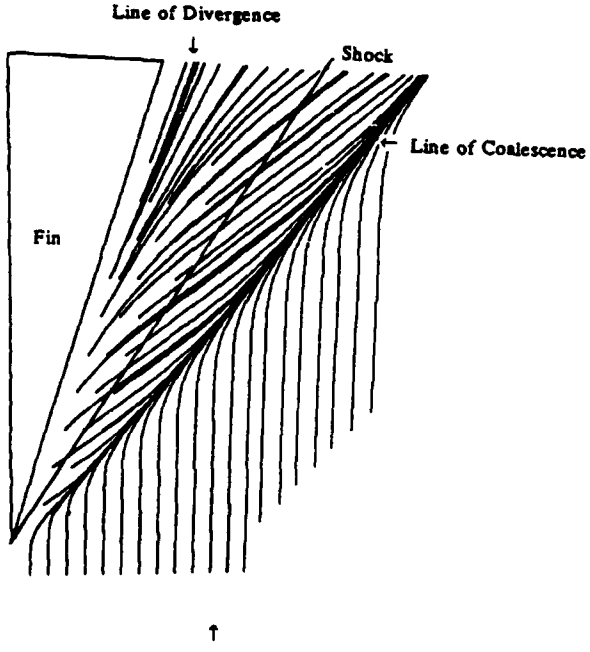

Figure 8: Surface streamline pattern for 17.5 deg fin — Theory

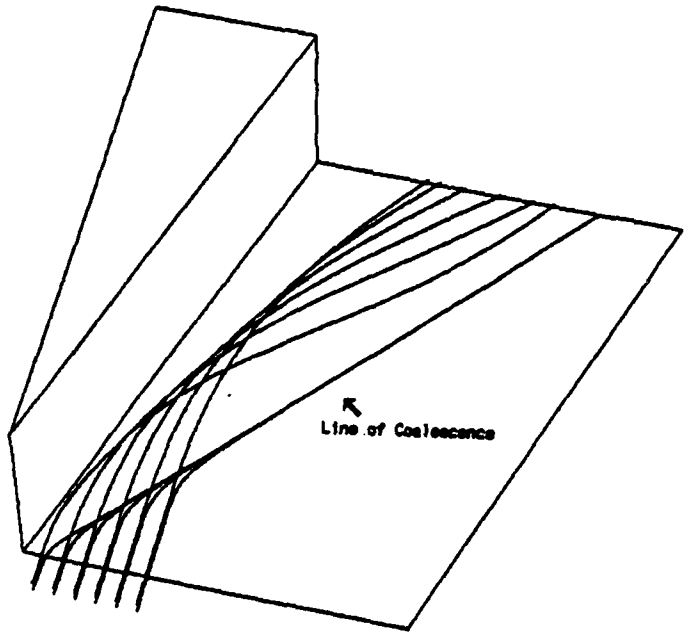

Figure 9: Particle traces for 17.5 deg fin — y = 0 and 0.5 δ_∞

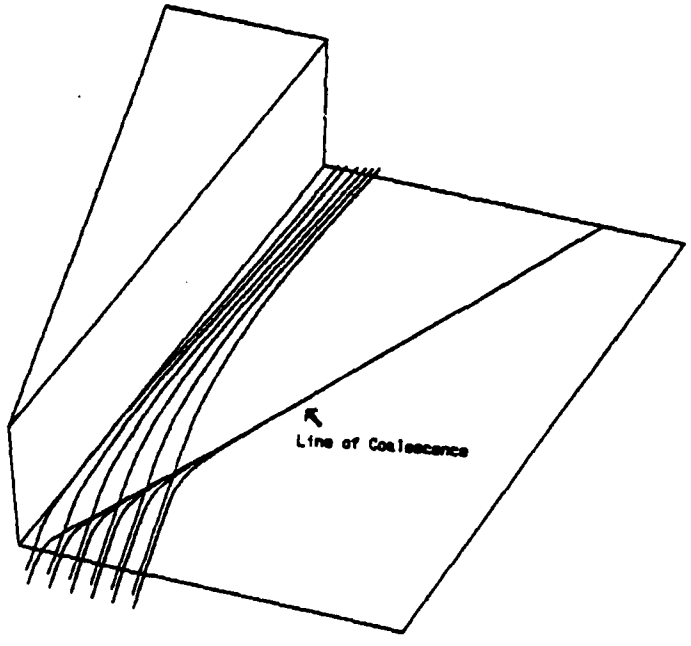

Figure 10: Particle traces for 17.5 deg fin — y = 0 and 1.1 δ_∞

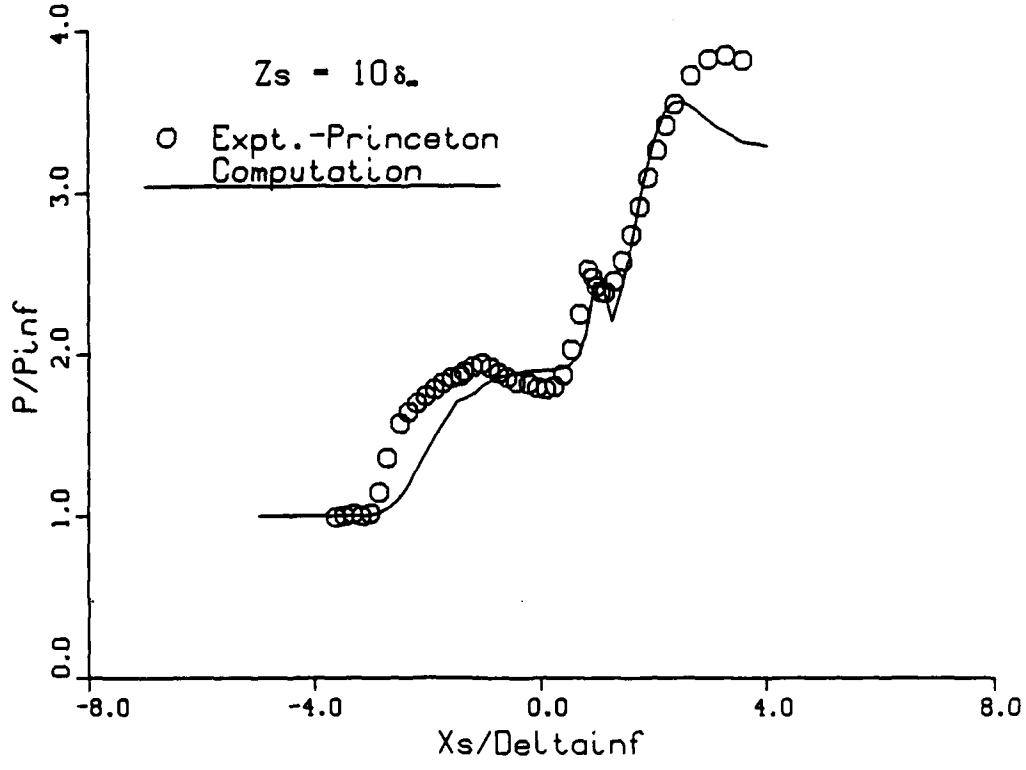

Figure 11: Surface pressure at $z_s = 10\delta_\infty$ for (30,60) corner

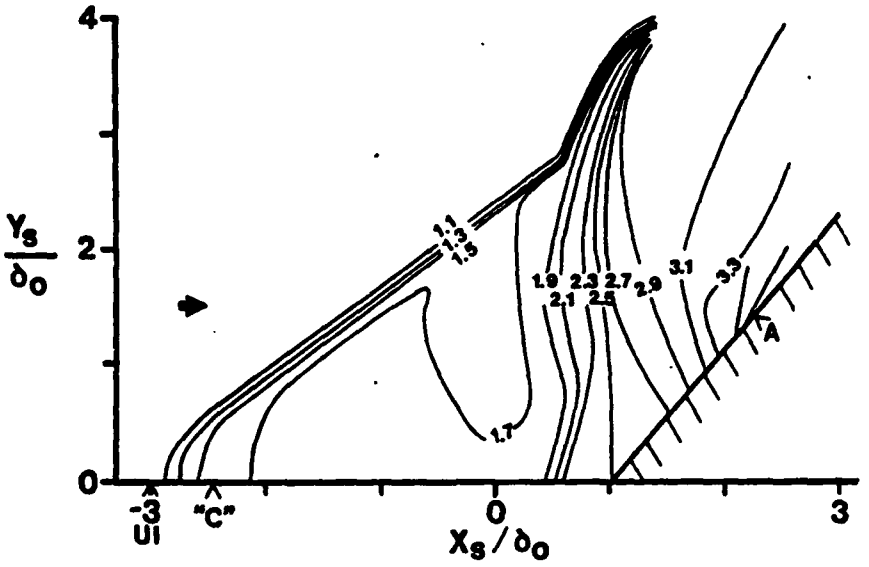

(a) Experiment

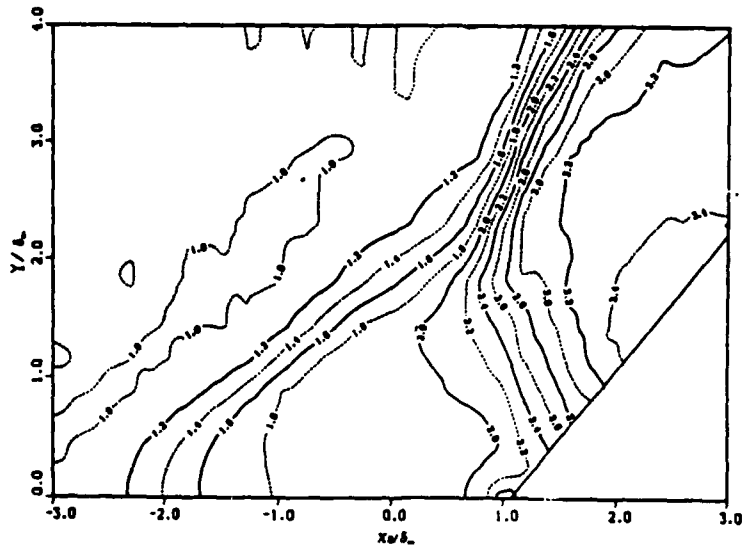

(b) Computed

Figure 12: Static pressure contour (30,60) Swept corner — $z_s = 10\delta_\infty$

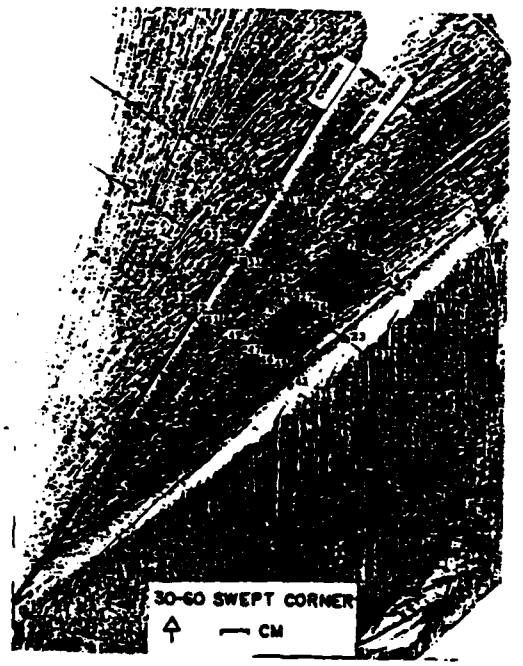

Figure 13: Surface streamline pattern for (30,60) corner — Experiment

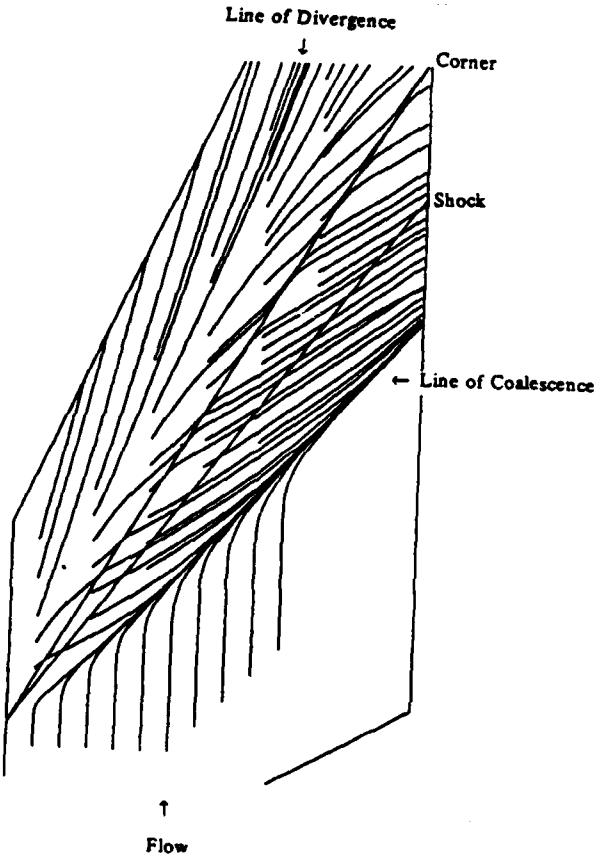

Figure 14: Surface streamline pattern for (30,60) corner — Theory

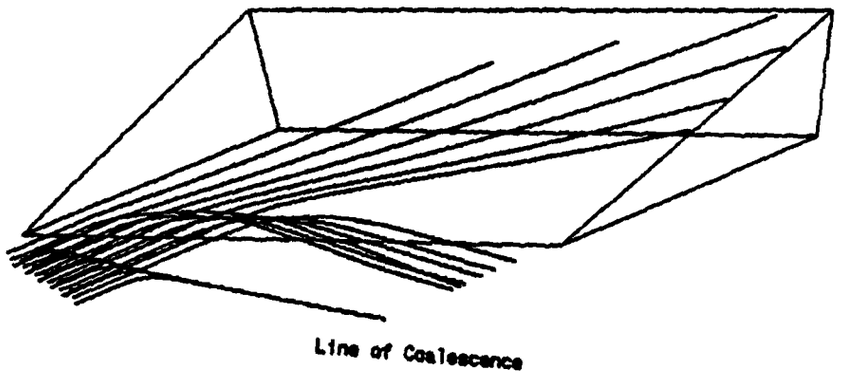

Figure 15: Particle traces for (30,60) Swept Corner (front view) – $y/\delta_\infty = 0, 0.5, 1.2$

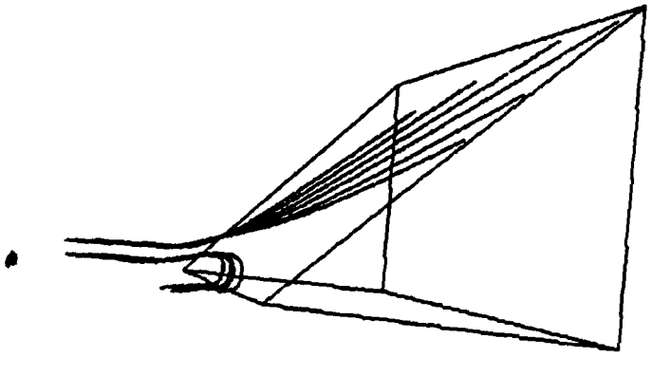

Figure 16: Particle traces for (30,60) Swept Corner (side view) – $y/\delta_\infty = 0.5, 1.2$

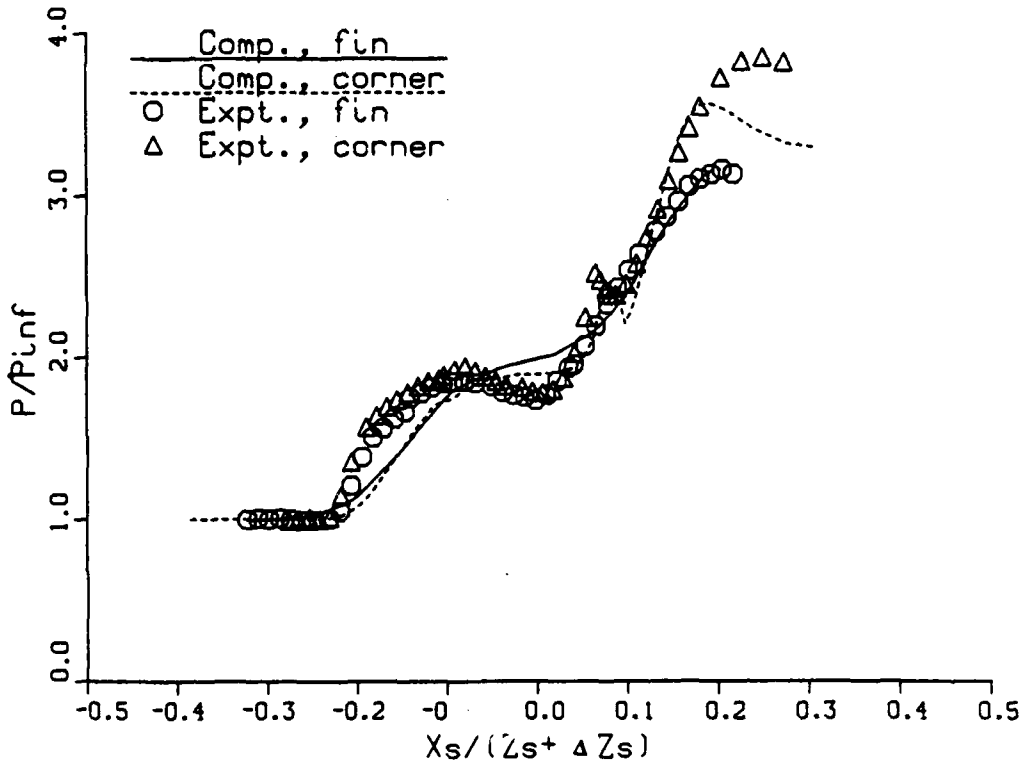

Figure 17: Surface pressure profiles for 17.5*deg* Fin and (30,60) Swept Compression Corner

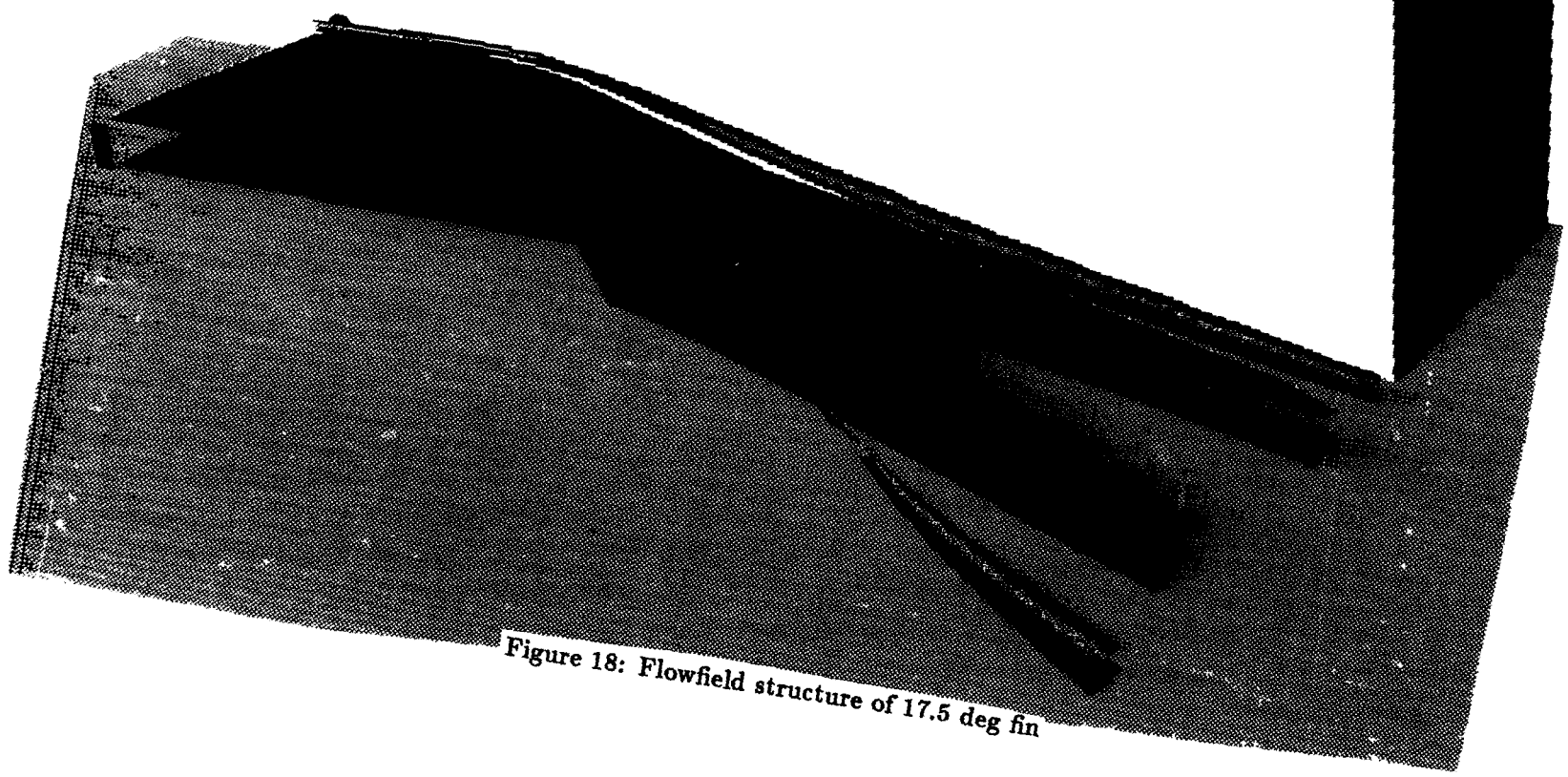

Figure 18: Flowfield structure of 17.5 deg fin

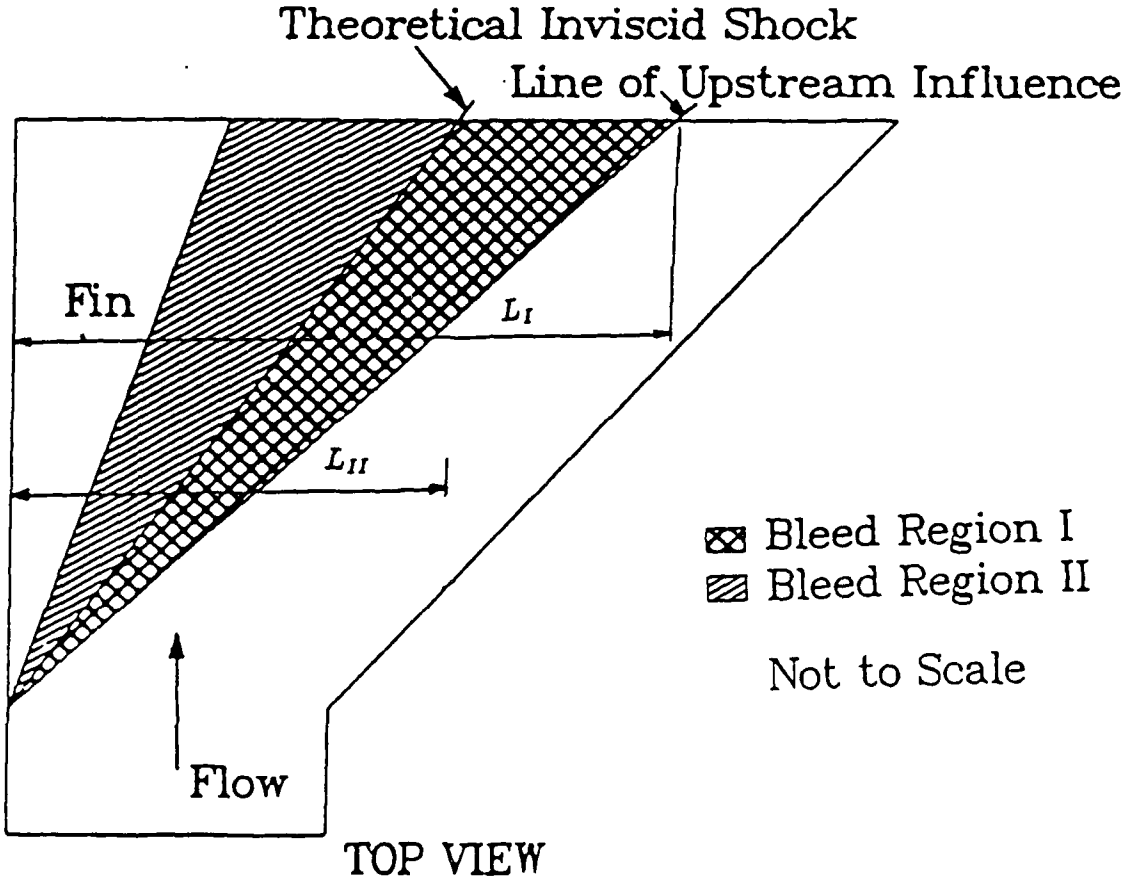

Figure 19: Bleed Regions — 20 deg Single Fin Configuration (SFC)

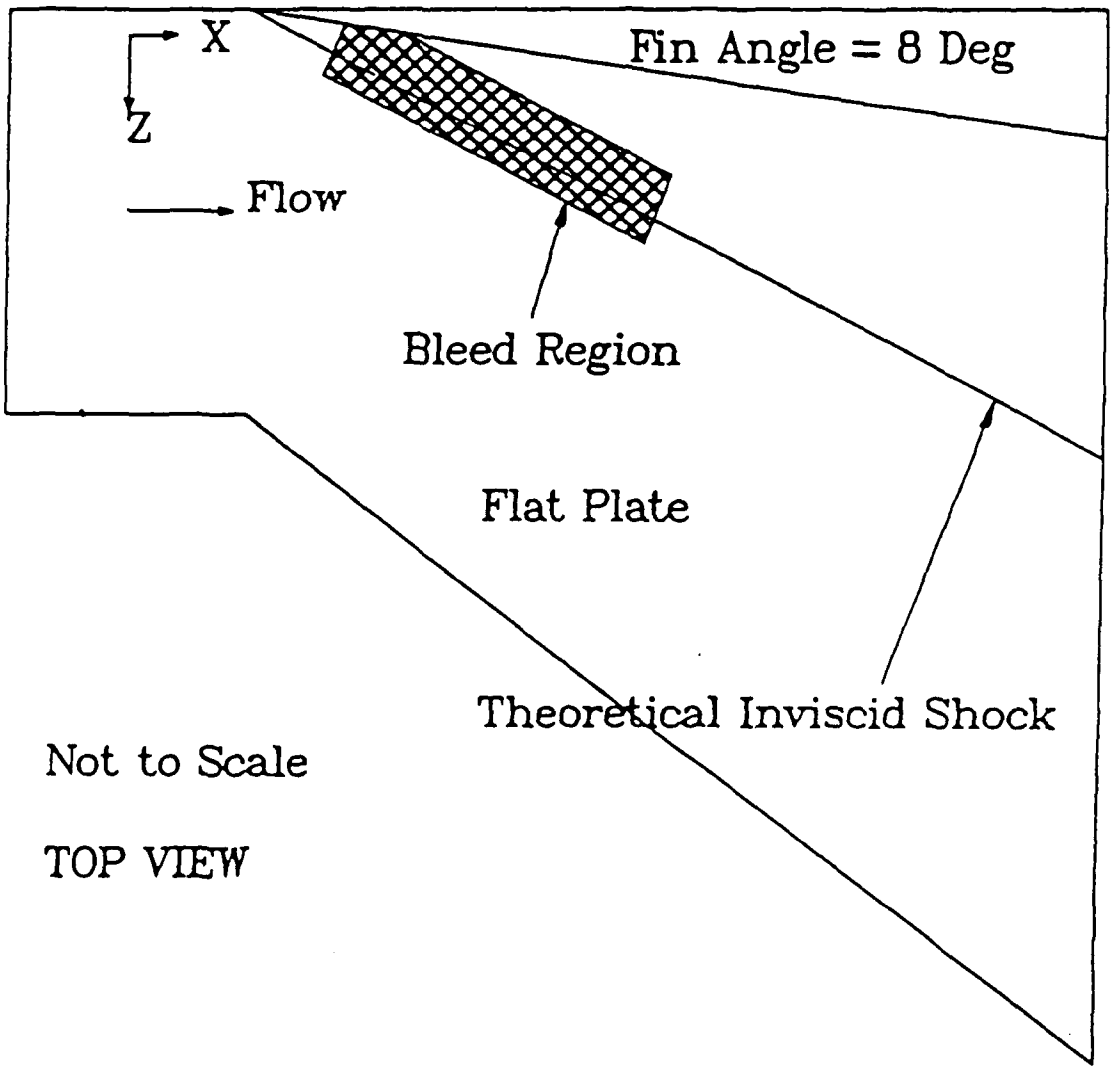

Figure 20: Bleed Regions — 8 deg Single Fin Configuration (SFC)

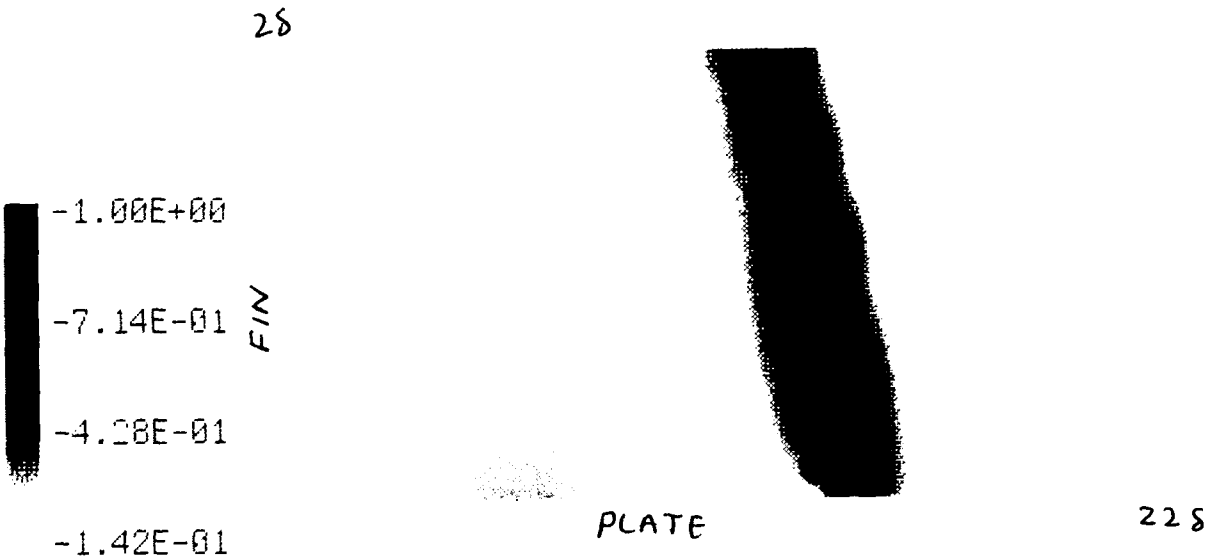

Figure 21: Pressure (inviscid) contribution for 20 deg fin – $x = 15\delta_\infty$

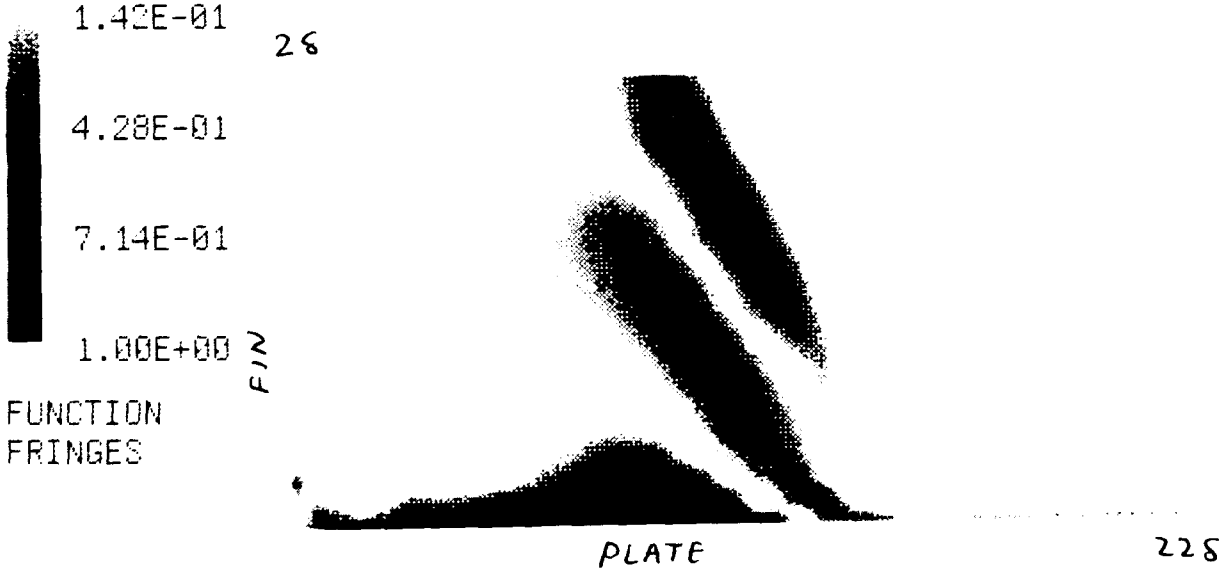

Figure 22: Viscous contribution for 20 deg fin – $x = 15\delta_\infty$

VII Papers

Paper A.

Numerical Investigation of Some Control Methods for 3-D Turbulent Interactions due to Sharp Fins

D. Gaitonde[12]
D. Knight[13]

Paper B.

Viscous/Inviscid Effects in 3-D Shock Wave-Turbulent Boundary Layer Interactions

N. Narayanswami[14]
D. Knight[15]

To be presented at the AIAA 27th Aerospace Sciences Meeting
Reno NV

[12]Graduate Student, MAE Dept, Rutgers University
[13]Professor, MAE Dept, Rutgers University
[14]Graduate Student, MAE Dept, Rutgers University
[15]Professor, MAE Dept, Rutgers University

Numerical Investigation of Some Control Methods for 3-D Turbulent Interactions due to Sharp Fins

Datta Gaitonde[1]
Doyle Knight[2]
Department of Mechanical and Aerospace Engineering
Rutgers University
P.O. 909, MAE
Piscataway, NJ 08855

Abstract

This paper describes continuing numerical research efforts on the modification and control of 3-D shock wave-turbulent boundary layer interactions due to supersonic flow past a sharp fin mounted on a flat plate. In supplement to previous numerical experiments (20° fin, Mach 3, $Re_\delta = 9 \times 10^5$), the effect of bleeding off roughly 5% & 8% of the incoming boundary layer from two distinct bleed regions is studied. Region I covers the area on the flat plate between the line of upstream influence (as determined by computed initial pressure rise) and the theoretical inviscid shock footprint (TISF) while Region II covers the remaining portion on the plate between the TISF and the base of the fin. Numerical pitot pressure and yaw angles are compared with experimental data obtained in the absence of bleed. The results indicate that the influence of both suction schedules on the overall flowfield and the previously observed vortical structure is remarkably modest with significant effects restricted to the region adjacent to the plate near the bleed region. In a separate computation, for an incipiently separated configuration (8° fin, Mach 3, $Re_\delta = 6.5 \times 10^5$), 23% suction is applied on an area across the shock corresponding to the experimental configuration of Barnhart *et al.* Comparison with experimental data and analysis of computed results indicates that the effect of bleed is primarily to reduce surface angularity and upstream influence. The major portion of the flow is not influenced by suction.

Following the conclusions of Mee and Stalker that shock-shock intersections may be capable of producing a given pressure rise with less likelihood of separation, a systematic study of symmetric double fin configurations is initiated. Two configurations with fin angles 4 deg × 4 deg and 8 deg × 8 deg respectively at Mach 2.95 and Reynolds number 2×10^5 are simulated. Results are presented in the form of surface streamlines, surface pressures and particle traces. The 4 × 4 configuration is a completely weak interaction for the domain under consideration. In contrast, the 8 × 8 configuration displays surface flow turning angles larger than the primary shock angle. The consequent separated flow is examined with particle traces.

1 Introduction

Research on 3-D shock wave - turbulent boundary layer interactions ("3-D turbulent interactions") finds utility in a number of high speed aerodynamic applications such as aircraft components. A supersonic inlet flowfield, for example, is characterised by a pattern of oblique shocks formed by the general curvilinear shape of the ramp and cowl surfaces, that interact with turbulent boundary layers on the walls. Dimensionless geometries such as the 3-D sharp fin (as in this research) and the 3-D swept compression corner are often employed to isolate the physics of such interactions from the geometrical complexity. The principal parameters for the sharp fin (Fig. 1) configuration are the Mach number M_∞, the Reynolds number, Re_{δ_∞} based upon the boundary layer thickness δ_∞ at the leading edge of the fin, the thermal boundary conditions and the fin angle α.

Progress has been achieved in analysing 3-D turbulent interactions with analytic, experimental and numerical techniques applied separately or in conjunction with each other. Analytical investigations have been restricted primarily to weak interactions in which, by definition, there is no separation [1, 2, 3, 4]. Such studies have provided valuable insight into the various scales involved in complex interactions resulting in better understanding of required resolution for numerical and experimental effort.

Experimental results in the form of surface pressures and surface flow visualizations have been available for over two decades[5, 6, 7, 8, 9, 10]. In recent years, improvements in instrumentation have made it possible to measure flow variables (such as pitot pressure and yaw angles) in the boundary layer as well [11, 12, 13,

[1]Graduate Student, Student Member AIAA

[2]Professor, Associate Fellow AIAA

14]. Measurements of skin friction by laser interferometry [15] have helped compare the accuracy of different eddy viscosity models. In addition to providing results of practical value, experimental observations provide a valuable benchmark for code validation.

The objective of current research efforts is to achieve the ability to not only predict variables of practical interest (surface pressures, skin friction and heat transfer rates), but also overall flow characteristics such as upstream influence, symmetricity (conical or cylindrical [16]), existence of separation and flow structures on various scales. With the advent of relatively easily accessible high-speed computers, computational research efforts have become a very cost-efficient means to "reduce the required [experimental] test matrix to the smallest number of configurations [17]".

Computations [18, 19, 20, 21, 22] typically employ the Reynolds averaged Navier-Stokes equations coupled with an algebraic [23] or two-equation [24] turbulence model. Numerical results for the sharp fin [14] and the swept compression corner [25, 26] have shown overall good agreement with experimental measurements, with modest local discrepancies in the prediction of upstream influence and skin friction values. Analysis of the computed flowfields confirm the principal flow feature — a large vortical structure aligned with the corner in agreement with the flowfield models of Token [27] and Kubota and Stollery [8]. A three dimensional surface of separation (Fig. 2) emanates from the line of coalescence (separation), and spirals into the vortical center. A second surface, emanating from upstream, intersects the wall at the line of divergence (attachment), and defines the extent of the fluid entrained into the vortical structure.

Such a flowfield – specifically the large vortical structure and separated flow – is undesirable in applications such as aircraft inlets whose function is to provide a nearly uniform subsonic flow with high total pressure recovery at the compressor face. The objective of this research work is to study possible perturbations to the boundary conditions which might influence the flowfield in a positive fashion and thus provide control. The need for boundary layer control studies has been recognized in the literature:

> Despite the obvious importance of boundary-layer control in high-speed air-breathing propulsion inlets, only two basic experimental studies of this problem involving swept interactions have been found in the literature both employing sharp fin shock generators [28].

Several possible methods of control may be proposed:

- Bleed (suction): Boundary layer suction serves to remove low speed fluid in the boundary layer before it separates from the surface. In inlets, suction is traditionally employed on the ramp, cowl and sidewalls to prevent flow separation in the vicinity of the intersection of the shock waves and walls.
- Blowing: Experimental results [12] at several Mach numbers indicate that tangential blowing is beneficial in retarding separation. The effect of blowing is to enhance the energy of the retarded boundary layer fluid.
- Shock-shock Interaction: Mee and Stalker [4] have theorised from an experimental study of weak shock-shock interactions with a turbulent boundary layer that intersecting shocks can produce a given overall pressure rise with less likelihood of separation than an equivalent strength single shock interaction.
- Modification of Geometry: It has been suggested that minor modifications in the 3-D configuration itself *may* exert significant influence. One proposal [29] envisages lifting the fin off the surface of the flat plate effectively permitting the flow to bleed off from the corner formed by the fin and the plate.
- Vorticity Modifications in Incoming Flow: Since the principal flow feature is a vortical structure, it may be possible to apply control through the introduction of additional vorticity in the longitudenal or spanwise direction.

This paper describes a continuing research effort focused on a numerical investigation of the first and third of these options. For suction, the *single fin configuration* (**SFC** - Fig. 1) is utilized. A series of computations on the 20° SFC, with porous suction over a triangular region extending from the line of upstream influence to the theoretical inviscid shock location (Region I in Fig. 3) has been described in previous literature [30]. The maximum bleed corresponded to removal of approximately 25 % of the upstream boundary layer. The computed streamline structure was observed to be essentially independent of the surface bleed flow rate, although the line of coalescence moved downstream toward the TISF and upstream influence was reduced. The effect of bleed was focused principally in a small fraction of the boundary layer. This represents a significant and surprising result and brings into question the efficacy of boundary layer bleed for sidewall interactions in high speed inlets. Numerical results of the application of bleed on a different area - the region on the plate between the TISF and the base of the fin (Region II in Fig. 3) are described in this paper (Section 6.1). The recent experiment of Barnhart *et al* [31] with suction on an incipiently separated configuration (8° SFC, Mach 3, $Re_{\delta_\infty} = 6.5 \times 10^5$) is not extensive enough to provide

general guidelenes. Nevertheless, their observation of beneficial effects of suction warrants numerical investigation (Section 6.2).

The second set of computations deals with crossed shock wave - turbulent boundary layer interactions. The concept of employing intersecting shocks (produced by the *s*ymmetric *d*ouble *f*in *c*onfiguration (**SDFC**) in Fig. 4) is based on the experimental observation that the limiting streamline deflection angles downstream of the reflected shocks are less than the angles downstream of the primary shock [32]. This concept is unproven, however, and additional computational and experimental research is required to determine its validity. It is emphasised that suction in *not* imposed in the double fin configurations. A calculation was performed previously [30] for the strongest intersecting shock configuration of Mee and Stalker corresponding to incoming Mach and Reynolds numbers 1.85 and 7.8×10^4 and symmetric sharp fins with angles of 5 deg each. The results indicated overall good agreement with experiment with one interesting anomaly that the computation overpredicted the extent of upstream influence by approximately 13%. This is in contrast to previous 3-D turbulent interaction studies [14] where computations have consistently underpredicted upstream influence. A more systematic study of stronger interactions is described in this paper. The Mach and Reynolds numbers are 2.95 and 2×10^5 respectively for symmetric fin angles of 4 deg and 8 deg. It is anticipated that equivalent experiments will be performed at the Princeton Gas Dynamics Laboratory in the future.

2 Governing Equations and Numerical Model

The governing equations are the full mean compressible Navier-Stokes equations using mass averaged variables and strong conservation form [33]. The molecular and turbulent Prandtl numbers are 0.73 and 0.9 respectively. Turbulence is modeled through the inclusion of the two-layer algebraic turbulent eddy viscosity model of Baldwin and Lomax [23] with the mixing length (l) as specified by the formula of Buleev [34]. The effect of bleed is incorporated through the bleed correction factor of Cebeci [35] as described in [30]. This turbulence model has been validated for a variety of boundary layer flows [36] with zero, favorable and adverse pressure gradients in the presence of suction.

A 3-D coordinate transformation is employed as in [14] to facilitate the application of the numerical algorithm and the boundary conditions. The hybrid explicit-implicit algorithm of Knight [33] is employed to solve the governing equations. The implicit algorithm employs Keller's Box scheme [37] and is applied to the asymptotic form of the Navier-Stokes equations (the sublayer equations) in a thin region (typically less than 1% of the boundary layer) adjacent to solid surfaces. The sublayer approximation has been validated for both 2-D [38] and 3-D [30] applications. The explicit algorithm of MacCormack [39] is applied to the full Navier-Stokes equations on grid points exterior to the computational sublayer. This includes nearly all of the boundary layer and the external inviscid region. The code has been employed successfully to predict turbulent interactions for the 3-D sharp fin [14], swept compression corner [25, 26] and the double fin configuration [30]. Computations described in this paper were performed either on the now decommissioned 4-pipe CYBER 205 at the NASA Ames Research Center or on the 2-pipe VPS-32 machine at NASA Langley Research Center.

3 Classification of Computations

Two configurations are utilised in this research — the SFC (Fig. 1) and the SDFC (Fig. 4).The single-fin configuration (SFC) is employed to study the effects of suction on the flowfield. None of the computations on the symmetric double-fin configuration (SDFC) incorporate suction. The attempt at control arises rather from the geometry itself since the vorticity generated by the two fins tends to counteract. For the purposes of the following discussion, the x-axis points in the general streamwise direction, y is plate normal and z is the spanwise axis. Also, the *theoretical* boundary layer thickness is utilised to scale distances for Cases A, B, C, F and G (see below). The *experimental* value is utilized for Cases D and E (Table 1).

3.1 Suction on SFC

In each case, a particular area (see below) is demarkated and the mass flux at each grid point in the area is specified as a ratio of the upstream freestream mass flux. The *b*leed *p*arameter, B.P. I,defined as follows:

$$\text{Bleed Parameter (B.P.) I} = \frac{\rho_w v_w}{\rho_\infty u_\infty} \qquad (1)$$

is utilised to characterize the magnitude of suction. In this equation, ρ is the density, u and v are the Cartesian components of the velocity in the streamwise and plate normal directions and subscripts w and ∞ indicate wall and freestream respectively. The implementation corresponds to *porous* bleed as opposed to *slot* bleed. The parameter B.P. I does not incorporate the area of bleed and therefore, provides only a local estimate of bleed magnitude. A more physical value may be computed by *approximating* the percentage of fluid in the incoming boundary layer bled off. This requires an estimate of the amount of incoming flow that actually "sees" the bleed region. This guess may be made in a simple manner by simply projecting the ray indicating start of suction on the upstream end of the domain. For example, for

Case	A	B	C	D	E	F	G
Configuration	SFC					SDFC	
Fin Angle (deg)	20			8		4 × 4	8 × 8
Bleed Region	—	I (Fig. 3)	II (Fig. 3)	—	Fig. 5	—	—
$\delta\|_{theory}$ (cm.)	1.3			3.1		0.4	
$\delta\|_{expt}$ (cm.)	1.40			3.11		0.38	
B.P. I	0.00	0.01	0.01	0.00	0.04	0.00	
B.P. II	0.00	0.05	0.08	0.00	0.23	0.00	
$Re_\delta\|_{th} \times 10^5$	8.8			5.6		2.6	
$Re_\delta\|_{ex} \times 10^5$	9.8			6.5		—	
M_∞	2.95						
P_t (kPa)	690			276		690	
T_t (K)	251			300		251	
T_w (K)	280			299		239	
Grid Details							
IL,JL,KL	32,48,32			40,48,32		75,48,32	
NSL_1	8						
NSL_2	8						
Computer Resources							
Computer	SYS I			SYS II		SYS I	
CPU(hrs)	4.2	3.6	6.7	10.5	12.5	24.9	28.3
Flow Time (T_c)	3.5	4.2	4.9	4.6	3.5	4.9	5.1

Legend: δ - Boundary layer thickness
B.P. - Bleed Parameter
IL,JL,KL - Points in x, y, z directions
M - Mach number
NSL_1 - Grid points in fin sublayer
NSL_2 - Grid points in plate sublayer
Re - Reynolds number
P_t - Total pressure
SFC - Single fin configuration
SYS I - 4-Pipe CYBER 205 (Ames)
SYS II - 2-Pipe VPS-32 (Langley)
T_c - Characteristic time ($= L/U_\infty$)
T_t - Total temperature
T_w - Wall temperature (fin and plate)

Table 1: Classification of Computations

Requirement	$z_1'^+ \ll 3$		$z_1'^+ N \ll 3$		$\frac{z_1'\dot{m}}{\mu_w} \ll 1$		$z_m'^+ \leq 60$		NPBL
	Avg.	Max	Avg.	Max	Avg.	Max	Avg.	Max	
Case A	1.47	3.03	1.47	3.03	0.00	0.00	47.4	97.4	16
Case B	1.47	3.01	1.46	3.01	0.30	0.41	50.4	97.0	16
Case C	1.99	4.21	1.62	3.03	0.37	0.41	59.3	135.3	16
Case D	0.89	2.10	0.89	2.10	0.0	0.0	28.6	69.4	16
Case E	1.10	5.02	0.91	2.18	1.42	1.44	35.26	161.6	16
Case F	0.91	1.01	0.91	1.01	0.0	0.0	19.1	21.2	16
Case G	1.05	1.20	1.05	1.20	0.0	0.0	19.4	24.3	16

Legend: $z_1'^+$ - First grid point from boundary in wall units
N - Bleed correction factor of Cebeci
$\dot{m}$ - Local bleed magnitude
μ_w - Molecular viscosity at wall
$z_m'^+$ - Height of sublayer in wall units
NPBL - Points in boundary layer

Table 2: Grid resolution requirements

Region I in Fig. 3, the boundary layer in distance L_I may be assumed to "see" the bleed region. B.P. II may be expressed as:

$$\text{B.P. II} = \frac{\int\int \rho_w v_w \mathrm{d}A_b}{L\int_0^\delta (\rho u)_{upstream} dy} = \frac{\int\int \rho_w v_w \mathrm{d}A_b}{(\delta - \delta^*)\rho_\infty u_\infty L} \quad (2)$$

where δ is the boundary layer thickness, δ^* is the displacement thickness, A_b is the area of bleed and L is the appropriate upstream distance. Two fin angles are utilised for bleed computations:

20 deg SFC

Case A corresponds to flow past the 20 SFC *without* bleed. For Cases B and C, 1% (= B.P. I) is imposed on Regions I and II (Fig. 3) respectively. The first region (Region I in Fig. 3) extends between the line of upstream influence and the TISF. The second region (Region II)extends between the TISF and the fin base. The bleed and flow parameters are presented in Table 1. Note that Cases A and B have already been described in [30] (identified there as the "no bleed" and "1% bleed" cases) and are included here only for comparison with Case C.

8 deg SFC

The recent experimental investigation by Barnhart *et al* [31] on the effect of suction on supersonic flow past an 8° SFC is numerically investigated in this research. The flow parameters are summarised in Table 1. Two computations are performed on this geometry, a *no bleed* case (Case D) and a case incorporating suction on the area displayed in Fig. 5 (Case E). As for the 20° SFC, bleed is imposed by specifying the bleed mass flux on the plate at each grid point in the bleed region. The relevant bleed parameters are provided in Table 1.

3.2 Flow past the SDFC

Computations are performed on two distinct SDFCs (Fig. 4) with fin angles 4 × 4 (Case F) and 8 × 8 (Case G). The overall flow parameters are listed in Table 1. The SDFC has two geometrical length scales — the separation between the fins (L_w in Fig. 4) and the length of the fins (L_{fin}). L_w is chosen to be 33.33δ in accordance with experimental considerations. The value of L_{fin} (69δ) is chosen such that for Case F, the inviscid secondary shock hits the fin at the trailing edge of the domain.

4 Boundary Conditions

The boundary conditions employed for both configurations are described together with reference to Figs. 1 and 4. The precise mapping from physical to computational domain is achieved with a computational grid described briefly in Section 5 and in detail in [40].

- Upstream boundary [ABHG]: The flow at this boundary (located 5δ upstream of the fin leading edge for Cases A,B,C,F & G, 4.6δ for Cases D & E)is assumed to be two-dimensional and is generated with a separate 2-D compressible boundary layer code [36] utilising the Baldwin-Lomax turbulent eddy viscosity model. For the SFC computations, the momentum thickness is matched while for the SDFC computations, the anticipated boundary layer thickness is matched.
- Plane of symmetry upstream of fin leading edge [AFLG]: Symmetry boundary conditions are applied at this boundary i.e., the normal component of the velocity and the normal derivatives of the remaining flow quantities are set to zero. For both the SFC and the SDFC,

$$w = 0; \frac{\partial(u, v, p, T)}{\partial \hat{n}} = 0 \quad (3)$$

  where, ρ is the density, u, v and w are the x,y, and z components of the velocity vector ($= \{u, v, w\}$), $\hat{n}$ is the normal to the boundary, p and T are the pressure and temperature respectively.
- Fin surface [LFKE]: Since this is a solid surface, the velocity vector and the normal pressure gradient are assumed zero and a fixed surface temperature is specified i.e.,

$$\rho\vec{v} = 0; \quad T = T_w; \quad \frac{\partial p}{\partial n} = 0 \quad (4)$$

  where the subscript w refers to wall conditions. The thermal boundary conditions employed for all cases are presented in Table 1.
- Flat plate [ABCDEF]: The two components of the velocity vector along the flat plate are specified zero. Bleed is applied in the appropriate areas for Cases B, C and E by specifying the quantity $\rho_w v_w / \rho_\infty u_\infty$ (B.P. I in Table 1). The normal pressure gradient is assumed zero and the surface temperature is fixed as for the fin surface (Table 1).

$$\rho v = \dot{m}; \quad u = w = 0; \quad T = T_w; \quad \frac{\partial p}{\partial n} = 0 \quad (5)$$

- Downstream boundary [EKJD]: In every case, the streamwise length of the physical domain is restricted so that the outgoing flow is supersonic (except close to the flat plate, of course) and as such, the zero gradient extrapolation condition ($\partial/\partial z = 0$) is applied. For Cases A,B and C, this boundary is located 26δ downstream of the fin leading edge. For Cases D and E this distance is 17.75δ and for Cases F and G, the value is 69δ.

- Right boundary [BCDJIH]: This boundary condition is treated separately for the SFC and the SDFC:
  - SFC: The boundary is assumed to be sufficiently far from the fin to ensure that the boundary layer is locally two-dimensional and therefore a simple gradient boundary condition $\partial/\partial z = 0$ is employed. This requires that the shock wave pass out the downstream boundary [EKJD].
  - SDFC: This is a symmetry boundary and the same conditions are applied as at the plane of symmetry upstream of the fin leading edge [AFLG].
- Top Boundary [HIJKLG]: This boundary is located far enough (roughly 8δ) away from the corner (formed by the plate and the fin) to permit the assumption of two-dimensional flow in planes parallel to the boundary. The boundary conditions applied are therefore:

$$\frac{\partial U}{\partial y} = 0 \qquad (6)$$

All boundary derivatives are implemented in single-sided first order accurate form.

5 Computational Details

Non-uniform Cartesian grids are employed in all calculations. The 3-D grid is composed of a set of streamwise (x = constant) planes (equally spaced with $\Delta x = \delta$ for all cases except D and E). Within each plane, two separate grid systems are employed — the "ordinary" and the "sublayer" grid [33]. The ordinary grid points adjacent to the plate and the fin are distributed using a combination of geometrically-stretched and uniform spacings in the general fashion of [20]. The number of grid points utilised, CPU and corresponding flow development time required for each case are presented in Table 1.

Adequate resolution of different regions of the flow impose various constraints on permissible grid sizes. A complete set of criteria for judging the acceptability of a grid system do not exist at present, except perhaps for the process of successive grid refinement which is generally not feasible for 3-D Navier Stokes calculations. The determination of the acceptability of a given grid system, must be based on experience and previous numerical computations [33]. The characteristics of the grids employed for every case satisfy constraints described in the literature in the average sense (see Table 2). The maximum values are localized in a few locations such as in bleed regions and at the fin leading edge, where the local skin friction τ_w shows steep increases (see Fig. 11 for example), making it unfeasible to satisfy all constraints locally. Previous computations with similar values have compared well with experiment [33].

Station	$\frac{x-x_s}{\delta_\infty}$	$\frac{z}{\delta_\infty}$	Station	$\frac{x-x_s}{\delta_\infty}$	$\frac{z}{\delta_\infty}$
1	-5.4	5.81	8	1.52	5.81
2	-4.4	5.81	9	2.6	5.81
3	-3.4	5.81	10	3.4	5.81
4	-2.4	5.81	11	-0.14	4.81
5	-1.4	5.81	12	-2.67	6.81
6	-0.4	5.81	13	-3.94	7.81
7	0.6	5.81	14	1.13	3.81

Table 3: Location of Experimental Surveys

6 Results

For the purpose of brevity, several results are presented without figures. A more detailed description of this work may be found in [40].

6.1 Suction on 20 deg. SFC

Computed results are first formally compared with available experimental data in the form of boundary layer pitot pressure and yaw angle profiles and surface pressures. Since no bleed is imposed in the experiments, direct comparison with theory is limited to Case A (no bleed). In the following discussion, the upstream boundary layer thickness δ_∞ (theoretical) is utilised to scale distances (cf. [13] for alternate scales). Streamwise distances (x), unless otherwise mentioned, are measured relative to the location of the inviscid shock (x_s) at the relevant spanwise (z) position. The distance normal to the flat plate is denoted y. Flow variables are normalised by their freestream values upstream of the interaction.

Effect of suction on Flow Variables

The fourteen experimental stations of Shapey and Bogdonoff [14] are located in the general shape of a cross (Fig. 6) with stations 1 and 2 located upstream of the interaction, 3 and 13 at about the line of upstream influence, stations 4, 5, 6 and 12 lie in Region I, while 7 through 11 and 14 lie in Region II. The coordinates of these stations are provided in Table 3. Experimental and numerical results available in the form of pitot pressure and yaw angle boundary layer surveys are compared at each of the above stations, although, for the purpose of brevity, only some plots (stations 3, 5, and 8) are presented here.

At stations 1 and 2 located upstream of the interaction, the pitot pressure and yaw angle profiles (not shown — see [40]) are unaffected by suction in either region and resemble profiles for 2-D boundary layer flows

as expected. The pitot pressure and yaw angles at station 3 are shown in Fig. 7 where the ordinate (y/δ) is the distance normal to the flat plate and the abscissa is the pitot pressure (Fig. 7 (a)), normalised by the freestream pitot pressure, or yaw angle in degrees (Fig. 7 (b)). A perceptible drop in pitot pressure because of bleed is evident at about $y/\delta = 0.1$ for Region I bleed in contrast to Region II bleed which shows negligible influence at this station. A similar conclusion may be drawn from the yaw angle profile. Region I bleed displays reduced yaw angles up to about $y/\delta_\infty = 0.8$ while Region II bleed has no significant effect. This general behavior is also seen at stations 4 (not shown) and 5 (Fig. 8) both of which lie upstream of Region II. At both these stations, whereas Region II bleed has no influence, Region I bleed exhibits a "cross-over" point, i.e., near the flat plate (up to about $y/\delta_\infty = 0.7$ for station 5) the pitot pressure increases above its no bleed value while, at larger distances from the plate, the pitot pressure is slightly lower. The yaw angles at both stations (4 and 5) are lower for Region I bleed with no effect of Region II bleed. At station 8 (Fig. 9), the pitot pressure for Region II bleed is larger very close to the flat plate accentuating the previously observed s shaped structure. In the major portion of the boundary layer however, the pitot pressure closely parallels the no bleed profile. Yaw angles for Region II bleed show no significant deviation from no bleed (Case A) values except in the free stream.

The computed wall pressure is compared with the experimental data of Goodwin [10] in Fig. 10 at the spanwise location $z/\delta = 5$. The ordinate is the static pressure normalised by the freestream static pressure. The abscissa is the streamwise distance (measured relative to the inviscid shock) normalised with δ_∞ . Comparison of Case A with experimental data indicates good agreement with regard to upstream influence. The experimental data indicates a plateau region at about $(x - x_s \sim 0)$ which is not adequately reproduced in the computation perhaps for reasons of grid resolution. The total pressure rise equals the expected theoretical value in the invisced region and is independent of bleed region and magnitude. The effect of Region I bleed (Case B) is evidently to reduce upstream influence thus reducing modestly the distance over which the pressure rise is achieved. Region II bleed (Case C) does not influence the upstream influence or the total pressure rise.

The localised effect of bleed on skin friction coefficient is exhibited in Fig. 11 at $z/\delta = 5$. For both bleed regions, local skin friction values display steep increases. It is apparent that a significant drag penalty is associated with the employment of suction.

Fig. 12 displays static pressure contours on the $z/\delta = 5.81$ plane. The high concentration of static pressure contours in the region away from the plate ($y/\delta > 3$) indicate the existence of the inviscid shock which is smeared over roughly three (3) grid points at this section. Near the plate, the shock wave forms two compression fans - an upstream (left) and a downstream (right) fan. The effect of bleed in Region I is evidently to reduce the size of the upstream fan. Region II bleed, on the other hand, has no significant effect on either fan.

Effect of Suction on Flowfield Structure

The computed solutions are utilised to examine the effect of bleed on the flow structure. Fig. 13 displays surface skin friction lines (often denoted "surface streamlines") for Cases A, B and C respectively. These are generated with a particle tracing code with the appropriate surface stresses replacing velocities. The location of the inviscid shock is indicated in each figure. The line of coalescence clearly persists for all cases. Whereas Region I suction (Fig. 13(b)) tends to align the line of coalescence with the theoretical inviscid line, Region II suction (Fig. 13(b)) has no significant influence despite the previously discussed steep local increase in skin friction values. This is another manifestation of the conclusion derived from the surface pressure plots, viz., Region II bleed has no effect on upstream influence.

A further analysis of the computed flowfield is carried out with particle traces employing a 3-D code [41]. Particles are "released" at various heights above the flat plate at the upstream boundary and their paths are plotted to study gross flow features. Fig. 14 shows traces of particles released at $y/\delta_\infty = 0.0001$, within the sublayer. For Case A, these particles coalesce to form the line of coalescence observed in the surface streamlines. For Case B, the particles are ingested by the plate in the region of bleed. Particles for Case C follow trajectories similar to those for Case A. Fig. 15 shows traces of particles released at $y/\delta_\infty = 0.6$. For both Cases A and B, the particles are entrained in the vortical structure. For Case C, those particles originating near the leading edge of the fin at the upstream boundary (small values of the spanwise coordinate z), are ingested by the flat plate in Region II (note the trajectories of the first seven particles from the fin leading edge). The other particles are swept into the vortical structure as for the other cases. It is evident that only those particles whose *no bleed* trajectory passes close to the flat plate (to within a certain height whose value is difficult to estimate) are ingested. To study the origin of the flow that is ingested by the plate in Case 5, a series of particles were released near the plate (in the bleed region) and their motion was traced *in reverse*. The traces are shown in Fig. 16. These particles generally originate near the fin leading edge. In the no bleed case, they would then have then risen up and around the vortical core. The above figures show clearly that the mean flowfield pattern continues

to be dominated by the vortical structure for both bleed regions.

6.2 Suction on 8 deg SFC

The geometrical configuration, bleed region and other significant parameters of the two computations (Cases D and E) on the 8° SFC are described in Fig. 5 and Table 1. As for the 20° SFC, results are first compared with experimental data and the flow is then examined with particle traces.

Comparison with Experiment

The experimental data utilised for comparison purposes was recorded at the NASA Lewis Research Center and is reported in Barnhart *et al* [31]. They utilise two Mach numbers, 2.48 and 2.95. For the latter, relevant to this research, results are published *only* in the presence of bleed and include surface (static pressures and wall flow angles) and boundary layer measurements (pitot pressure and yaw angles). Each of these is compared below with computed results.

It is important to note one fundamental distinction between the computed and experimental configuration. In the experiment, suction is applied by perforations on the plate in conjunction with a vacuum boost pump downstream of the suction plenum. Since the surface pressure increases into the interaction, the experimental bleed rate is variable, increasing generally in the streamwise direction at any given spanwise location. For lack of precise information on local bleed variation on the plate, the computation assumes a uniform bleed mass rate such that the total bleed mass rate over the entire bleed area matches experiment. It is expected therefore, that computed bleed values exceed experimental values in the vicinity of the upstream end of the bleed domain. The reverse situation may be expected at the downstream end. In the following discussion, distances are normalised with the *experimental* upstream boundary layer thickness ($\delta = 3.112cm.$). The term "experimental data" is assumed to imply *in the presence of bleed* since no data is available without suction for this configuration. The strict comparison is therefore restricted to Case E.

The computed (Case E only) and experimental surface pressures at four spanwise locations are plotted in Fig. 17. Note that the profiles at all locations collapse roughly on a single curve. Further, while the upstream pressures ($(x - x_s)/\delta \sim -4$) match well as expected, the computation displays significantly lower upstream influence. Experimental pressures begin to rise at $(x - x_s)/\delta \sim -1.5$ whereas the initial computed pressure rise occurs at $(x - x_s)/\delta \sim 0$, at the theoretical inviscid shock location. This discrepancy is partly attributable to the assumption of uniform bleed in the computation. Since the effect of bleed is to lower upstream influence, a higher local computed bleed value (over experiment) may be expected to result in a lower upstream influence. The maximum deviation ($\sim 25\%$) occurs near the location of the inviscid shock ($(x - x_s)/\delta \sim 0$) and beyond. Near the center of the suction region, the computed and experimental values match, resulting from a higher rate of pressure rise for the former. The overall pressure rise at the spanwise location ($Z = 2.46$) matches experiment and is only slightly lower (by $\sim 3\%$) than the theoretical pressure rise ($p_2/p_1 = 1.78$).

The comparison with experimental surface yaw values at the same spanwise locations is displayed in Fig. 18. The value α/θ is plotted on the ordinate where α is the turning angle and θ is the fin angle. Upstream of the interaction ($(x - x_s)/\delta \sim -4$), yaw angles are roughly zero. Within the interaction ($-3 < (x - x_s)/\delta < 2$), experimental values display considerable scatter and indicate a more gradual turning of the flow than does the computation. The discrepancy is again partly attributable to differences in local bleed rates. Computations predict lower turning angles at the upstream edge of the bleed region because local bleed values are higher than probably exist in experiment. Both computation and experiment display maximum turning angles lower than the shock angle (corresponding to the value 3.23 in Fig 18) although maximum experimental values exceed computed by roughly 15%. Note that maximum turning occurs behind the inviscid shock. Further downstream, computed values display turning angles twice the fin angle whereas experimental values approach the fin angle.

Fig. 19 exhibits the location of the nine experimental boundary layer surveys where pitot pressure and yaw angle profiles were measured. Fig 20 displays pitot pressure profiles at each of the nine stations. At station 1, upstream of the interaction, the experimental values (markers) match both the no bleed (solid line) and bleed (dotted line) cases and resemble a 2-D profile similar to that existing at the upstream end of the domain. At station 2, the curves are generally similar to those at station 1 although in the region between $0.3 < y/\delta < 1$, experimental values are slightly lower. At the upstream edge of the bleed domain (station 3), both computed and experimental values in the presence bleed display modestly lower values in the upper half of the boundary layer. At station 4, on the shock location, Case D displays a small pitot pressure overshoot. The effect of bleed is to increase pitot pressure values up to about $y/\delta \sim 0.3$ compared to the no bleed case, beyond which the values are lower. A similar observation was made previously for the 20° SFC (see Fig. 8 for example). The experimental results agree with Case E beyond $y/\delta > 0.3$ although closer to the plate, more

conformity is obtained with the no bleed case. A similar crossover of no bleed and bleed profiles is observed at station 5, the first station located downstream of the theoretical shock. Comparing Case E with experiment, in the region $0 < y/\delta < 0.8$, the computed values overpredict pitot pressure values. The situation is reversed higher into the boundary layer. At stations 6, 7, 8 and 9, the profiles all display similar qualitative behaviour. The "crossover" of bleed and no bleed profiles occurs successively higher into the boundary layer. In general, experimental values agree with Case E close to the plate although higher into the boundary layer, experimental values match no bleed results quite closely, indicating that the effect of bleed propagates higher into the boundary layer in the computation than in experiment.

The computed and experimental yaw angles are displayed in Fig. 21. At station 1, upstream of the interaction, yaw angles are negligible throughout the boundary layer as anticipated. At station 2, the effect of bleed is to lower yaw angle values below the no bleed values up to about $y/\delta \sim 0.5$. At the surface, computational values exceed experimental values. At the start of the bleed region (station 3), computed yaw angles for Case E assume small values through out the boundary layer although in the absence of bleed (Case D), the flow exhibits significant turning at this station. Experimental values lie between those for Cases D and E. Downstream of the inviscid shock (station 5), the correspondence between Case E and experiment is good with the computations tending to slightly underpredict yaw angles. The effect of bleed is to reduce yaw angles in the boundary layer by as much as $\sim 50\%$ at the surface. Further downstream, at station 6, although Case E displays lower yaw angles, experimental values parallel Case D more closely. At stations 7 and 8, located downstream of the bleed region, the effect of suction is more modest. The comparison between experiment and Case E is very good at station 7. Experimental observations display lower turning at close proximity to the plate at station 8. At station 9, located far downstream of the bleed region, the effect of bleed is restricted to the region $0 < y/\delta < 0.6$. The experimental values, which display significantly lower values at this location, are suspect since the angle obtained in the free stream is far lower than anticipated (equal to the fin angle since this station is downstream of the shock).

Analysis of Computed Flowfield

The overall effects of bleed are observed to be the same as for the previously discussed 20° SFC. Fig. 22 compares surface static pressure at two spanwise locations for Cases D and E. Upstream influence, determined by initial pressure rise, is reduced and the rate of pressure rise in the interaction increases with bleed. The total pressure rise remains the same. Local skin friction values (not shown) display steep increases in the bleed region and are not affected elsewhere. The effect of bleed on the shock structure is also similar to that observed for the 20° fin with Region I bleed. The effect of bleed is to completely eliminate the upstream fan resulting in a shock structure that appears entirely inviscid (not shown). No significant influence of bleed is observed in the inviscid regions.

The computed surface streamlines are displayed in Figs. 23 and 24 for Cases D and E respectively. For Case D, surface streamlines display maximum turning angles roughly equal to the shock angle. No clear line of coalesence is visible though the lines display bunching slightly upstream of the inviscid shock trace. For Case E, significant reduction in surface angularity is observed in the bleed region only. Streamlines originating near the fin leading edge follow trajectories similar to those for Case D. Upon reaching the bleed region however, they straighten out and move parallel to the upstream flow for a short distance gradually obtaining the shock angle downstream of the bleed region. Several lines passing through the furthermost upstream end of the bleed region form a single group of closely bunched lines passing out the extreme downstream end of the bleed region.

The flowfield is analysed with exhaustive sets of particle traces released at various heights above the plate. For brevity, only a few sets are discussed. Particles released within the sublayer ($y/\delta = 0.0001$) follow the general trajectory of the surface streamlines as anticipated (see Fig. 25 (a)) for Case D. In the presence of bleed however, particles are ingested (Fig. 25 (b)) at the leading edge of the bleed region if released appropriately close to the fin. Particles at larger spanwise distances escape the influence of suction. A similar pattern is observed up to about $y/\delta = 0.01$. Further into the boundary layer, at $y/\delta = 0.1$ (Fig. 26), Case D displays significant flow turning although the clear vortical structure observed for the 20° SFC does not exist. Several particles originating near the fin and whose no bleed trajectory passes over the bleed region are ingested in Case E roughly at the center of the bleed region. Particles released further from the plate ($y/\delta = 0.2$) are ingested at the trailing edge of the bleed region (not shown). Particles released at larger spanwise distances are not affected. At $y/\delta = 0.3$ (Fig. 27), none of the particles are ingested although the traces are slightly altered by suction and display modestly lower yawing. At $y/\delta = 1$ (Fig. 28), the effect of bleed is negligible.

6.3 Flow past double fin configurations

Both computations on the SDFC (see Table 1) are described together. Since experimental data is unavail-

able at this time, only computed results are discussed. Note that the domain length is identical for both the weaker (4 × 4) and the stronger (8 × 8) interactions. Hence, the free stream flow passes through a larger number of shock waves for the latter case.

Fig. 29 shows computed surface pressure contours plotted after symmetrically extending the flowfield. The theoretical pressure rise after each shock for both cases is presented in Table 4. These figures are qualitatively similar for the initial (primary) pressure rise though the pressure rises faster for the larger angle as is expected. Two types of contour lines exist - "⊂" and "⊃". Note that the switch from the one type to the other occurs at roughly the pressure ratio value associated with the relevant shock wave causing the pressure rise. The upstream influence at the line of symmetry is $\sim 15\delta$ for Case F and $\sim 12.5\delta$ for Case G. For the stronger (8 × 8) interaction, at the centerline near the trailing edge of the domain, the pressure rise is observed to reach a uniform rate. As explained later, the flow solution in this region exhibits strange behavior.

Fig. 30 shows computed surface streamlines for both cases. Case F exhibits a regular pattern devoid of any line of coalescence despite the fact that the total pressure rise after two shocks is roughly equal to that achieved with a single 8 deg fin. Outside of the region close to the fin leading edge, the minimum and maximum flow turning angles are −3.7 and 17.9 degrees respectively. The surface streamlines for Case G form an interesting pattern. Near the fin leading edge, surface turning angle roughly equal the shock angle resulting in a dense region of bunched lines. Surface streamlines at and near the line of symmetry do not display significant turning. Upon approaching the line of symmetry, the densely concentrated lines straighten out and move parallel to the centerline. Near the trailing edge of the domain, the two sets of lines from either side of the line of symmetry form a node-like structure. Due to the finite size of the grid, it is not clear if there are one or two nodes (slightly displaced from the line of symmetry). We believe at this time, that this structure is a numerical artifact. The overall accuracy of the solution near the trailing edge of the domain is questionable (see below) since the sublayer approximation assumes uniform mass flux within the sublayer region as imposed at the wall (zero in this case).

The computed flowfields are analysed with particle traces as for the single fin cases. The flowfield for Case F exhibits a simple structure as summarized in Fig. 31 which shows traces of particles released at $y/\delta_\infty = 0.1$ and $y/\delta_\infty = 0.5$. At the lower distance, the particles near the fin yaw more toward the centerline than those particles emanating from higher in the upstream boundary layer i.e., the spanwise displacement effect is larger near the base of the fin. As anticipated, this interaction does not exhibit separation.

Fig. 32 shows traces of particles released for Case G inside the sublayer at $y/\delta_\infty = 0.0001$. The particles follow the general behavior of the surface streamlines and form an unphysical stagnation point on the plate at the location corresponding to the node. Fig. 33 shows a sequence of particles released at various heights in the boundary layer. Particles released close to the plate but outside the sublayer ($y/\delta_\infty = 0.01$) also follow the general pattern of the surface streamlines up to the node at which point they rise and move parallel to the center line. Particles released in the vicinity of the line of symmetry at various heights move parallel to it (as expected from the imposed boundary conditions) but rise up and away from the plate to form an arch-like trace at the downstream end of the domain. Particles released near the fin at small values of y/δ_∞ pitch toward the plate and yaw toward the line of symmetry straightening out as they approach it. At higher distances from the plate, particles released near the fin pitch toward the plate over the particles beneath yawing toward the centerline. The arch-like structure formed by the particles released near the centerline broadens so that the overall flow approaches the boundary layer flow (due to the fin) expected at large distances from the plate.

7 Conclusions

The effect of suction on the supersonic flow past the SFC is investigated. Two fin angles 20 deg and 8 deg are considered, both at Mach 3. The former represents a strong interaction for which the existence of the vortical structure has been previously demonstrated. The latter is an incipiently separated configuration for which experimental data incorporating suction is available. For the 20 deg fin, bleed is applied on two regions on the plate jointly spanning the region between the line of upstream influence and the base of the fin. For the 8 deg fin, the area of suction considered is roughly rectangular and covers a strip on either side of the theoretical shock foot print.

For both interaction strengths, surface turning angles are generally lower than for the equivalent no bleed case. For the stronger interaction, the line of coalesence persists for all suction magnitudes and areas considered. Since the weaker interaction does not display a clear line of coalescence in the absence of bleed, an equivalent statement cannot be made. Detailed examination of the flow indicates that the width of the upstream compression fan formed by the shock wave near the plate is significantly reduced for Region I bleed, for which upstream influence is also reduced and the rate of pressure rise on the plate is higher although the total pressure rise remains roughly the same. Local skin friction val-

	Upstream	After			
		Shock 1	Shock 2	Shock 3	Shock 4
	Case F/Case G	F/G	F/G	F/G	F/G
Mach No	2.95/2.95	2.75/2.56	2.40/2.22	2.23/1.91	2.08/1.63
$\frac{p}{p_\infty}$	1.0/1.0	1.35/1.78	1.78/2.97	2.32/4.72	2.98/7.17

Table 4: Theoretical pressure rise after shocks - Cases F and G

ues display steep increases above no bleed values. For the stronger interaction, the vortical structure persists. The effect of suction is to ingest particles approaching the bleed area without affecting the overall flow field in any significant fashion.

The flow past the symmetric double fin configuration is computed for a weak and a strong interaction. The weak interaction (4 × 4 at Mach 3) displays a relatively simple flow structure without the existence of separation. The flow past the 8 × 8 SDFC exhibits separation upstream of the primary shock with significant flow motion away from the plate. Surface flow turning angles exceed the inviscid shock angle. Flow traces indicate that particles released at the same height at the upstream end of the domain form an arch-like structure at the downstream end with the flow near the plane of symmetry moving furthest away from the plate.

Acknowledgements This research was sponsored by the Air Force Office of Scientific Research under AF Grant # 86-0266 monitored by Dr. James McMichael and Dr. Len Sakell. The authors would like to thank Dr. C.C. Horstman for many helpful discussions. The computations described were performed at the NASA Research Centers at Ames and Langley. The assistance of the staff at both centers is gratefully acknowledged.

REFERENCES

[1] G. Inger. Supersonic Viscous-Inviscid Interaction of a Swept Ramp with a Turbulent Boundary Layer. *AIAA Paper 85-1669*, 1985.

[2] G. Inger. Incipient Separation and Similitude Properties of Swept Shock/Turbulent Boundary Layer Interactions. *AIAA Paper 86-0345*, 1986.

[3] R. Stalker. Spanwise Propagation of Disturbances in Swept Shock Wave - Boundary Layer Interactions. *AIAA Paper 82-0988*, 1982.

[4] D. Mee and R. Stalker. Investigation of Weak Shock-Shock and Shock-Expansion Intersection in the Presence of a Turbulent Boundary Layer. *AIAA Paper 87-0549*, 1987.

[5] A. Stanbrook. An Experimental Study of the Glancing Interaction Between a Shock Wave and a Boundary Layer. In *British ARC CP-555*, July 1960.

[6] A. McCabe. The Three-Dimensional Interaction of a Shock-Wave with a Turbulent Boundary Layer. *The Aeronautical Quarterly*, 17:231–252, 1966.

[7] C. Law. *Three-Dimensional Shock Wave/Turbulent Boundary Layer Interactions at Mach 6.* Technical Report TR-75-0191, ARL, 1975.

[8] H. Kubota and J. Stollery. An Experimental Study of the Interaction Between a Glancing Shock Wave and a Turbulent Boundary Layer. *J. Fluid Mech.*, 116:431–458, 1982.

[9] D. Dolling and S.M. Bogdonoff. Upstream Influence in Sharp Fin Induced Shock Wave Turbulent Boundary-Layer Interactions. *AIAA Journal*, 21:143–145, January 1983.

[10] S. Goodwin. *An Exploratory Investigation of Sharp-Fin Induced Shock Wave/Turbulent Boundary Layer Interactions at High Strengths.* Master's thesis, Princeton University, 1984.

[11] B. Oskam, I. Vas, and S. Bogdonoff. An Experimental Study of 3-D Flowfields in an Axial Corner at Mach 3. *AIAA Paper 77-689*, 1977.

[12] D. Peake. *Three-Dimensional Swept Shock/Turbulent Boundary Layer Separations with Control by Air Injection.* Technical Report Aero. Report No. LR-592, National Research Council - Canada, 1976.

[13] W. McClure and D. Dolling. Flowfield Scaling in Sharp Fin-Induced Shock Wave Turbulent Boundary Layer Interaction. *AIAA Paper 83-1754*, 1983.

[14] D. Knight, C. Horstman, B. Shapey, and S. Bogdonoff. The Flowfield Structure of the 3-D Shock Wave - Boundary Layer Interaction Generated by a 20 Deg. Sharp Fin at Mach 3. *AIAA Journal*, 25(10):1331–1337, October 1987.

[15] K-S. Kim and G. Settles. Skin Friction Measurements by Laser Interferometry in Swept Shock Wave/Turbulent Boundary Layer Interactions. *AIAA Paper 88-0497*, 1988.

[16] G. Settles and H-Y. Teng. Cylindrical and Conical Flow Regimes of Three-Dimensional Shock/Boundary-Layer Interactions. *AIAA Journal*, 1984.

[17] G Paynter. Current Status of Inlet Flow Prediction Methods. In *12th U.S.Navy Symposium on Aeroballistics*, David Taylor Naval Ship Research and Development Center, Bethesda, Maryland, May 1982.

[18] R. MacCormack. *Numerical Solution of the Interaction of a Shock Wave with a Laminar Boundary Layer.* Lecture Notes in Physics, Vol. 8 Springer-Verlag, pp. 151-163, 1971.

[19] C. Horstman and C. Hung. Computation of Three-Dimensional Turbulent Separated Flows at Supersonic Speeds. *AIAA Paper 79-0002*, 1979.

[20] D.D. Knight. A Hybrid Explicit-Implicit Numerical Algorithm for the Three-Dimensional Compressible Navier-Stokes Equations. *AIAA Journal*, 22:1056–1063, August 1984.

[21] D.D. Knight. Calculation of Three Dimensional Shock/Turbulent Boundary Layer Interaction. *AIAA Journal*, 12:1885–1893, December 1985.

[22] D.D. Knight. *Modelling of Three-Dimensional Shock Wave Turbulent Boundary Layer Interactions.* Macroscopic Modelling of Turbulent Flows, Lecture Notes in Physics, 230, Springer-Verlag, pp. 177-201, 1985.

[23] B. Baldwin and H. Lomax. Thin Layer Approximation and Algebraic Model for Separated Flows. *AIAA Paper 78-257*, 1978.

[24] W. Jones and B. Launder. The Prediction of Laminarization with a Two-Equation Model of Turbulence. *Int. J. Heat and Mass Transfer*, 15:301–304, 1972.

[25] D. Knight, C. Horstman, R. Ruderich, M-F. Mao, and S. Bogdonoff. Supersonic Turbulent Flow Past a 3-D Swept Compression Corner at Mach 3. *AIAA Paper 87-0551*, 1987.

[26] D. Knight, D. Raufer, C. Horstman, A. Ketchum, and S. Bogdonoff. Supersonic Turbulent Flow Past a Swept Compression Corner. *AIAA Paper 88-0310*, 1988.

[27] K. Token. *Heat Transfer Due to Shock Wave/Turbulent Boundary Layer Interactions in High Speed Weapons Systems.* Technical Report TR-74-77, AFFDL, 1974.

[28] G. Settles and D. Dolling. Swept Shock Wave Boundary-Layer Interactions. *Tactical Missile Aerodynamics, AIAA Progress in Astronautics and Aeronautics Series*, 104:297–379, 1986.

[29] S. Bogdonoff. *Private Communication.* Princeton University, 1987.

[30] D. Gaitonde and D. Knight. Numerical Experiments on the 3-D Shock Wave - Boundary Layer Interaction Generated by a Sharp Fin. *AIAA Paper 88-0309*, 1988.

[31] P.J. Barnhart, I. Greber, and W.R. Hingst. Glancing Shock Wave-Turbulent Boundary Layer Interaction with Boundary Layer Suction. *AIAA Paper 88-0308*, 1988.

[32] D.J. Mee. *Experiments Involving the Interactions of a Turbulent Boundary Layer with Single and Intersecting Fin-Induced Swept Shock Waves and Swept Expansion Fans.* Technical Report 11/86, Department of Mechanical Engineering, University of Queensland, Australia, 1986.

[33] D. Knight. *A Vectorized Three-Dimensional Navier-Stokes Code for High Speed Inlets.* Technical Report RU-TR-161-MAE-F, Rutgers University, New Brunswick, New Jersey, 1983.

[34] N. Buleev. *Theoretical Model of the Mechanism of Turbulent Exchange in Fluid Flows.* Technical Report 957, AERE, Hartnell, England, 1963.

[35] T. Cebeci and A.M.O. Smith. *Analysis of Turbulent Boundary Layers.* Academic Press, 1974.

[36] B. York. *Evaluation of the Baldwin-Lomax Turbulence Model for a Class of Boundary Layer Flows.* Master's thesis, Rutgers University, 1984.

[37] H. Keller. Accurate Difference Methods for Nonlinear Two-Point Boundary Value Problems. *SIAM J. Numerical Analysis*, 11:305–320, 1974.

[38] D.D. Knight. Improved Calculation of High Speed Inlet Flows - Part I: Numerical Algorithm. *AIAA Journal*, 19:34–41, January 1981.

[39] R. MacCormack. Numerical Solution of the Interaction of a Shock Wave with a Laminar Boundary Layer. *Lecture Notes in Physics*, 8:151–163, 1971.

[40] D. Gaitonde. *Numerical Investigation of Some Control Methods for 3-D Turbulent Interactions due to Sharp Fins.* PhD thesis, Mechanical and Aerospace Engineering, Rutgers University, January 1989 (expected).

[41] D. Raufer. *The Development of a 3-D Particle Tracing Algorithm and its Application to the Study of Swept Compression Corner Boundary Layer Interactions.* Master's thesis, Rutgers University, December 1987.

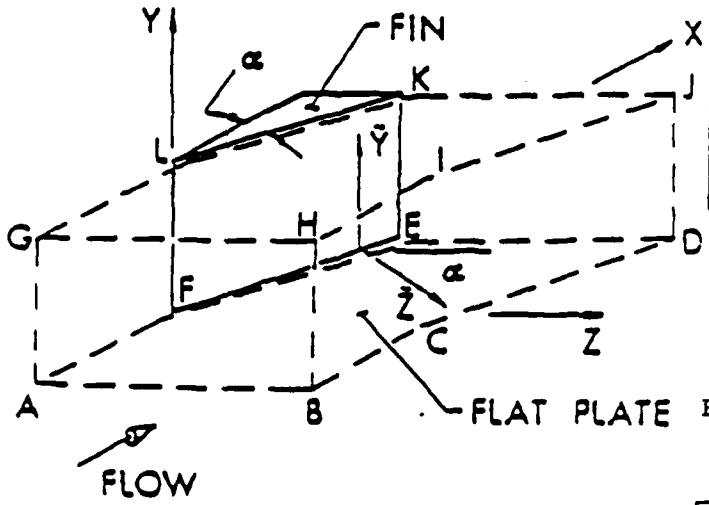

Figure 1: Sharp Fin Configuration (SFC)

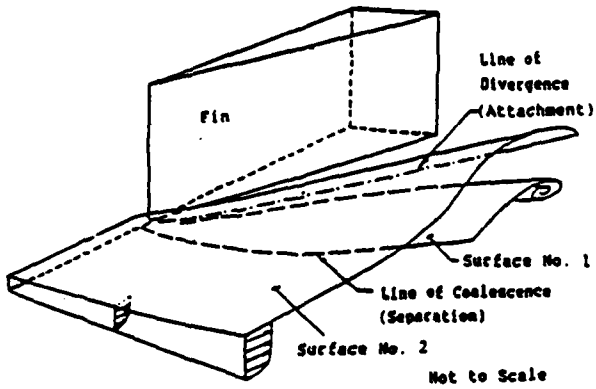

Figure 2: Mean Flowfield Structure for SFC

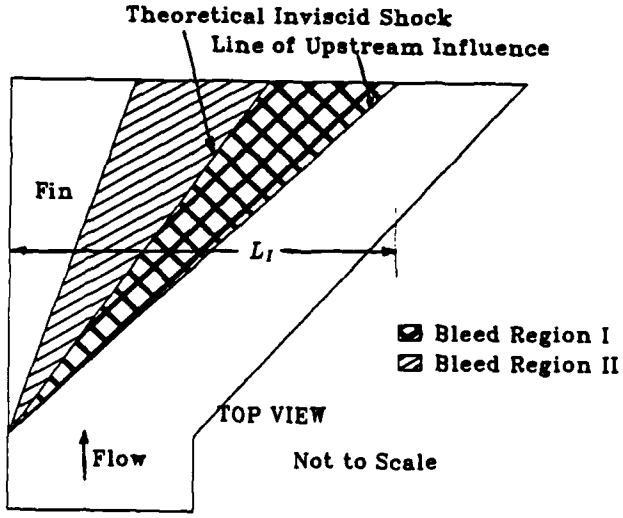

Figure 3: Bleed Regions – 20° SFC

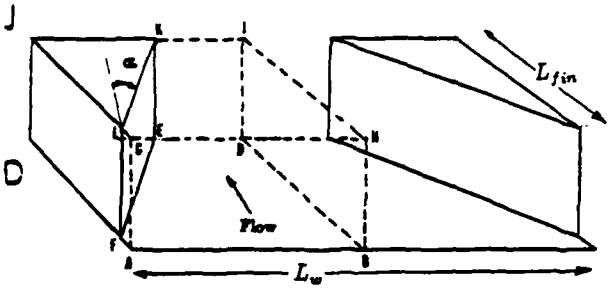

Figure 4: Symmetric Double Fin Configuration (SDFC)

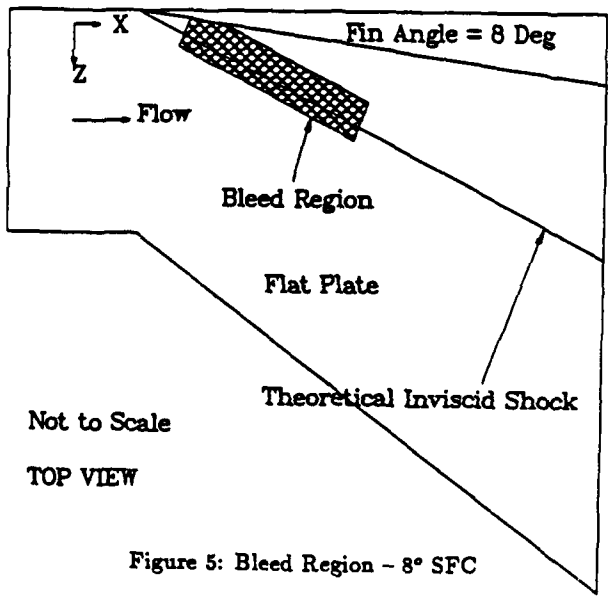

Figure 5: Bleed Region – 8° SFC

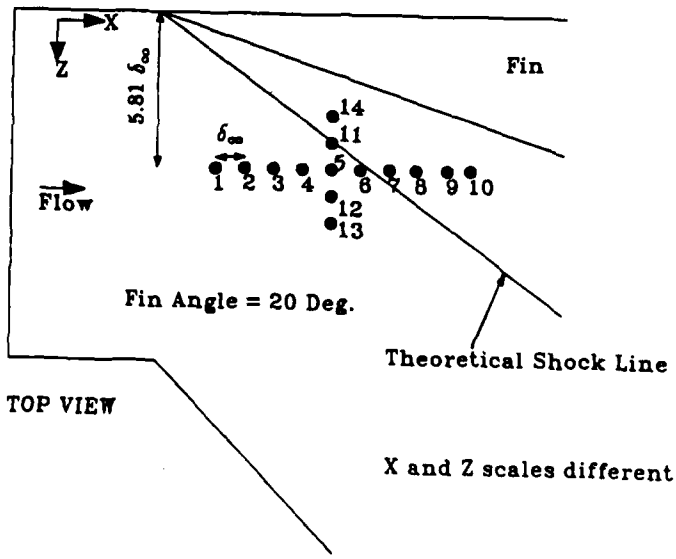

Figure 6: Experimental Locations of Shapey and Bogdonoff – 20° SFC

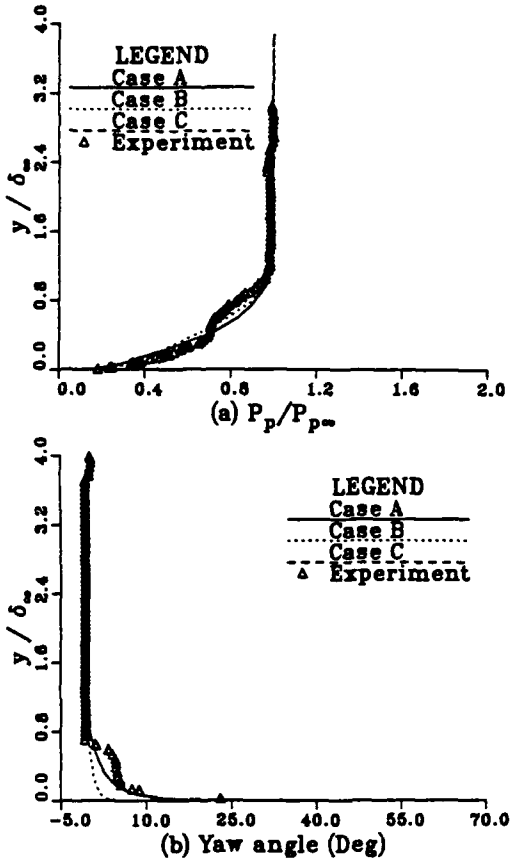

Figure 7: Pitot pressure and Yaw Angles — Station 3 (20° SFC)

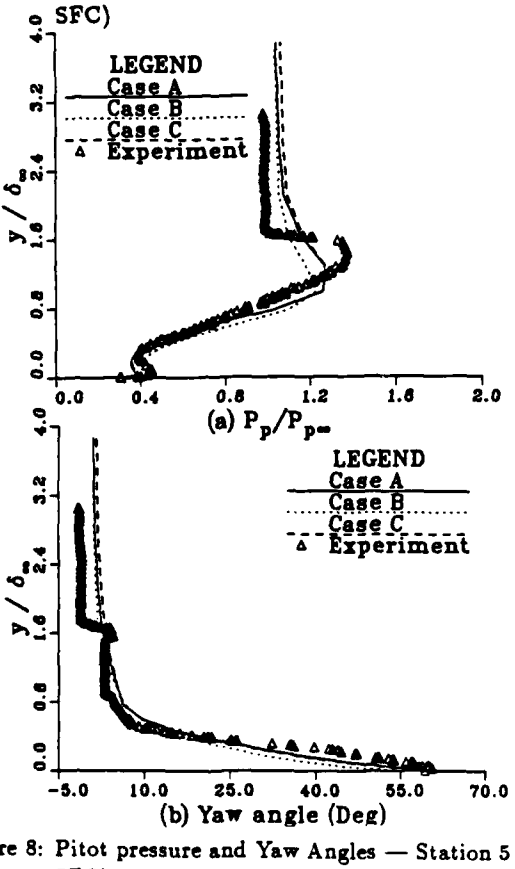

Figure 8: Pitot pressure and Yaw Angles — Station 5 (20° SFC)

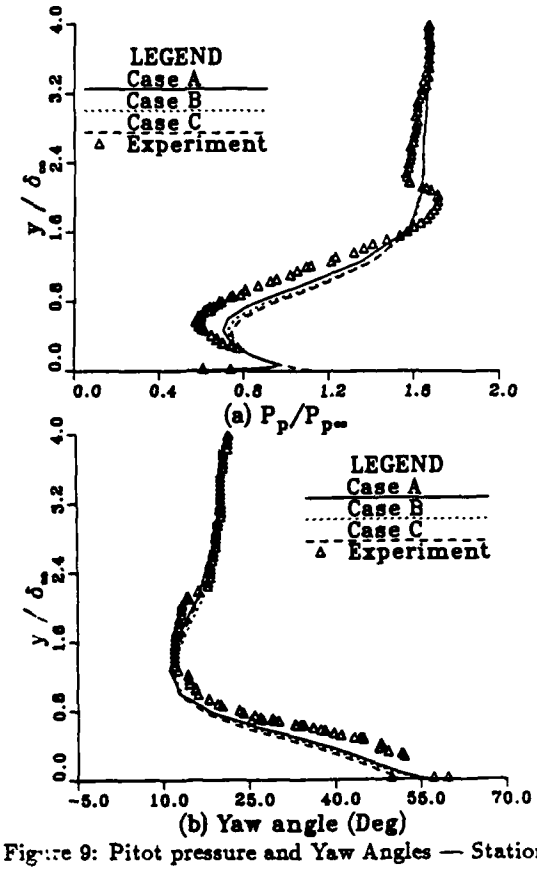

Figure 9: Pitot pressure and Yaw Angles — Station 8 (20° SFC)

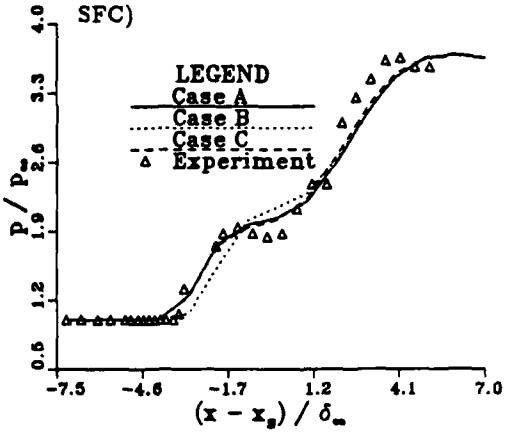

Figure 10: Surface pressure — $z/\delta = 5$ (20° SFC)

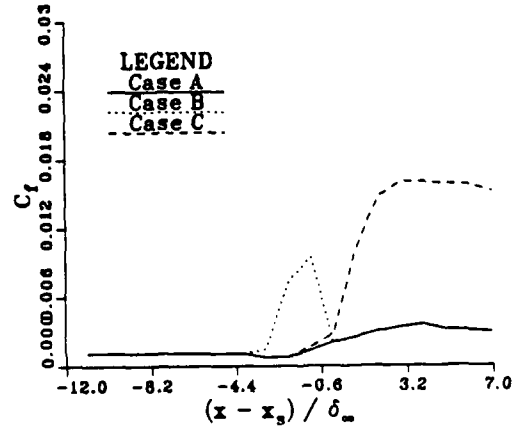

Figure 11: Skin Friction Coefficient — $z/\delta = 5$ (20° SFC)

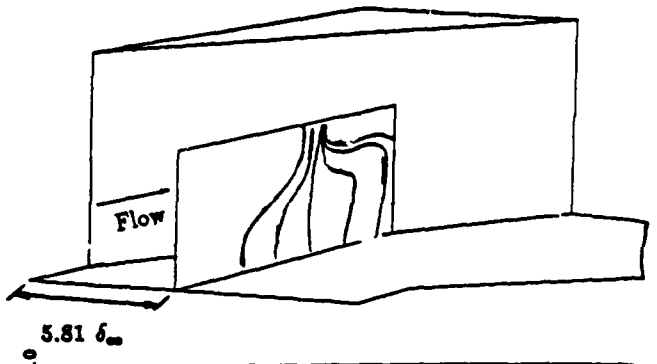

5.81 δ_{∞}

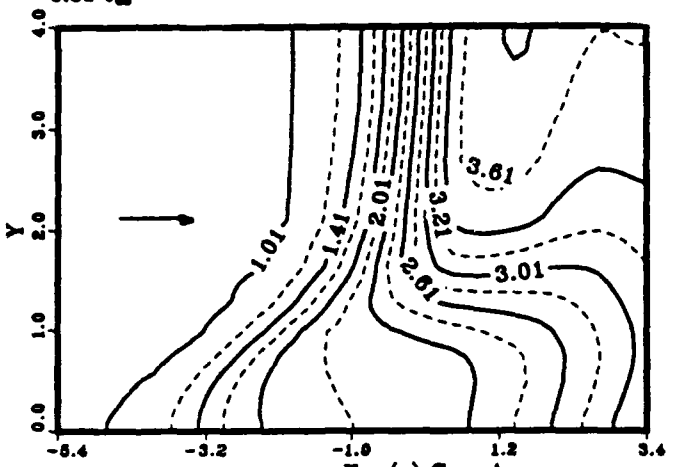

(a) Case A

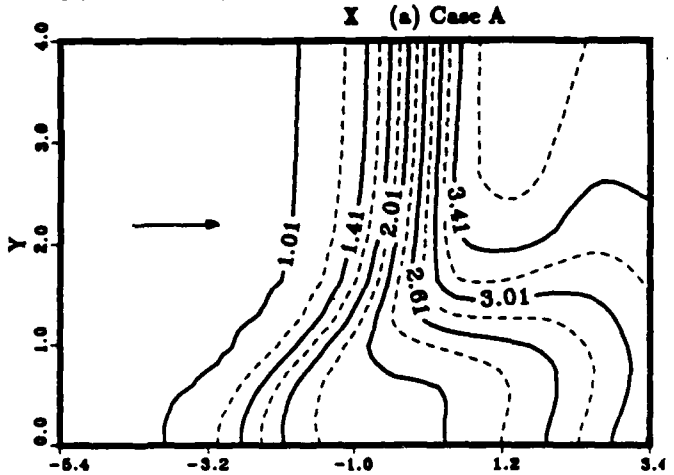

(b) Case B

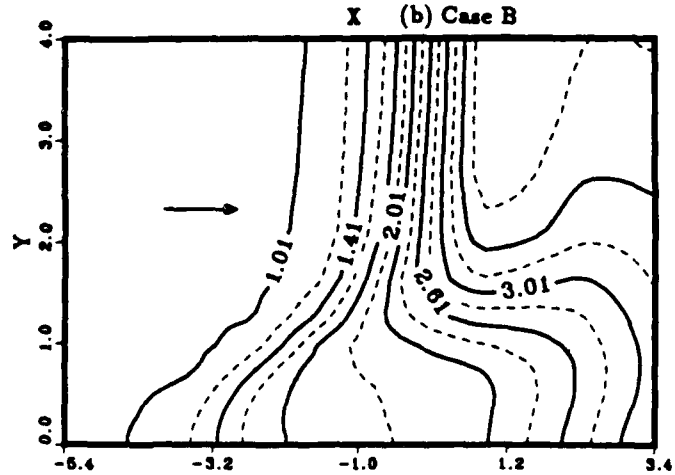

(c) Case C

Figure 12: Static pressure contour plots — $z/\delta = 5.81$ (20° SFC)

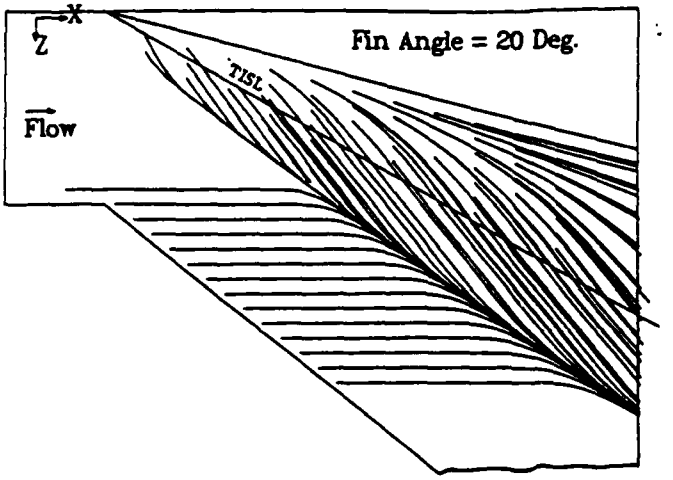

(a) Case A

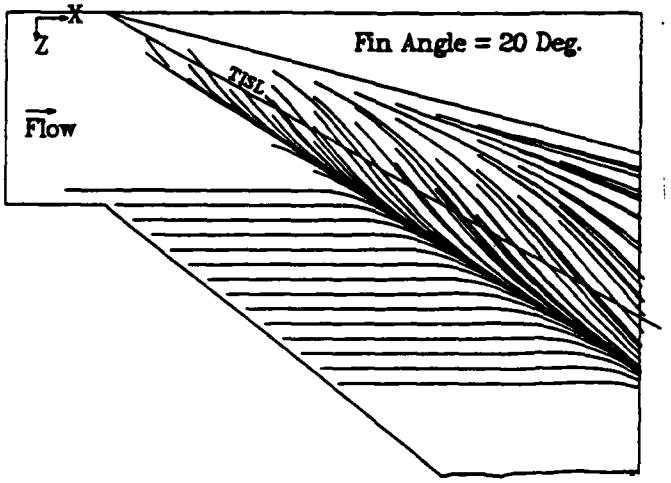

(b) Case B

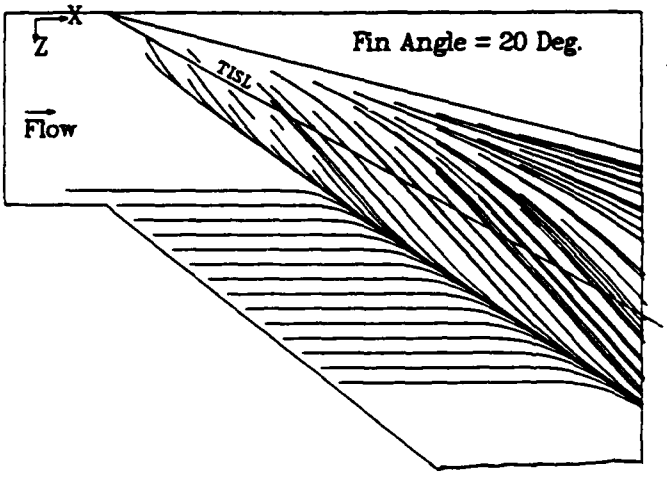

(c) Case C

Figure 13: Surface streamlines (20° SFC)

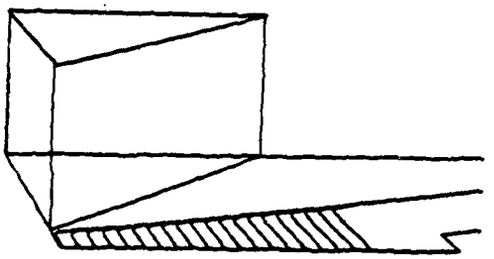

(a) Case A

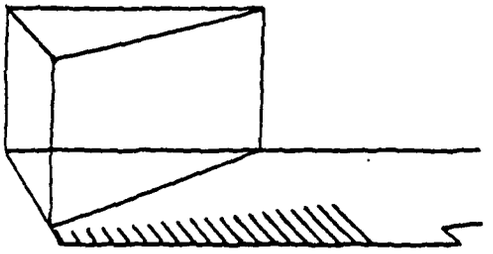

(b) Case B

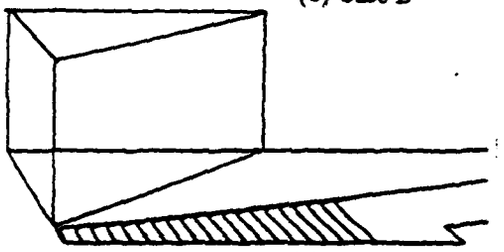

(c) Case C

Figure 14: Particle traces - $y/\delta = 0.0001$ — 20 deg SFC

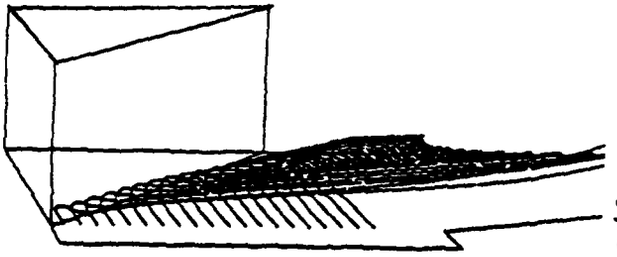

(a) Case A

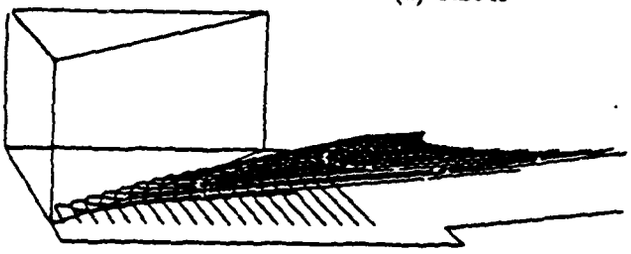

(b) Case B

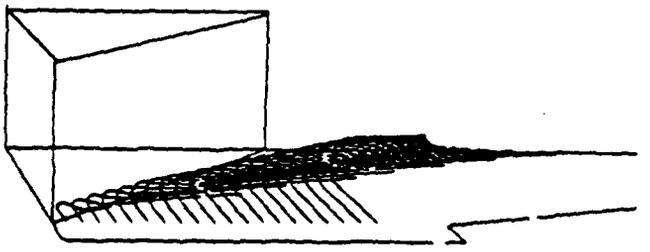

(c) Case C

Figure 15: Particle traces - $y/\delta = 0.6$ — 20 deg SFC

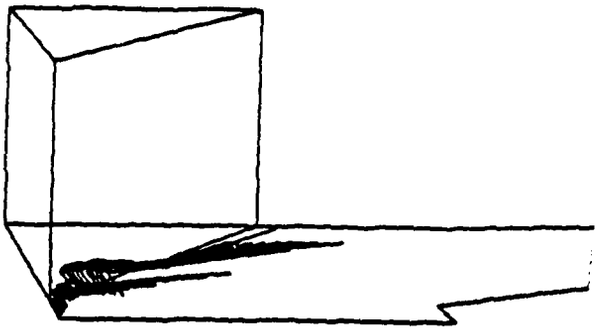

Figure 16: Particle traces in reverse — Case C (20° SFC)

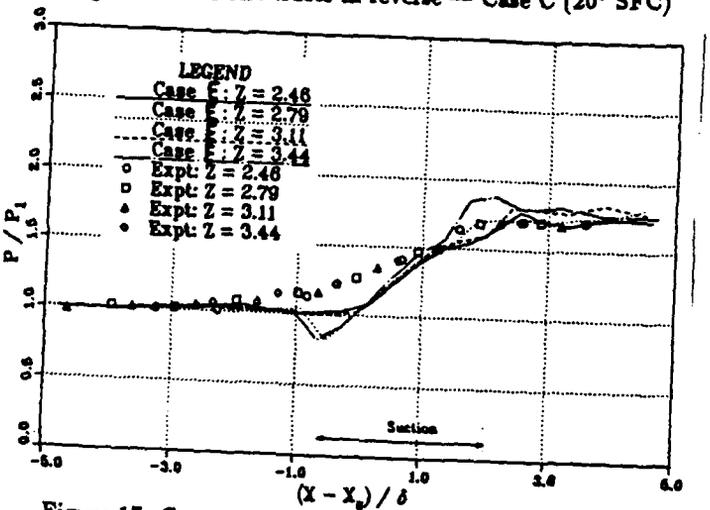

Figure 17: Comparison of surface pressure with experiment — Case E (8° SFC)

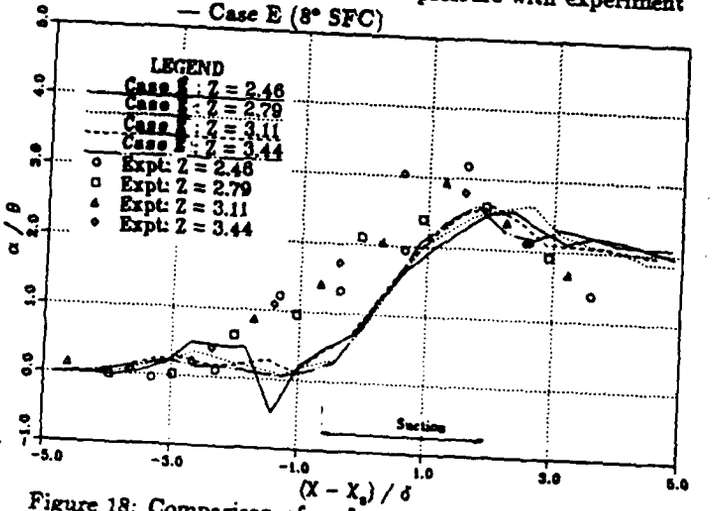

Figure 18: Comparison of surface yaw with experiment — Case E (8° SFC)

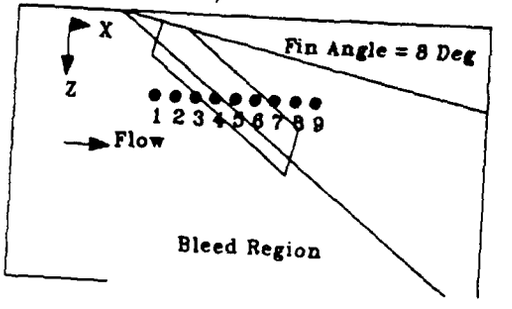

Figure 19: Location of experimental surveys - 8 deg SFC

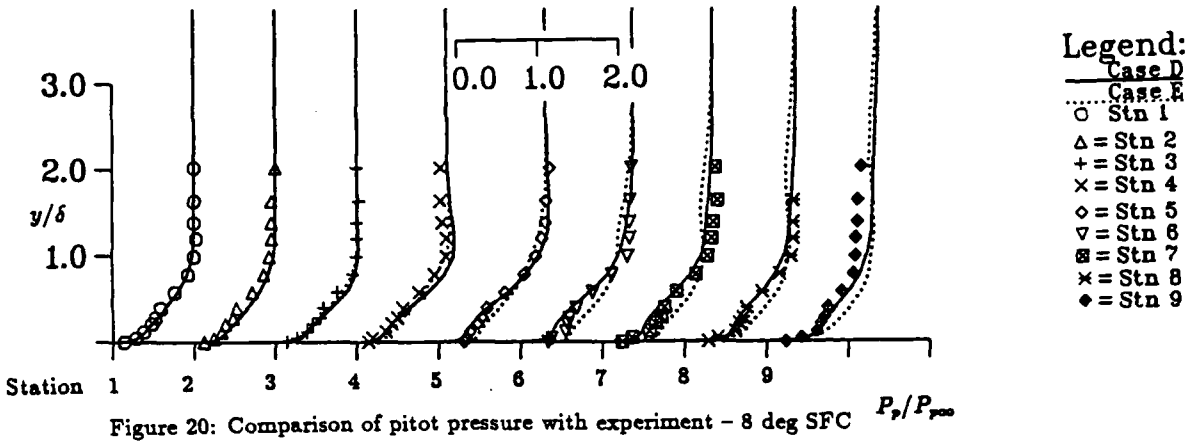

Figure 20: Comparison of pitot pressure with experiment – 8 deg SFC

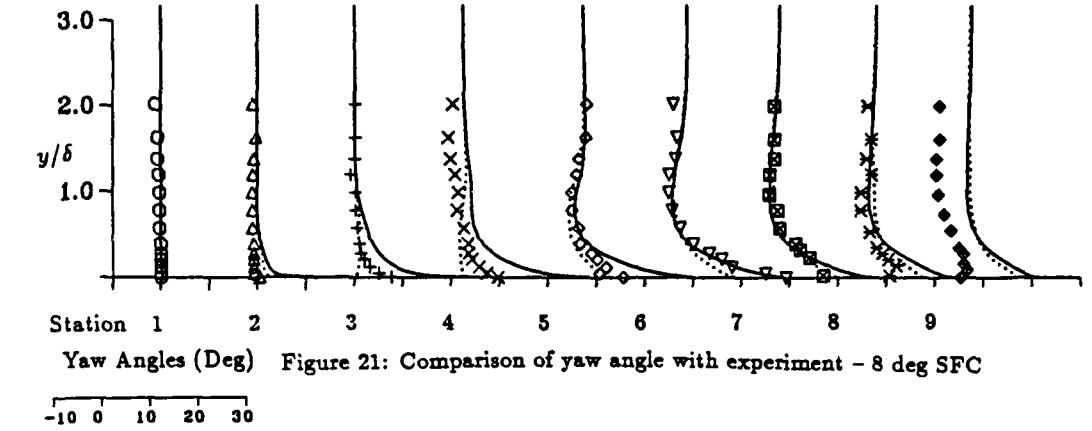

Figure 21: Comparison of yaw angle with experiment – 8 deg SFC

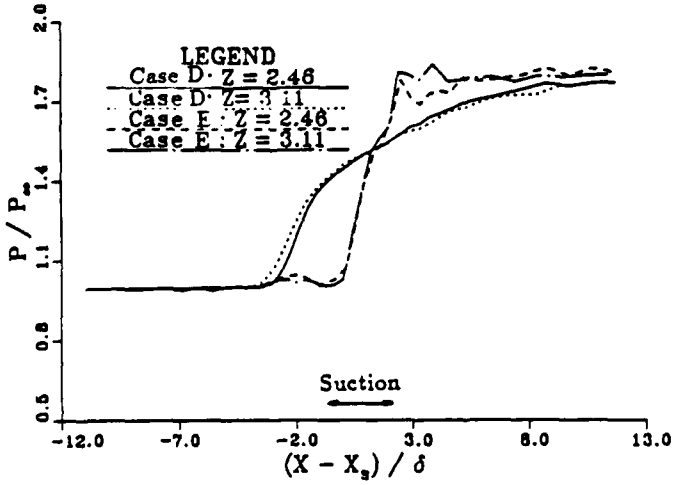

Figure 22: Effect on surface pressure (computed) – 8 deg SFC

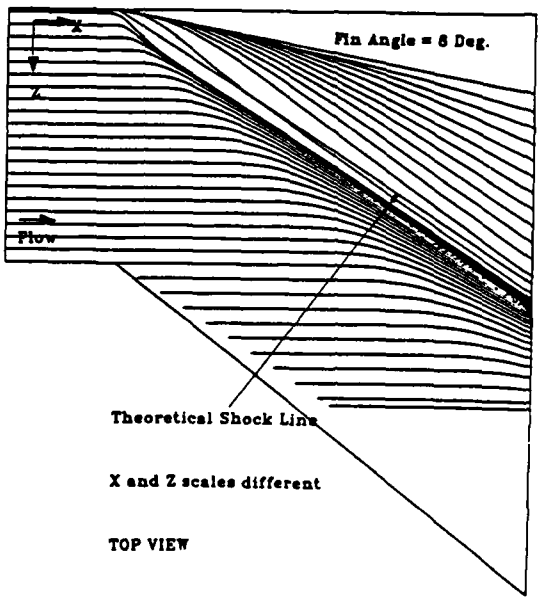

Figure 23: Surface streamlines – Case D (8° SFC)

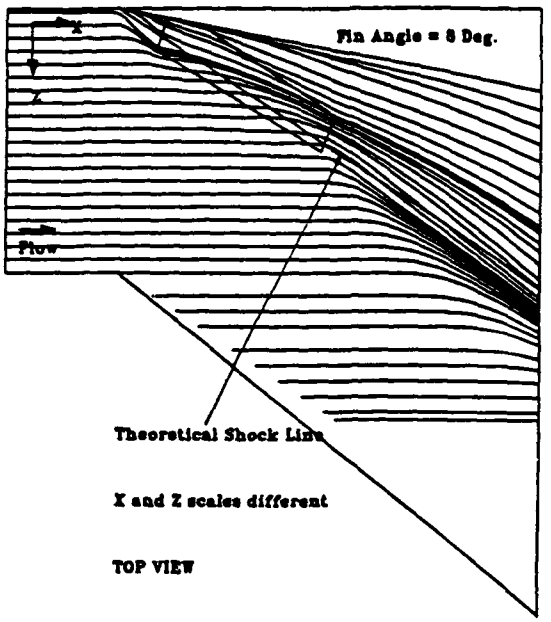

Figure 24: Surface streamlines – Case E (8° SFC)

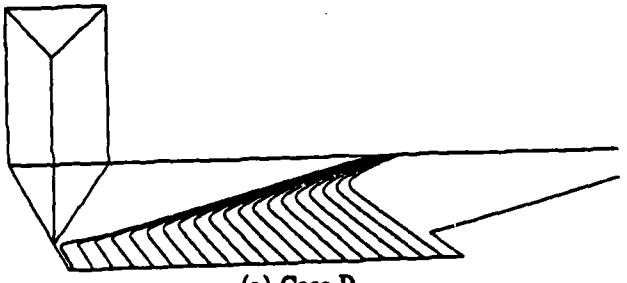

(a) Case D

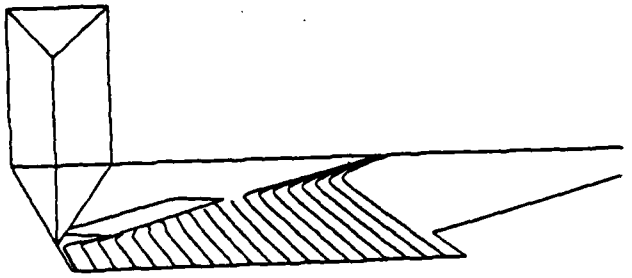

(b) Case E

Figure 25: Particle traces – $y/\delta = 0.0001$ (8° SFC)

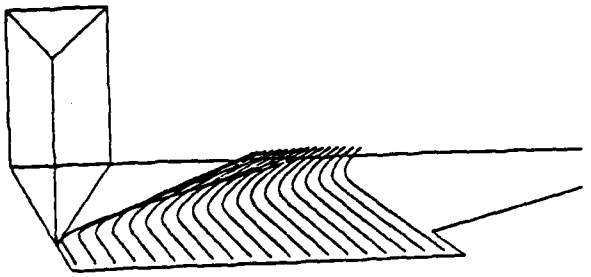

(a) Case D

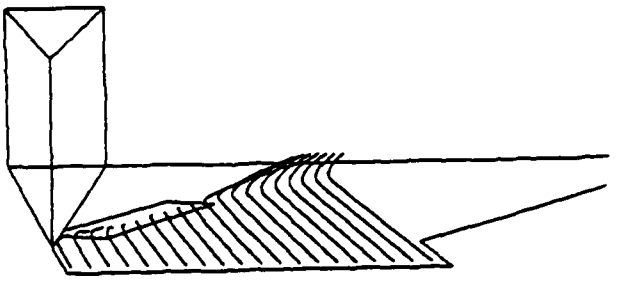

(b) Case E

Figure 26: Particle traces – $y/\delta = 0.1$ (8° SFC)

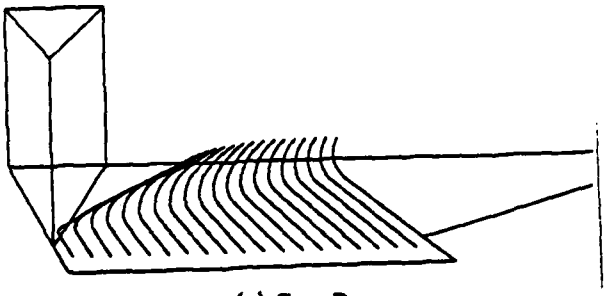

(a) Case D

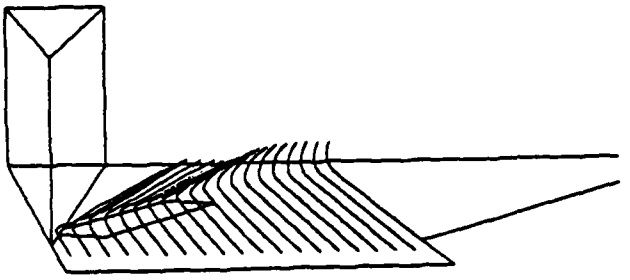

(b) Case E

Figure 27: Particle traces – $y/\delta = 0.3$ (8° SFC)

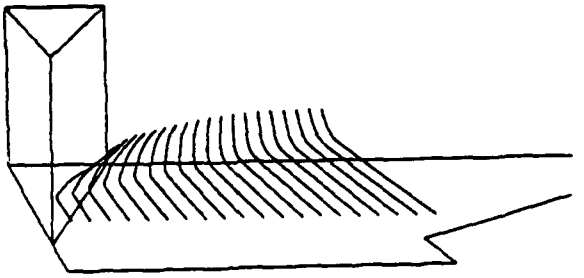

(a) Case D

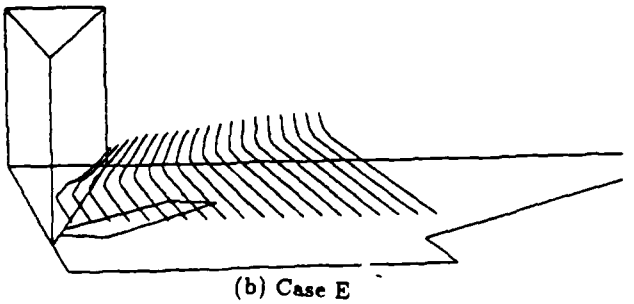

(b) Case E

Figure 28: Particle traces – $y/\delta = 1.0$ (8° SFC)

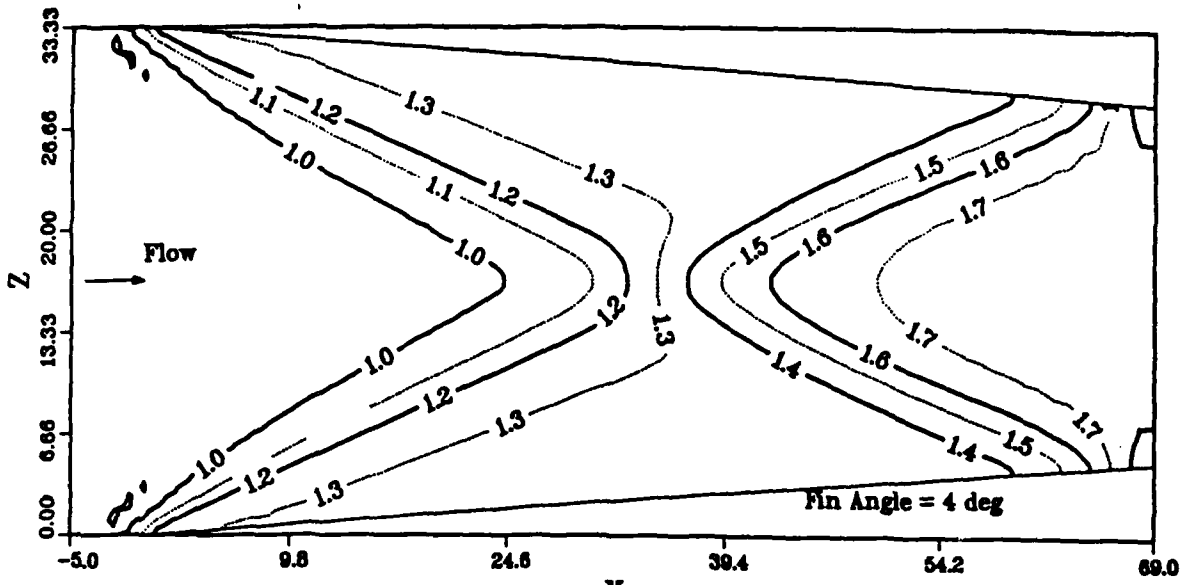

(a) Case F

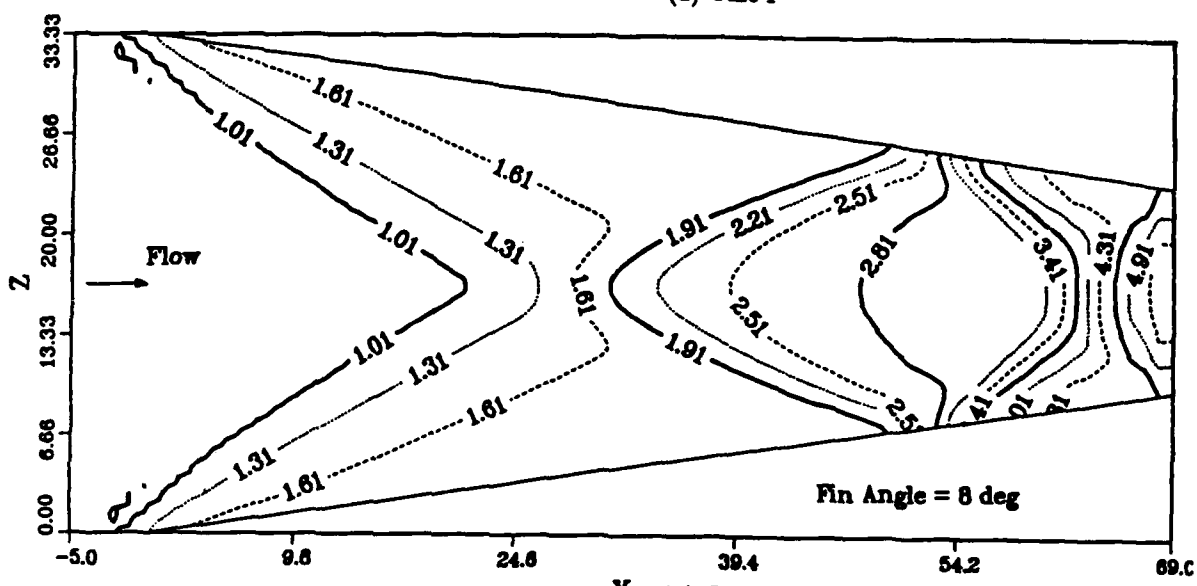

(b) Case G

Figure 29: Surface pressure contours - Cases F and G

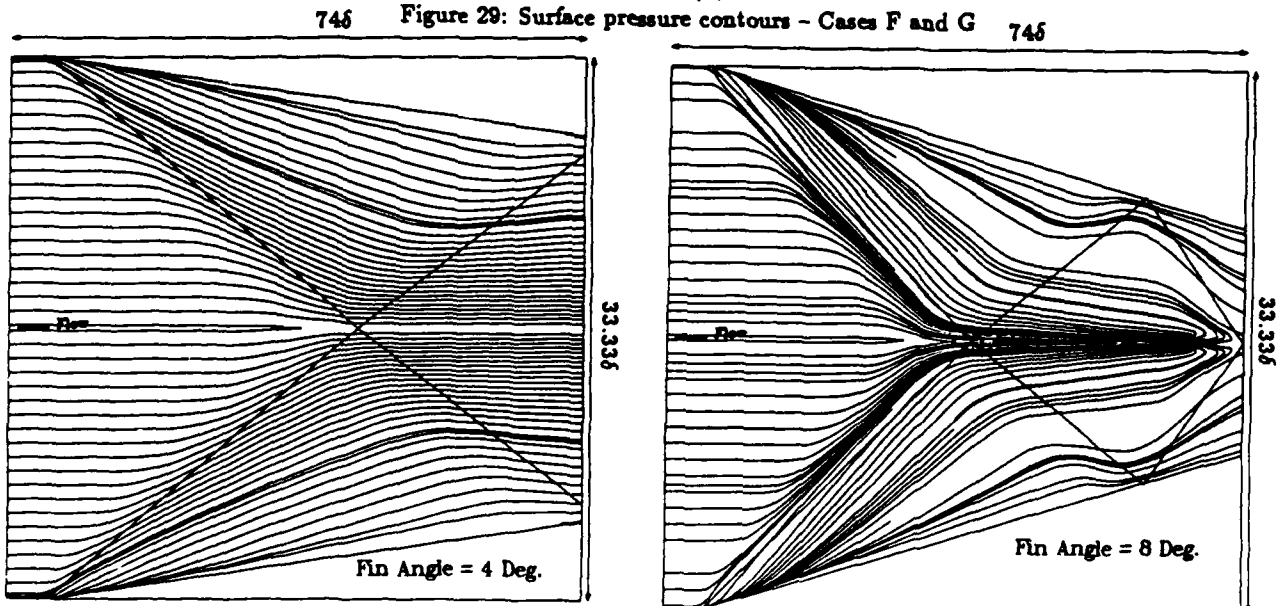

(a) Case F

Figure 30: Surface streamlines - Cases F and G

(b) Case G

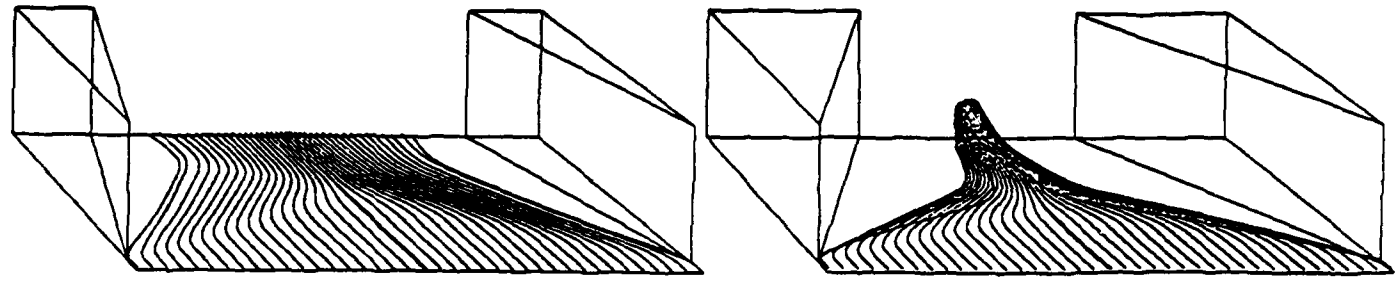

(a) $y/\delta_\infty = 0.1$

$y/\delta = 0.2$

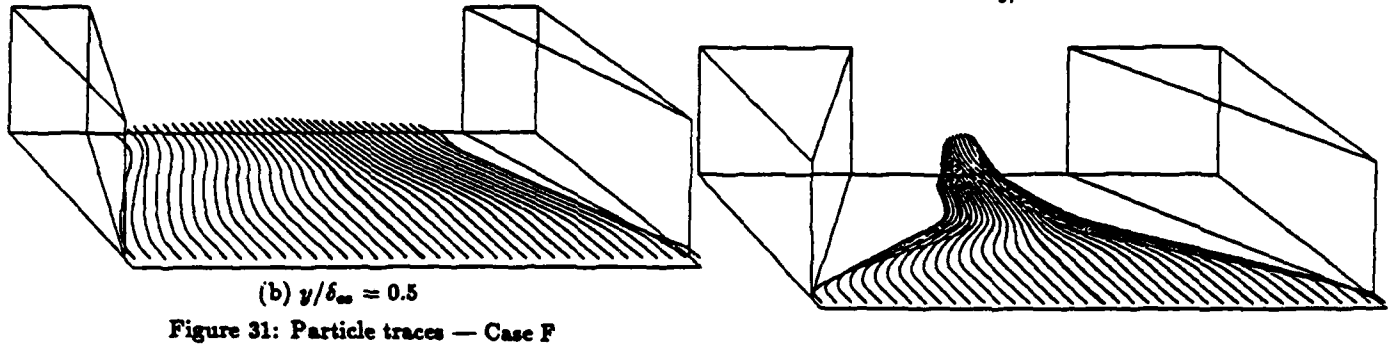

(b) $y/\delta_\infty = 0.5$

Figure 31: Particle traces — Case F

$y/\delta = 0.3$

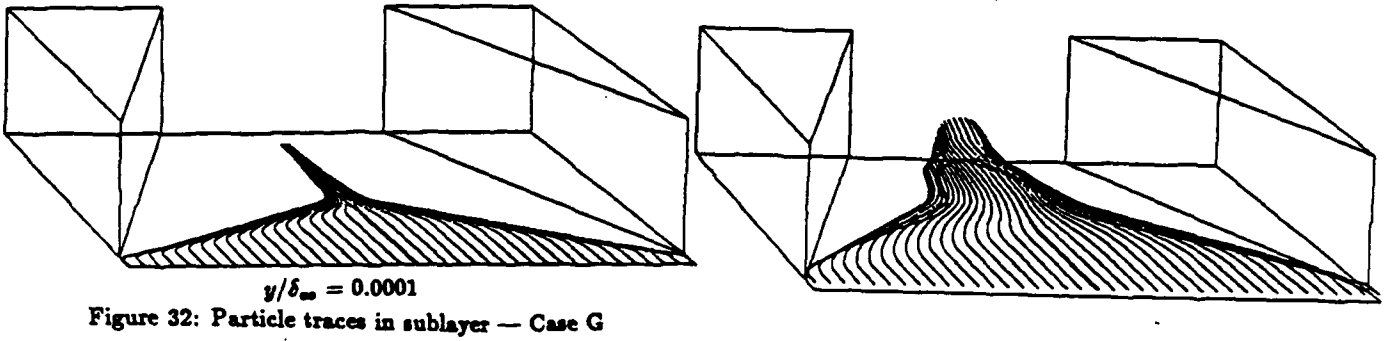

$y/\delta_\infty = 0.0001$

Figure 32: Particle traces in sublayer — Case G

$y/\delta = 0.4$

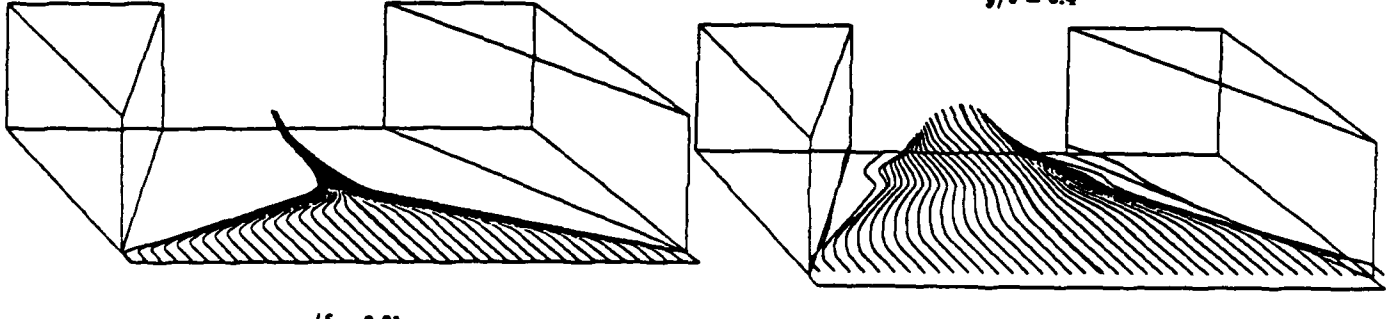

$y/\delta = 0.01$

$y/\delta = 0.8$

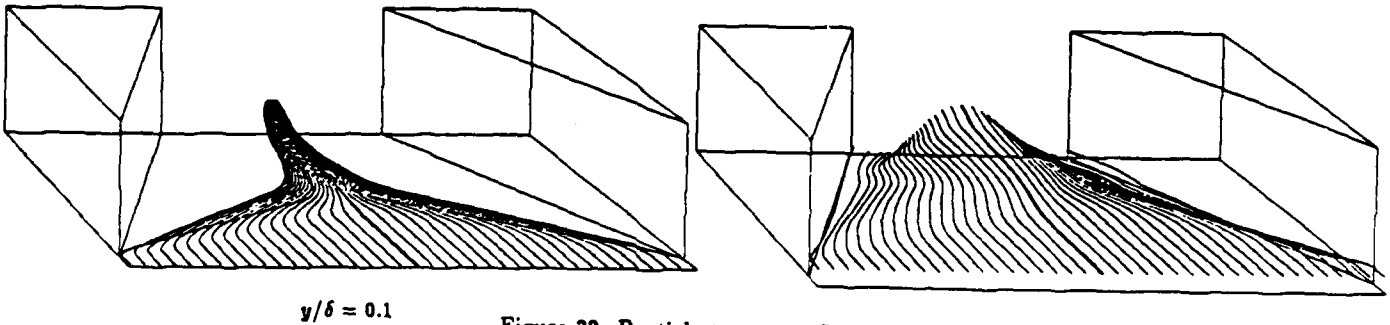

$y/\delta = 0.1$

Figure 33: Particle traces — Case G

$y/\delta = 1.0$

Viscous/Inviscid Effects in 3-D Shock Wave-Turbulent Boundary Layer Interactions

N.Narayanswami† D.D.Knight‡
Department of Mechanical and Aerospace Engineering
Rutgers University, Piscataway, NJ 08855.

Abstract

A detailed analysis of viscous and inviscid effects in 3-D shock wave - turbulent boundary layer interactions has been carried out, focussing on the $(\alpha,\lambda)= (24°,40°)$ swept compression corner configuration at $Re_{\delta_\infty} = 8.1\times10^5$ and the $\alpha = 20°$ sharp fin configuration at $Re_{\delta_\infty} = 9.0\times10^5$. Two flowfields, computed using different turbulence models, are analysed for each configuration. The mean kinetic energy equation is integrated along streamlines originating at various y/δ_∞ locations within and outside the boundary layer and a quantitative comparison is made of the contribution to the mean kinetic energy by inviscid and viscous terms in the equation. Also, the terms are quantitatively compared at points on y - s planes (normal to the streamwise direction) for the sharp fin interaction and at points lying on y - s planes (along the streamwise direction) for the swept compression corner interaction. The results indicate that the interactions for both geometries are governed primarily by inviscid (pressure) effects. Viscous influence, although not of the same magnitude as the inviscid effects, is found to be significant in regions both near and away from the surface of the geometry and not restricted to the 'viscous sublayer' region within the boundary layer.

Introduction

The problem of 3-D shock wave - turbulent boundary layer interactions (3-D turbulent interactions) occurs in a variety of high Mach number flows. Some of the practical applications in which this phenomenon is encountered include high speed aircraft inlets and compressors, wing-body junctures and control surfaces. The complexity of such viscous-inviscid interactions is due to non-linearity, compressibility effects and high gradients of flow variables, besides the difficulty arising from three-dimensionality and turbulence. The interactions are governed in each case by the freestream Mach number M_∞, the Reynolds number Re_{δ_∞} based upon the boundary layer thickness δ_∞, the wall thermal conditions and the geometry generating the interaction.

† Graduate Student, Student Member AIAA
‡ Professor, Associate Member AIAA

Significant progress has been made in the understanding of 3-D turbulent interactions in the past few years. Interactions generated by dimensionless geometries like sharp fins (Fig.1) and swept compression corners (Fig.2) have been studied extensively using experimental techniques, numerical flow simulation and analytical methods.

Recent experimental investigations of 3-D turbulent interactions for simplified geometries like sharp and blunt fins and swept compression corners have been carried out by a number of researchers. Experiments dealing with surface and boundary layer measurements have been conducted by McCabe [1], Law [2], Korkegi [3], Peake [4], Kussoy *et al* [5], Kubota and Stollery [6], Oskam *et al* [7,8], Dolling and Bogdonoff [9,10], McClure and Dolling [11] and Settles *et al* [12,13,14,15,16].

Analytical studies of 3-D interactions have been made by Myring [17], Stalker [18,19], Inger [20,21,22] and by Mee and Stalker [23].

Numerical simulations using the 3-D mean compressible Reynolds averaged Navier - Stokes equations have focussed on similar dimensionless geometries. Swept compression corner and sharp fin generated interactions have been studied by Hung and MacCormack [24,25], Horstman and Hung [27], Horstman [28,29] and Knight [30,31,32,33]. The computations of Knight employ the Baldwin-Lomax algebraic turbulent eddy viscosity model [36] and those of Horstman incorporate the Jones-Launder ($k-\epsilon$) two equation model [37] or Cebici-Smith model [38]. These computations have been validated by comparison with experiments and have been found to be in good agreement with measured values of pitot and static pressure profiles in the boundary layer, surface pressure and yaw angles [34,35].

The interactions are found to be dominated by a large vortical structure (Figs. 5 and 6), in agreement with the flowfield models proposed by Token [40] and and Kubota and Stollery [6]. Besides, the computations of Knight and Horstman, although employing two different turbulence models, show close agreement for both sharp fin and swept compression corner interactions, displaying modest differences only in a small fraction of the boundary layer adjacent to the surface. *The insensitivity of the flowfield to the turbulence models employed in the computations suggests that the flowfield is primarily rotational and inviscid with viscous influence being limited to regions very close to the wall or surface.*

In order to verify this conjecture and to further understand the dynamics of the interactions, the present study aims at making a *quantitative* comparison of inviscid and viscous influence in the flow. Attention has been focussed on the terms in the mean kinetic energy equation (chosen for simplicity and as a first step in this quantitative analysis) and a computer code has been developed to analyse the contributions to the rate of change of mean kinetic energy by both inviscid and viscous terms, along streamlines in the flow. In particular, this code has been used to analyse the 3-D turbulent interactions generated by a swept compression corner and a qualitatively similar interaction generated by a sharp fin geometry. Both geometries chosen are 'dimensionless' and the interactions in the two cases involve similar incoming flow characteristics and pressure rise (shock strengths).

Computation of Flowfields

The flowfields for the sharp fin and swept compression corner interactions analysed in the present study have been computed by Knight [30,31] and Gaitonde [41] and separately by Horstman [28,29]. The mean compressible Navier- Stokes equations coupled with the Baldwin-Lomax algebraic turbulent eddy viscosity model (Knight and Gaitonde) or the Jones-Launder ($k-\varepsilon$) two equation model (Horstman), form the basis of these computations. The code employed by Knight uses an efficient hybrid explicit-implicit algorithm [30] for solution of the governing equations. The implicit algorithm is the Box Scheme of Keller [39], which is applied to the asymptotic form of the Navier-Stokes equations in the very thin 'viscous-sublayer' region of the boundary layer. The flowfield in the region outside the sublayer is computed using the explicit finite-difference algorithm of MacCormack [25,26]. The computations incorporate a body-fitted coordinate transformation to permit the treatment of flow regions of arbitrary shapes and the code has been vectorised for efficient computation on vector processing supercomputers like the CYBER-205 and ETA-10. The code employed by Horstman uses an explicit finite-difference scheme for the computations.

The present study involves the examination of the following flowfields in detail:

1. $(\alpha,\lambda)=(24^\circ,40^\circ)$ Swept corner at $Re_{\delta_\infty}=8.1\times10^6$, $M_{\delta_\infty}=3$ and $\delta_\infty = 0.5$ inch.
(Flowfield No.1: Computed using the Baldwin-Lomax model, and Flowfield No.2: Computed using the Jones-Launder model).

2. $\alpha=20^\circ$ Sharp fin at $Re_{\delta_\infty}=9.0\times10^6$, $M_{\delta_\infty}=3$ and $\delta_\infty =$ 0.5 inch.
(Flowfield No.1: Computed using the Baldwin-Lomax model, and Flowfield No.2: Computed using the Jones-Launder model).

Governing Equation for Mean Kinetic Energy

The mean kinetic energy equation along a streamline may be written as follows:

$$\frac{D}{Dt}\left(\frac{1}{2}\overline{u_i}\overline{u_i}\right) = -\left(\frac{\overline{u_i}}{\rho}\right)\frac{\partial p}{\partial x_i} + \left(\frac{\overline{u_i}}{\rho}\right)\frac{\partial \tau_{ij}}{\partial x_j}$$

Here, $\frac{1}{2}\overline{u_i}\overline{u_i}$ is the mean kinetic energy per unit mass. The D/Dt operator denotes the Particle derivative or the Substantial Derivative. ρ denotes the density of the fluid, p is the pressure and x_i (i=1,2,3) denotes the coordinates x, y and z.
τ_{ij} is the stress tensor (laminar + turbulent) and is given by the relation:

$$\tau_{ij} = -\frac{2}{3}(\mu+\varepsilon)\nabla\cdot\vec{u}\,\delta_{ij} + (\mu+\varepsilon)\left(\frac{\partial u_i}{\partial x_j} + \frac{\partial u_j}{\partial x_i}\right)$$

where,
$\delta_{ij}= 1$ for i=j , and $= 0$ for $i \neq j$
i, j =1,2,3

ε is the algebraic turbulent eddy viscosity given by the turbulence model employed, $\vec{u}$ is the velocity vector and μ is the molecular dynamic viscosity obtained using Sutherland's law.
The equations above are written in the Einstein summation convention.
Integration of the mean kinetic energy equation yields:

$$\frac{1}{2}\overline{u_i}\overline{u_i} = \frac{1}{2}\overline{u_i}\overline{u_i}\,|_{start} + \int -\frac{\overline{u_i}}{\rho}\frac{\partial p}{\partial x_i}\frac{ds}{V} + \int \frac{\overline{u_i}}{\rho}\frac{\partial \tau_{ij}}{\partial x_j}\frac{ds}{V}$$

where,
$\frac{1}{2}\overline{u_i}\overline{u_i}\,|_{start}$ denotes the mean kinetic energy at the starting point of streamline for the fluid particle. 'V' denotes the magnitude of the resultant velocity vector at the location of the fluid particle and 'ds' is the infinitesimal arclength along the streamline.
The rate of change of mean kinetic energy per unit mass is affected by two distinct terms:
The first term $-(\overline{u_i}/\rho)\partial p/\partial x_i$ denotes the inviscid or pressure effect and the second term $(\overline{u_i}/\rho)\partial\tau_{ij}/\partial x_j$ denotes the combined viscous and turbulent stress effect. By following a particle along a streamline and simultaneously integrating the mean kinetic energy equation along the path, the magnitudes of the inviscid contribution and viscous contribution to kinetic energy are quantitatively compared.

It is also useful to consider the following two groups of terms:

1. $\frac{1}{2}\overline{u_i}\overline{u_i}\,|_{start} + \int -\frac{\overline{u_i}}{\rho}\frac{\partial p}{\partial x_i}\frac{ds}{V} + \int \frac{\overline{u_i}}{\rho}\frac{\partial \tau_{ij}}{\partial x_j}\frac{ds}{V}$
2. $\frac{1}{2}\overline{u_i}\overline{u_i}\,|_{start} + \int -\frac{\overline{u_i}}{\rho}\frac{\partial p}{\partial x_i}\frac{ds}{V}$

The first group denotes the *mean kinetic energy obtained by including both the inviscid(pressure) and the viscous integrands* and the second group denotes the *mean kinetic energy obtained by including only the pressure inte-*

grand. The groups 1 and 2 are simultaneously computed along the path of a particle (along the streamline) and compared with each other. A good agreement between the two results indicates that the dynamics along the streamline are governed principally by the *inviscid*(pressure) *effects*, while a significant disagreement between the two indicates that *both pressure and viscous effects* influence the flow along the streamline. Various streamlines (for particles starting at different points in the flow) are investigated in this manner and the results analysed to verify the original conjecture about the principally rotational and inviscid nature of the flowfield.

Computational scheme for the mechanical energy equation

Both the swept compression corner and the sharp fin geometries involve non-uniform grids in the 'physical' domains of the flow. As mentioned earlier, in computing the flowfields, a body-fitted coordinate transformation is used to permit treatment of these non-uniform regions. In a similar manner, the evaluation of the path integral (of the mean kinetic energy equation) involves the transformation of the non-uniform 'physical' grid, denoted by the (x,y,z) coordinate system to a uniform 'computational' grid denoted by the (ξ,η,ζ) coordinate system. The derivative terms in the equation are then approximated by second-order accurate finite-differences. The particle tracing is accomplished by an algorithm developed by *Rauser*[42], which involves location of the particle within a particlar 'cell' of the grid, interpolation of the velocity terms at the particle position and 'movement' of the particle using the interpolated velocities. This particle tracing code has been used to study the flowfield structure of the (α,λ)= (24°,40°) swept compression corner interaction [35]. The mean kinetic energy equation is integrated simultaneously with each movement of the particle. The inviscid(pressure) and viscous (laminar+turbulent) contributions to the rate of change of mean kinetic energy are computed at the particle position in the following steps:

1. Location of the particle in the uniform (computational) grid (using the particle tracing algorithm)
2. Evaluation of the inviscid and viscous terms of the mean kinetic energy equation at the 'cell' corners using finite-differences.
3. Linear interpolation of these values at the particle position and
4. Integration of the inviscid and viscous terms (at the particle position) using simple trapesoidal method.

Results

(α,λ)=(24°,40°) Swept Compression Corner
$Re_{\delta_\infty} = 8.1\times10^6$

The swept compression corner geometry and the computational domain are shown in Figs.2 and 4. The shock generated by the presence of the swept corner interacts with the incoming turbulent boundary layer on the flat plate and causes separation of the flow. The computation of the flowfield incorporates the same incoming flow conditions as the experiments conducted for this configuration at the high Reynolds number wind tunnel at the Princeton Gas Dynamics Laboratory. The experiments involved a Mach number of 3, a total pressure of 690 kPa ± 1.3%, a total temperature of 265.4 deg K ± 1.6% , near adiabatic surface temperature and an incoming 2-D turbulent boundary layer which has been studied and observed to satisfy the Law of the Wall and Wake [43]. The molecular and turbulent Prandtl numbers are 0.73 and 0.9, respectively. The incoming turbulent bounday layer is a 'thick' layer of a height δ_∞ = 0.5 inch. Here, δ_∞ refers to the height of the boundary layer at the corner line (where the compression ramp meets the flat plate), in the absence of the ramp.

Flowfield No.1: *Baldwin-Lomax Turbulence Model*

In order to study individual particles in the flow, streamlines were traced by releasing particles at fixed y/δ_∞ locations near the upstream end of the flowfield. 10 particles were released at every y/δ_∞ location, spaced evenly in the *z-direction*, between the minimum and maximum z values of the grid at that location. Particle traces for $y=0.02\delta_\infty$, $0.05\delta_\infty$, $0.2\delta_\infty$ and $0.5\delta_\infty$ are shown in Fig.7. The particles released at $y=0.02\delta_\infty$ and $y=0.05\delta_\infty$ are observed to get entrained into the vortical structure at the base of the compression corner and those starting at $y= 0.2\delta_\infty$ and $y=0.5\delta_\infty$ continue over the vortex and up the compression ramp.

The streamlines may be numbered 1 through 10, starting from the one nearest to the symmetry boundary of the *domain*. The *fifth* streamline among these is chosen as a 'typical' streamline for study, for each of the four y/δ_∞ (starting) locations. In Figs. 8-11, the kinetic energy evaluated by interpolating the velocities from the computed flowfield and that obtained by computing the path integral (right hand side of the integrated mean kinetic energy equation) are shown for each y/δ_∞ (starting) case. The results for the $y= 0.02\delta_\infty$,$y=0.05\delta_\infty$ and $y=0.5\delta_\infty$ cases have been presented in an earlier paper [35], but are described again here for comparison with the results for the flowfield obtained using the different turbulence model (Flowfield No.2). The kinetic energy profiles are in close agreement, and the differences in the two results is attributable to the truncation errors involved in the schemes employed in computing both the path integral as well as the flowfield itself. For the streamlines originating at $y=0.2\delta_\infty$ and $y=0.5\delta_\infty$, however, the difference in the two values of kinetic energy is approximately 15% in each

case. The reason for this error is being investigated. The kinetic energy, in each of the cases, remains unaffected till the start of the interaction, when the adverse pressure gradient encountered in the region of the shock coupled with viscous influence causes a sharp decline in the energy of the particle. The drop in energy stops at the end of the interaction, after which it reaches a near asymptotic value.

For the same streamlines discussed above, the mean kinetic energy obtained by including both the pressure and the viscous integrands is compared to that obtained by the path integral involving only the pressure integrand. (i.e) the term

$\frac{1}{2}u_i u_i|_{start} + \int -(u_i/\rho)\partial p/\partial x_i(\frac{dx}{V}) + \int (u_i/\rho)\partial \tau_{ij}/\partial x_j(\frac{dx}{V})$

is compared to the term $\frac{1}{2}u_i u_i|_{start} + \int -(u_i/\rho)\partial p/\partial x_i(\frac{dx}{V})$

The first term is referred to as *K.E -Path Integral*, in the plots and the second term, as *K.E -Path Integral, Inviscid Integrand*. For the $y=0.02\delta_\infty$ case, the two values differ considerably, indicating that *both inviscid and viscous effects are significant for these streamlines*. Similar results are observed for the other nine streamlines originating at $y=0.02\delta_\infty$. For the $y=0.05\delta_\infty$ case, the two values are reasonably close and it can be inferred that *the pressure (inviscid) influence is dominant* for the streamline. Similar results are again observed for the other streamlines originating from the same y- location. It is to be noted here, that in both the $y=0.02\delta_\infty$ and $y=0.05\delta_\infty$ cases, the particles get trapped deep within the vortical structure. Yet, viscous influence is more significant for the former than the latter case. The plots for the $y=0.2\delta_\infty$ and $y=0.5\delta_\infty$ streamlines show an increasing dominance of the inviscid effect on the mean kinetic energy. As remarked before, these particles do not get trapped within the vortical structure of the interaction, but continue over it and along the ramp. The remaining nine streamlines in each case exhibit similar behavior as the 'typical' streamline examined for the two cases.

The relative importance of the viscous effect for the streamlines originating at $y=0.02\delta_\infty$ and $y=0.05\delta_\infty$ is also evident from the profile of the kinetic energy obtained using only the viscous integrand (refered to as *K.E -Path Integral, Viscous Integrand*) in the plots.

Flowfield No.2: *Jones-Launder Turbulence Model*

A similar analysis is carried out for this flowfield and the mean kinetic energy evaluated for streamlines originating at $y=0.02\delta_\infty$, $0.05\delta_\infty$, $0.2\delta_\infty$ and $0.5\delta_\infty$. Again, the fifth streamline from the symmetry boundary of the domain is chosen as the 'typical' streamline for study. Figs.12 and 15 show the streamlines for the particles originating at the four different y -locations. The streamlines are similar to that obtained for the different cases for Flowfield No.1. Figs.13-14 and 16-17 show a comparison between the kinetic energy obtained by a) interpolating the flowfield, b) by the path integral, c) by the path integral obtained with only the inviscid integrand and d) by the path integral obtained with only the viscous integrand. The kinetic energy values obtained by flowfield interpolation and by the total path integral, although close, differ by about 10-15% on average. This error may be attributed to the coarseness of the grid and the resulting truncation errors in the computation of both the flowfield and the path integral. Consequently, no definite conclusion can be reached about the nature of the flow from these results. It can however be noted that the path integral obtained using the inviscid term alone approximates reasonably well, the total path integral in each of the four cases. Also, the viscous influence is particularly significant for the streamline originating at $y = 0.2\delta_\infty$.

20° Sharp fin: $Re_{\delta_\infty} = 9.0\times10^6$

The sharp fin geometry and the computational domain, are shown in Figs. 1 and 3. Here again, the generated shock wave interacts with a 'thick' incoming boundary layer on the flat plate (δ_∞= 0.5 inch), where δ_∞ is the height of the boundary layer at the location of the apex of the fin, in the absence of the fin.

The computations of the flowfield incorporate the inflow conditions for the experiments on the 20° sharp fin case at the Princeton Gas Dynamics Laboratory. The experiments involve nominal freestream Mach number of 2.93, a total pressure of 680 kPa ± 1% , a total temperature of 251 deg K ± 5%, near adiabatic wall conditions and a 2-D 'thick' incoming equilibrium boundary layer which has been thoroughly investigated and observed to fit the Law of Wall and Wake.

Flowfield No.1: *Baldwin-Lomax Turbulence model*

An analysis similar to that for the swept compression corner case is carried out for this interaction. 10 particles spaced evenly between the minimum and maximum 's' values of the domain upstream of the leading edge of the fin are released at different y/δ_∞ locations near the upstream boundary. Again, the *'fifth'* streamline is chosen for study for each of the y-levels. The streamlines for particles released at $y=0.02\delta_\infty$,$y=0.05\delta_\infty$, $y=0.2\delta_\infty$ and $y=0.5\delta_\infty$ are shown in Fig.18. In all the four cases, the streamlines are observed to get wrapped up into the vortical structure emanating from near the leading edge of the fin. Figs.19-22 show the comparison between a) the mean kinetic energy obtained by interpolation of the computed flowfield b) the path integral for the streamline c) the path integral involving only ine inviscid term and d) the path integral involving only the viscous term, for each case. The interpolated and integrated values of kinetic energy agree quite closely in the four cases, and differences in the two values are attributable to the truncation errors in the numerical schemes. The $y=0.02\delta_\infty$ case shows a drop in the kinetic energy at the start of the interaction but a subsequent rise in the energy to a level above the value at the upstream (starting) position of the particle. i.e., the particle is 'accelerated' by the influence of the inviscid/viscous terms. The $y=0.05\delta_\infty$ exhibits a similar behavior of acceleration of the particle along the streamline. For the $y=0.2\delta_\infty$ and $y=0.5\delta_\infty$ cases, the mean kinetic energy drops at the start of the interaction and reaches a

near asymptotic value thereafter.

It is also observed that the results obtained by computing the full path integral (b) and the path integral involving only the inviscid integrand (c) differ significantly for the streamlines starting at $y=0.02\delta_\infty$ and $y=0.05\delta_\infty$. Also, similar behavior is exhibited by the other nine streamlines in the two cases. It can therefore be concluded that *both inviscid and viscous effects are significant* for these streamlines.

For the $y=0.2\delta_\infty$ and $y=0.5\delta_\infty$ cases, the path integral involving the pressure term alone, is a reasonable approximation to the mean kinetic energy of the particle, indicating that *the flow along these streamlines is governed principally by inviscid (pressure) effects.* Similar results are obtained for the other nine streamlines originating at these two y/δ_∞ locations.

Figs.23 and 24 show the magnitudes of the inviscid (pressure) contribution to mean kinetic energy (i.e), $\int -(u_i/\rho)\partial p/\partial x_i(\frac{dx}{dt})$ and the viscous contribution to mean kinetic energy (i.e), $\int (u_i/\rho)\partial \tau_{ij}/\partial x_j(\frac{dx}{dt})$ for the 'fifth' streamlines starting at the levels $y=0.02\delta_\infty$ and $y=0.05\delta_\infty$. The height of the particles (from the surface of the flat plate) are also shown as a function of arclength. The inviscid and viscous terms have been normalised by the value of the mean kinetic energy at the upstream (starting) locations of the particles. It is observed that viscous influence continues to remain significant even as the particle moves away from the wall, contrary to the original hypothesis that a 'decrease' in the viscous effect should be observed as the distance of the particle from the wall increases. *This indicates that there exist regions in the flow, apart from regions adjacent to the plate surface, where the interaction is significantly viscous in nature.*

Flowfield No.2: *Jones-Launder Model*

Fig.25 shows the streamlines for particles released at $y= 0.02\delta_\infty$, $0.05\delta_\infty$ $0.2\delta_\infty$ and $0.5\delta_\infty$. The streamlines are similar to that obtained for the corresponding cases for Flowfield No.1. As before, the 'fifth' streamline from the symmetry boundary is chosen for study in each case. Fig.26-27 show the kinetic energy computed by: a) interpolating the velocities from the known flowfield values, 2) the path integral, 3) the path integral involving only the inviscid integrand and d) the path integral involving only the viscous integrand, for the *fifth* streamline originating at $y=0.2\delta_\infty$ and $0.5\delta_\infty$. The kinetic energy values obtained by interpolation and by the path integral are reasonable close. The kinetic energy profile obtained by employing the the inviscid term alone provides a good approximation to the value obtained by the full path integral in both cases. The other nine streamlines in each case exhibit similar behavior and it can thus be concluded that the dynamics of the interaction along these streamlines are governed primarily by *inviscid(pressure) effects.* The computations for the $y= 0.02\delta_\infty$ and $0.05\delta_\infty$ cases did not yield a good agreement between the interpolated and path integral values owing to large truncation errors in the numerical schemes and the results for these streamlines are hence not presented here.

Planewise examination of inviscid and viscous influence in the flow

Case 1: 20° Sharp Fin Interaction

In order to identify regions of inviscid and viscous influence in the flow, the pressure term $-(u_i/\rho)\partial p/\partial x_i$ and the viscous term $(u_i/\rho)\partial \tau_{ij}/\partial x_j$ are computed at mesh points on $y-z$ planes at different 'x/δ_∞' locations in the flow.

The following analysis refers to the flowfield generated using the Baldwin-Lomax algebraic turbulent eddy viscosity model (Flowfield No.1). Fig.28 shows the magnitude of the pressure and viscous terms in the form of contour plots on the $y-z$ plane at the location $x= 15\delta_\infty$, downstream of the leading edge of the fin. The minimum z/δ_∞ value of 0.0 corresponds to a point $0.01\delta_\infty$ away from the surface of the fin in the z-direction. The minimum y/δ_∞ value of 0.0 also corresponds to a point $0.01\delta_\infty$ above the surface of the plate. The maximum value of y is $2.0\delta_\infty$. The y and z values are denoted as multiples of δ_∞. Both pressure and viscous term values, $-(u_i/\rho)\partial p/\partial x_i$ and $(u_i/\rho)\partial \tau_{ij}/\partial x_j$ are normalised by the maximum(absolute) value of inviscid/viscous contribution terms on the particular $y-z$ plane. Also as observed from the plot of 'pressure contours' at the same location, the pressure rise due to the shock is distributed within the boundary layer and forms a 'λ' shaped region.

A comparison of the contour plots of the inviscid and viscous contributions (A and B) and pressure (C) shows that the inviscid influence is concentrated only towards the freestream side of the 'λ' shaped shock structure, although the pressure rise continues upto the fin surface. *The region of viscous influence is significantly large* as is evident from plot B and lies to the left of the region of maximum inviscid influence. The reason for the concentration of inviscid influence towards the freestream side of the 'shock' region, becomes evident when the inviscid (pressure) term $-(u_i/\rho)\partial p/\partial x_i$ is examined more closely. Since the term involves both the directions and magnitudes of velocity and the pressure gradient, the two may be combining in a way so as to result in an almost '*zero*' inviscid effect in the area between the observed region of concentrated inviscid influence and the fin surface. Plot D shows the direction of the velocity vectors on the plane as observed from the apex of the fin. The resultant velocities at the points on this plane are obtained from the velocity components tangential to a ray drawn from the apex to each grid point on the plane.

The orientation of the velocity vectors clearly indicates the presence of the vortical structure and the rotational nature of the flow. In the region between a ficticious 'center' of the vortical structure and the fin surface, the flow is observed to be going 'down', towards the plate. It is to be noted that at each mesh point on the y-z plane, a component of velocity along the ray drawn from the apex of the fin to the grid point, exists, but is not represented in the

diagram. It is conjectured that the term $-(u_i/\rho)\partial p/\partial z_i$ becomes nearly zero in this region due the fact that the directions of the velocity components are normal to that of the corresponding pressure gradients in this region. Similar results are obtained for the other $y-z$ planes analysed at other z/δ_∞ locations in the flow. The region of viscous influence is significant in each of the other cases, as observed earlier for the $x= 15\delta_\infty$ plane and always lies to the immediate left of the region of concentrated inviscid influence in the flow.

The maximum absolute value of the viscous term is approximately 40% of the maximum absolute value of the inviscid effect for points on the $x= 15\delta_\infty$ plane. Besides, the region of viscous influence extends upto a height of $2.0\delta_\infty$ above the surface of the plate.

The analysis for Flowfield No.2 was carried out in a manner similar to that for Flowfield No.1. (results not shown here). It was observed that although the location of the region of inviscid influence was found to agree closely with that for Flowfield No.1, the viscous influence remained concentrated only in the regions very close to the plate or fin surface (typically upto $0.05\delta_\infty$)and did not affect the flow higher up in the boundary layer. Again, this result may be a consequence of inadequate grid resolution for this flowfield and consequently, no firm conclusions can be drawn regarding the viscous influence in the flow from the analysis of Flowfield No.2.

Case 2: $(\alpha,\lambda)=(24°,40°)$ Swept Compression Corner Interaction

As observed from Fig.7, the 'vortical structure' in this interaction is aligned approximately with the base of the compression ramp. In order to study the interaction and the nature of the vortical structure in a manner similar to that of the sharp fin case, the pressure and viscous terms in the mean kinetic energy equation were compared quantitatively for points lying on '$y-z$' planes in the flow. Here, 'y' may be considered to be the height of a point above the surface of the plate/ramp.

Flowfield No.1.

Fig.29 shows the contours for the inviscid term (A), the viscous term (B) and the pressure (C) and velocity vector (D) plots for the '$y-z$' planes at $z\approx4.6\delta_\infty$ and $z\approx7.0delta_\infty$. These planes represent two 'typical' cross-sections of the flow, sufficiently far from the origin of the vortical structure aligned approximately with the corner. The pressure contours show the distribution of the pressure rise due to the shock over a finite area as the shock interacts with the incoming turbulent boundary layer on the flat plate, thus forming a 'λ' shaped region of pressure rise, similar to that observed for the case of the sharp fin interaction. The region of maximum inviscid influence (see contours of 'inviscid term') is concentrated towards the upstream side of the 'λ' shock structure. As in the case of the sharp fin interaction, the 'zero' inviscid influence to the left of this region maybe due to the orientation of the velocity components and the corresponding pressure gradients (in the 'inviscid' term) in this region. Also, a significantly viscous region lies between the region of maximum inviscid influence and the compression ramp surface. This structure is in very close agreement with that observed for the sharp fin configuration. The 'polar velocity vector' plot represents the resultant velocities of the components normal to a ray drawn from the origin (at the base of the corner and at the $z=0$ boundary of the domain). The directions of the velocity vectors shows quite clearly, the vortical structure at the base of the corner.

Flowfield No.2.

Fig.30 shows the contours for the inviscid and viscous terms (A, B) and pressure (C) along with the 'polar velocity plot' (D) for the '$y-z$' planes at $z\approx4.7\delta_\infty$ and $z\approx7.0\delta_\infty$. The region of inviscid influence again lies, to a large extent, towards the upstream side of the 'λ' shaped region of pressure rise. The region of viscous influence can be observed to lie along the streamwise direction at a certain distance from the surface of the plate or the compression corner. The region of maximum viscous influence lies far downstream of the region of concentrated inviscid influence in the flow. Again, however, it is possible that the inadequate grid resolution has introduced significant errors in the computation of the gradients of the viscous stresses for points lying on these planes. Hence, no firm conclusions can be drawn from the analysis of this flowfield with regard to regions of viscous influence in the interaction.

Conclusions

The detailed investigation of the viscous and inviscid influence in the 3-D turbulent interactions generated by the sharp fin and swept corner configurations yields the following results:

1. The dynamics of the interactions are observed to be governed primarily by inviscid (pressure) effects.
2. Viscous influence is significant in the interactions, as observed from the examination of the flowfields generated by the Navier-Stokes code incorporating the Baldwin-Lomax algebraic turbulent eddy viscosity model. In the case of the sharp fin, this region extends upto approximately $2.0\delta_\infty$ above the plate surface.
3. The region of maximum inviscid influence in the interactions is concentrated towards the freestream side of the λ shaped region of pressure rise for the sharp fin interaction and towards the upstream side for the swept compression corner case. This is observed to be consistent for both flowfields (generated using different turbulence models) in each case.

4. The region of maximum viscous influence lies between the region of maximum inviscid influence and the geometry generating the interaction for the flowfields computed using the Baldwin-Lomax model.
5. No firm conclusions can be drawn regarding region of viscous influence in the interactions, by the analysis of the flowfields generated using the Jones-Launder turbulence model, due to inadequate grid resolution for computation of the viscous stress gradient terms.

The present study gives an indication of the complex nature of the 3-D shock wave- turbulent boundary layer interaction generated by even simple dimensionless geometries. It would be interesting to examine the flowfields with regard to vorticity and total energy along streamlines in the flow. It would be also worthwhile to compare the results obtained for the sharp fin and swept corner interaction to other three dimensional interactions.

Acknowledgements

This research was sponsored by the Air Force Office of Scientific Research under AF Grant No. 86-0266 monitored by Dr. James McMichael and Dr. Len Sakell. The authors would like to thank Dr.C.C Horstman of the NASA Ames Research Center for many helpful discussions and for the flowfield data on the sharp fin and swept corner interactions for this study. Help from the Supercomputer Remote Access Facility staff at Rutgers University, is also gratefully acknowledged.

References

[1] McCabe, A., The Three-Dimensional Interaction of a Shock Wave with a Turbulent Boundary Layer. *The Aeronautical Quarterly* Vol 17, pp. 231-252, 1966.

[2] Law, C., Three Dimensional Shock Wave/Turbulent Boundary Layer Interactions at Mach 6. *Technical Report TR-75-0191, ARL*, 1975.

[3] Korkegi, R. H., On the Structure of Three-Dimensional Shock-Induced Separated Flow Regions. *AIAA Journal* Vol 14, No.5, May 1976.

[4] Peake, D., Three Dimensional Swept Shock Turbulent Boundary Layer Separations with Control by Air Injection. *Technical Report Aero. Report No. LR-592, National Research Council - Canada*, 1976.

[5] Kussoy, M. I., Viegas, J. R and Horstman, C. C., Investigation of a Three-Dimensional Shock Wave Separated Boundary Layer. *AIAA Journal* Vol 18, December 1980, pp. 1477-1484.

[6] Kubota, H. and Stollery, J. L., An Experimental Study of the Interaction Between a Glancing Shock Wave and a Turbulent Boundary Layer. *Jl. of Fluid Mech.* Vol 116, 1982, pp. 431-458.

[7] Oskam, B., Vas, I and Bogdonoff, S., Mach 3 Oblique Shock Wave / Turbulent Boundary Layer Interaction in Three Dimensions. *AIAA Paper No. 76-336*, 1976.

[8] Oskam, B., Vas, I. and Bogdonoff, S., An Experimental Study of three-Dimensional Flowfields in an Axial Corner at Mach 3. *AIAA paper No. 77-689*, 1977.

[9] Dolling, D. S. and Bogdonoff, S. M., Blunt Fin Induced Shock Wave / Turbulent Boundary Layer Interactions. *AIAA Journal*, Vol 20, No.12, December 1982, pp. 1674-1680.

[10] Dolling, D. S. and Bogdonoff, S. M., Upstream Influence in Sharp Fin-Induced Shock Wave Turbulent Boundary Layer Interaction. *AIAA Journal*, Vol 21, No.1, Jan 1983, pp. 143-145.

[11] McClure, W. and Dolling, D., Flowfield Scaling in Sharp Fin Induced Shock Wave Turbulent Boundary Layer Interaction. *AIAA Paper 83-1754*, 1983.

[12] Settles, G. S.,Vas, I. E and Bogdonoff, S. M., Details of a Shock Separated Turbulent Boundary Layer at a Compression Corner. *AIAA Journal* Vol 14, Dec 1976, pp. 1709-1715.

[13] Settles, G. S, Fitzpatrick, T. J and Bogdonoff, S. M., Detailed study of attached and Separated Compression Corner Flowfields in High Reynolds Number Supersonic Flow. *AIAA Journal*, Vol 17, June 1979, pp. 579-585.

[14] Settles, G. S., Perkins, J. J. and Bogdonoff, S. M., Investigation of Three Dimensional Shock/Boundary Layer Interactions at Swept Compression Corners. *AIAA Journal*, Vol 18, July 1980, pp.779-785.

[15] Settles, G. S and Bogdonoff, S. M., Scaling of Two and Three Dimensional Shock/Turbulent Boundary Layer Interactions at Compression Corners. *AIAA Journal*, Vol 20, June 1982, pp. 782-789.

[16] Settles, G. S and Teng, H. Y., Flow Visualization Methods for Separated Three Dimensional Shock Wave - Turbulent Boundary Layer Interactions. *AIAA Journal* Vol 21, March 1983, pp. 390-397.

[17] Myring, D. F., The Effect of Sweep on Conditions of Separation in Turbulent Boundary -Layer/Shock Wave Interaction. *The Aeronautical Quarterly*, May 1977, pp. 111-122.

[18] Stalker, R., Spanwise Propagation of Disturbances in Swept Shock Wave- boundary Layer Interactions. *AIAA Paper No. 82-0988*, 1982.

[19] Stalker, R., A Characteristics Approach to Swept Shock - Wave/Boundary Layer Interactions *AIAA Journal*, Vol 22, No.11, November 1984.

[20] Inger, G. R., Analytical Investigation of Swept Shock - Turbulent Boundary layer Interaction in Supersonic Flow. *AIAA Paper No. 84-1555*, June 1984.

[21] Inger, G. R., Supersonic Viscous-Inviscid Interaction of a Swept Ramp with a Turbulent Boundary Layer. *AIAA Paper No. 85-1669*, July 1985.

[22] Inger, G. R., Incipient Separation and Similitude Properties of Swept Shock/Turbulent Boundary Layer Interactions. *AIAA Paper No. 88-0388*, 1988.

[23] Mee, D. and Stalker, R., Investigation of Weak Shock-Shock and Shock Expansion Intersection in the Presence of a Turbulent Boundary Layer. *AIAA Paper No. 87-0549*, 1987.

[24] Hung, C. M. and MacCormack, R. W., Numerical Solution of Three-Dimensional Shock Wave and Turbulent Boundary Layer Interaction. *AIAA Journal* Vol 16, October 1978.

[25] MacCormack, R. W., Numerical Solution of the Interaction of a Shock Wave with a Laminar Boundary Layer. *Lecture Notes in Physics*, Vol 8, 1971, pp. 151-163.

[26] Baldwin, B. S.,and MacCormack, R. W., A Numerical Method for Solving the Navier-Stokes Equations with Application to Shock - Boundary Layer Interactions. *AIAA Paper 75-1*, 1975.

[27] Horstman, C and Hung, C., Computation of Three - Dimensional Separated Flows at Supersonic Speeds. *AIAA Paper No. 79-0002*, 1979.

[28] Horstman, C., A Computational Study of Complex Three-Dimensional Compressible Turbulent Flowfields. *AIAA Paper No. 84-1556*, 1984.

[29] Horstman, C., Computation of Sharp-Fin-Induced Shock Wave/ Boundary layer Interactions. *AIAA Paper No. 86-1032*, May 1986.

[30] Knight, D., A Hybrid Explicit-Implicit Numerical Algorithm for the Three-Dimensional Compressible Navier Stokes Equations. *AIAA Journal*, Vol 22, 1984 ,pp. 1056-1061.

[31] Knight, D., Numerical Simulation of 3-D Shock Turbulent Boundary Layer Interaction Generated by a Sharp Fin. *AIAA Journal* Vol 23, December 1985, pp. 1885-1891.

[32] Knight, D., Modelling of Three-Dimensional Shock Wave Turbulent Boundary Layer Interactions. *Lecture Notes in Physics* Vol 230, Springer-Verlag, New York, 1985, pp. 177-201.

[33] Knight, D., Horstman, C. C., Ruderich. R., Mao, M. F and Bogdonoff. S., Supersonic Turbulent Flow past a 3-D Swept Compression Corner at Mach 3. *AIAA Paper No. 87-0551*, January 1987.

[34] Knight, D., Horstman. C., Shapey, B and Bogdonoff, S., The Flowfield Structure of the 3-D Shock Wave Boundary Layer Interaction Generated by a 20 deg Sharp Fin at Mach 3. *AIAA Journal* Vol 25, No 10, October 1987, pp. 1331-1337.

[35] Knight, D., Raufer, D., Horstman, C. C., Ketchum, A and Bogdonoff. S., Supersonic Turbulent Flow Past a 3-D Swept Compression Corner at Mach 3 - Part II. *AIAA Paper No. 88-0310*, January 1988.

[36] Baldwin, B and Lomax, H., Thin Layer approximation and Algebraic Model for Separated Turbulence Flows. *AIAA Paper No. 78-257*, 1978.

[37] Jones, W and Launder, B., The Prediction of Laminarisation with a Two-Equation Model of Turbulence. *Int.J.Heat and Mass Transfer*,Vol 15, 1972, pp. 301-304.

[38] Cebeci, T and Smith, A. M. O., Analysis of Turbulent Boundary Layers. *Academic Press* ,New York, 1974.

[39] Keller, H., Accurate Numerical Methods for Nonlinear Two-Point Boundary Value Problems. *SIAM J. Numerical Analysis, Vol 11*, 1974, pp. 305-320.

[40] Token, K., Heat Transfer due to Shock Wave/ Boundary Layer Interactions on High Speed Weapons Systems. *AFFDL report No. TR-74-77*, 1974.

[41] Gaitonde, D and Knight, D. D., Numerical Experiments on the 3-D Shock Wave- Boundary Layer Interaction Generated by a Sharp Fin. *AIAA paper No. 88-0309*, 1988.

[42] Raufer, D., The Development of a 3-D Particle Tracing Algorithm and its application to The Study Of Swept Compression Corner Boundary Layer Interactions. *M.S Thesis, Rutgers University*, January 1988.

[43] Sun, C. C and Childs, M., Wall Wake Velocity Profile for Compressible Nonadiabatic Flows. *AIAA Journal*, Vol 14, 1976, pp. 820-822.

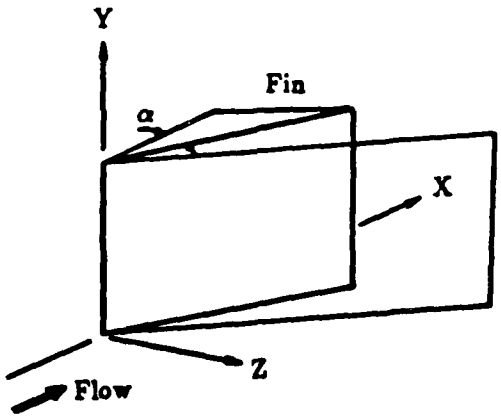

Fig.1 Sharp fin configuration

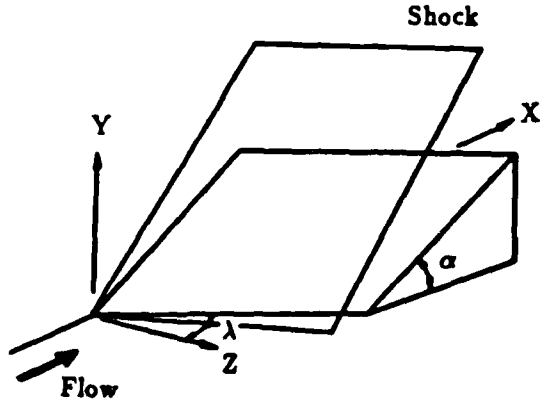

Fig.2 Swept compression corner configuration

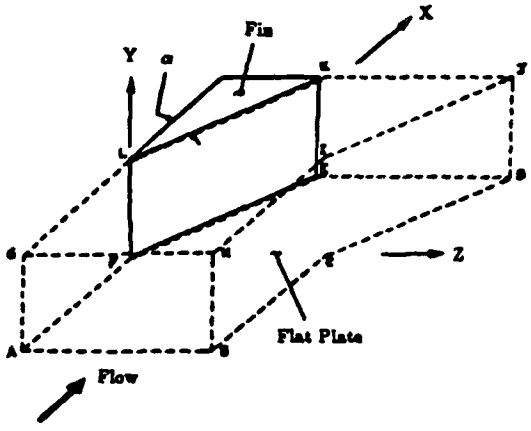

Fig.3 Physical domain for 3-D Sharp fin

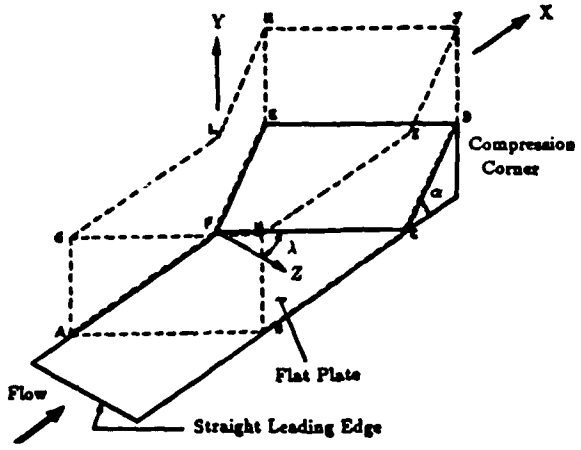

Fig.4 Physical domain for 3-D Swept compression corner

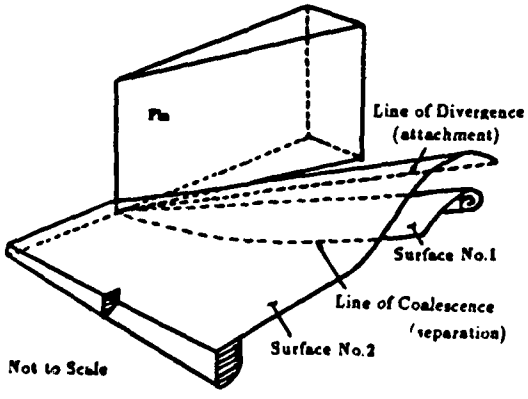

Fig.5 Mean flowfield structure
Sharp fin interaction

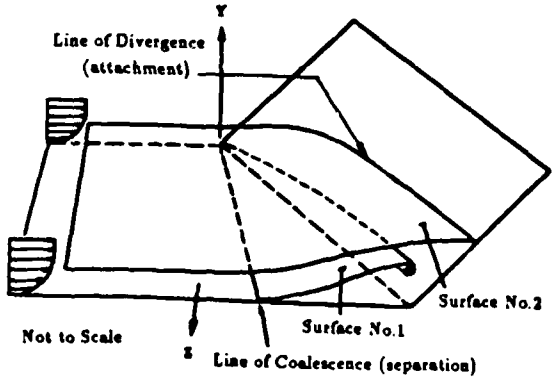

Fig.6 Mean flowfield structure
Swept compression corner interaction

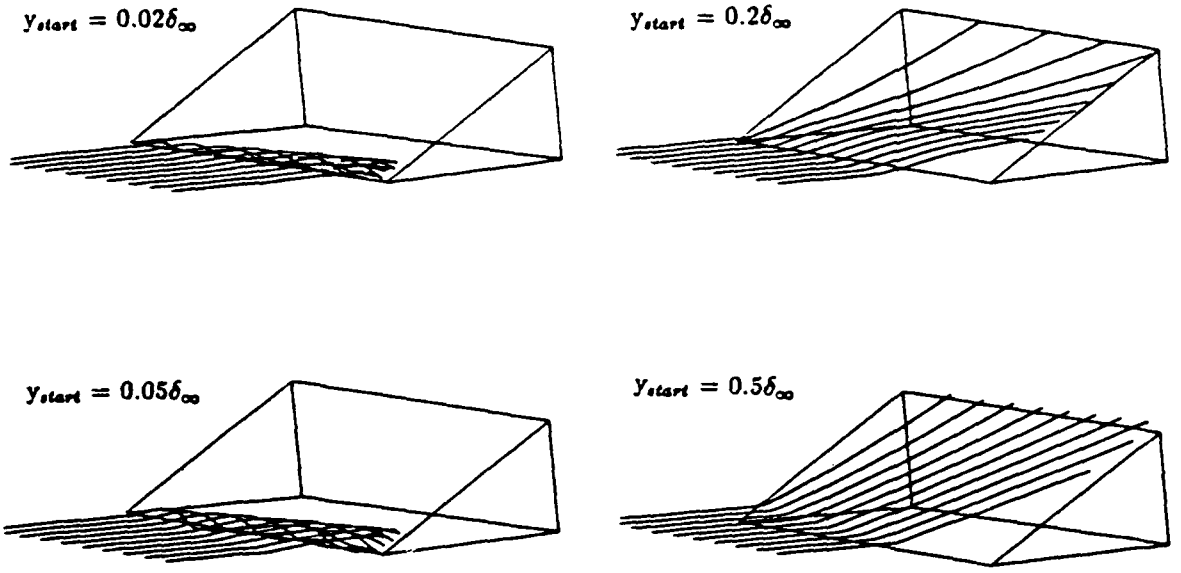

Fig.7 Streamlines for Swept compression corner
$(\alpha,\lambda)=(24,40)$ at $Re_{\delta_\infty} = 8.1\times10^5$
Flowfield generated using the Baldwin-Lomax algebraic eddy-viscosity model

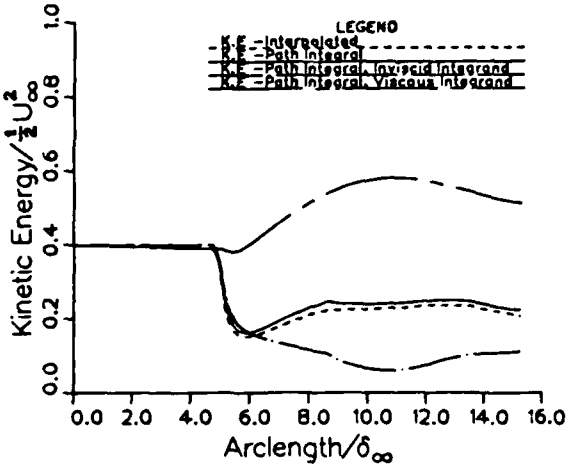

Fig.8 Kinetic energy along streamline originating from y $=0.02\delta_\infty$
Flowfield No.1

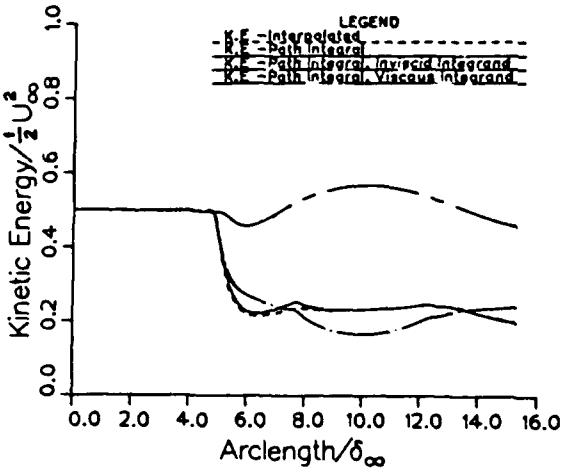

Fig.9 Kinetic energy along streamline originating from y $=0.05\delta_\infty$
Flowfield No.1

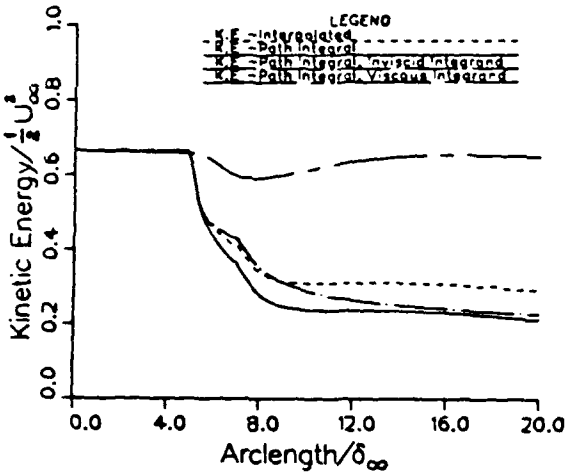

Fig.10 Kinetic energy along streamline originating from y $=0.2\delta_\infty$
Flowfield No.1

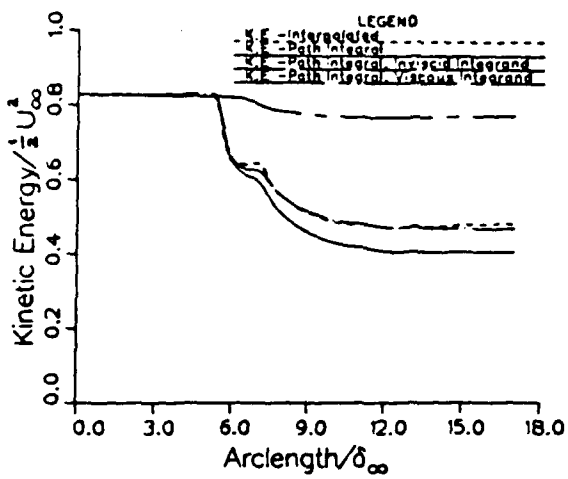

Fig.11 Kinetic energy along streamline originating from y $=0.5\delta_\infty$
Flowfield No.1

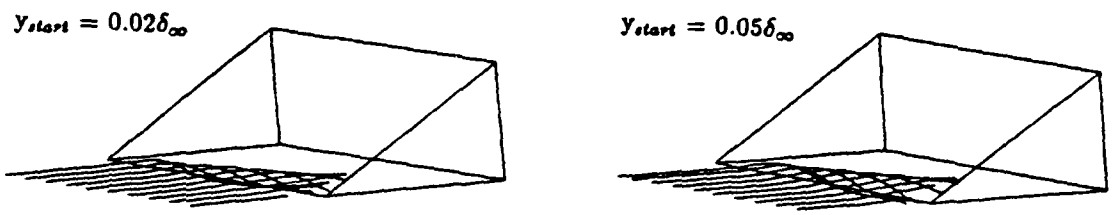

Fig.12 Streamlines for Swept compression corner
$(\alpha,\lambda)=(24,40)$ at $Re_{\delta_\infty} = 8.1\times10^6$
Flowfield generated using the Jones-Launder turbulence model

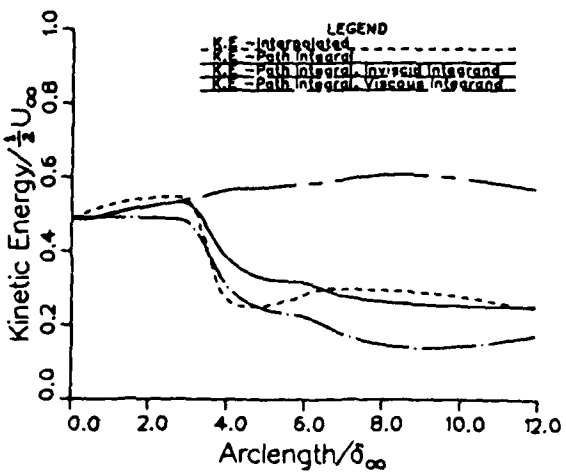

Fig.13 Kinetic energy along streamline originating from y $=0.02\delta_\infty$
Flowfield No.2

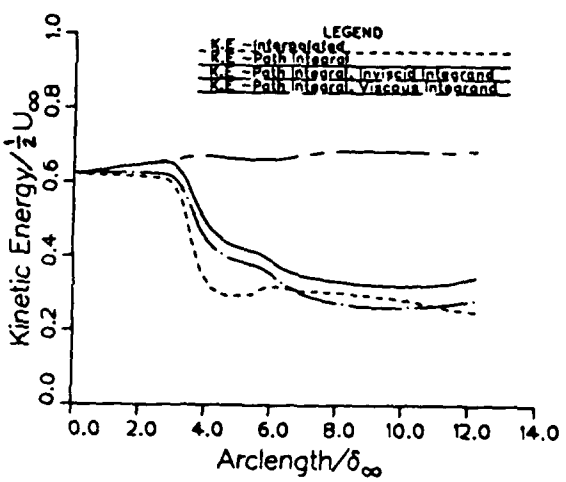

Fig.14 Kinetic energy along streamline originating from y $=0.05\delta_\infty$
Flowfield No.2

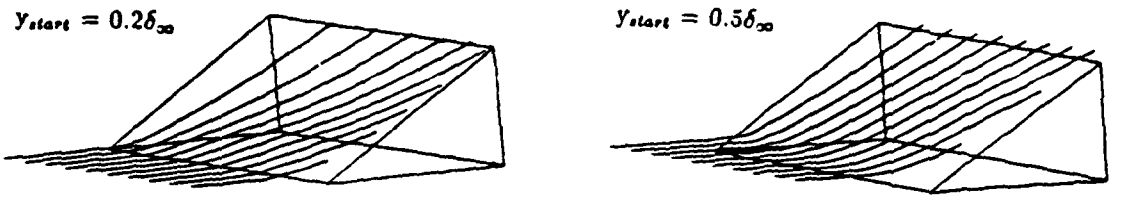

Fig.15 Streamlines for Swept compression corner
$(\alpha,\lambda)=(24,40)$ at $Re_{\delta_\infty} = 8.1\times10^6$
Flowfield generated using the Jones-Launder turbulence model

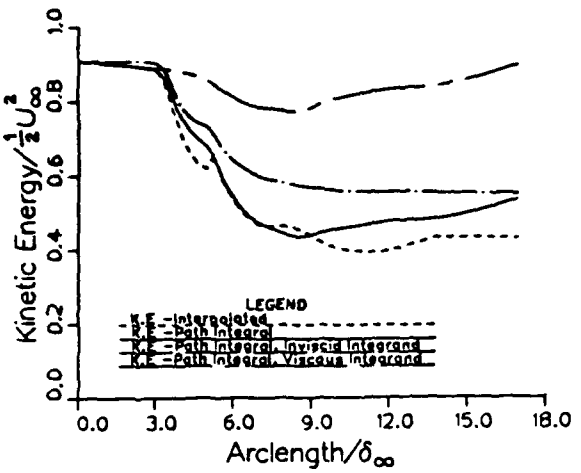

Fig.16 Kinetic energy along streamline
originating from y $=0.2\delta_\infty$
Flowfield No.2

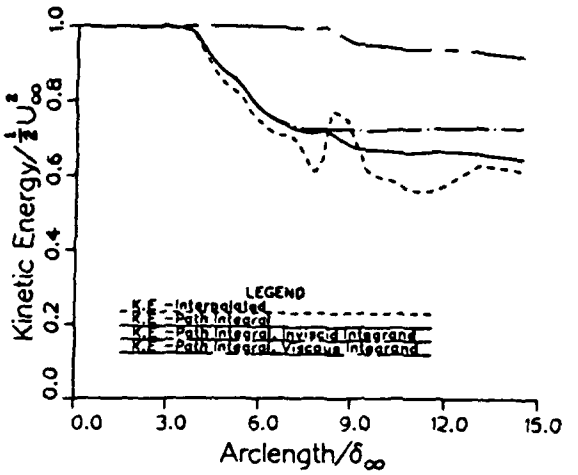

Fig.17 Kinetic energy along streamline
originating from y $=0.5\delta_\infty$
Flowfield No.2

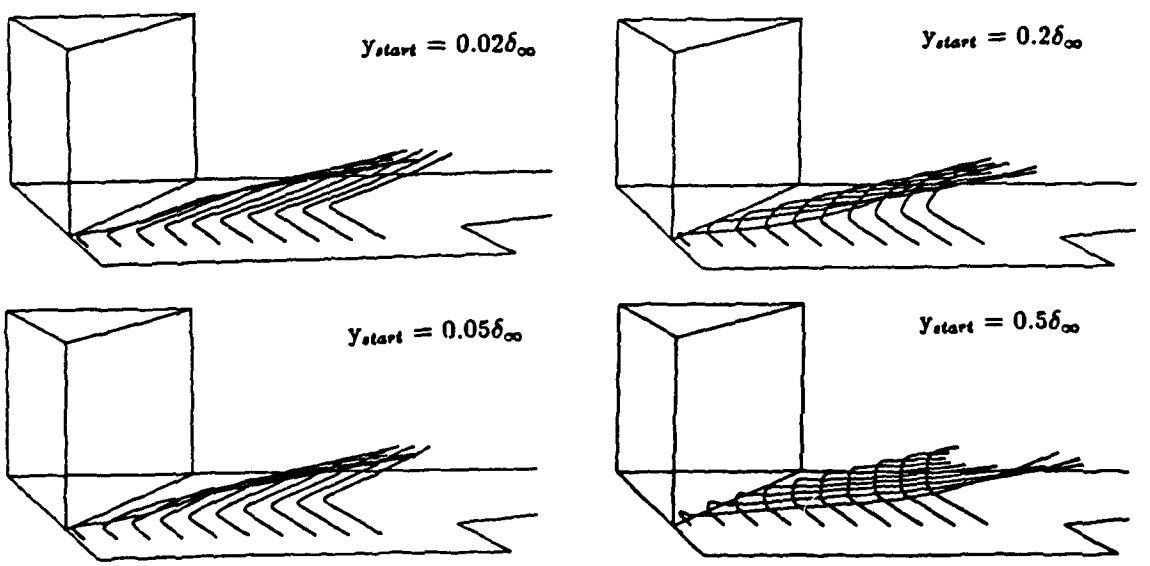

Fig.18 Streamlines for sharp fin configuration
$(\alpha = 20°)$ at $Re_{\delta_\infty} = 9.0\times10^6$
Flowfield generated using the Baldwin-Lomax turbulence model

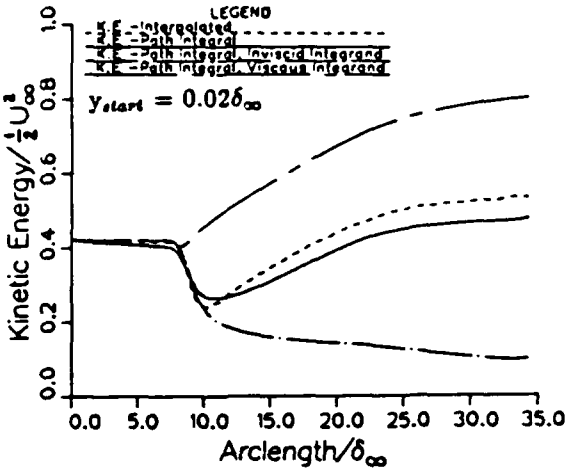

Fig.19 Kinetic energy along streamline
Flowfield No.1, Sharp fin interaction

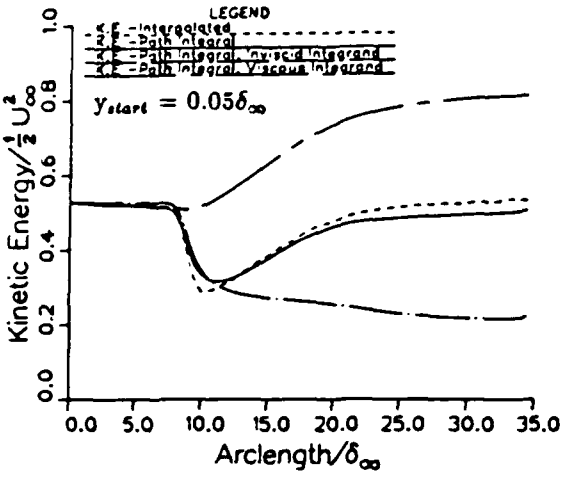

Fig.20 Kinetic energy along streamline
Flowfield No.1, Sharp fin interaction

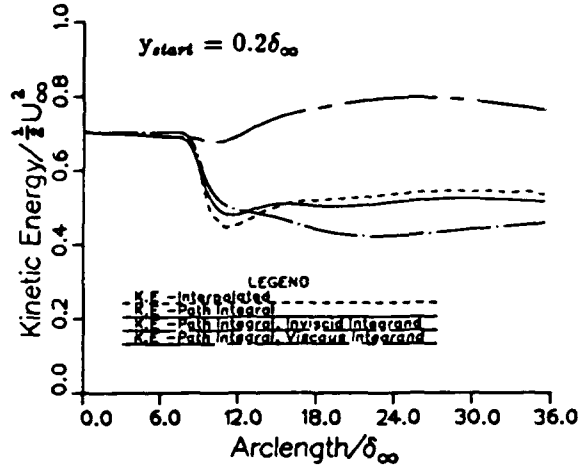

Fig.21 Kinetic energy along streamline
Flowfield No.1, Sharp fin interaction

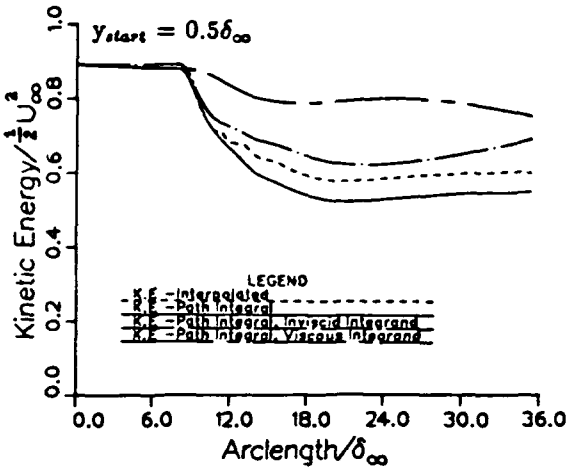

Fig.22 Kinetic energy along streamline
Flowfield No.1, Sharp fin interaction

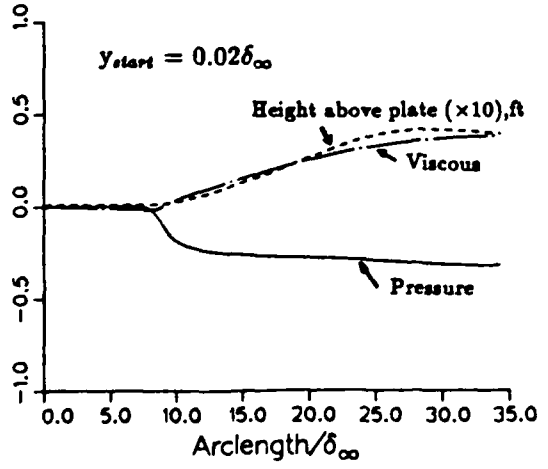

Fig.23 Pressure/Viscous Contribution,Height above plate
Flowfield No.1, Sharp fin interaction

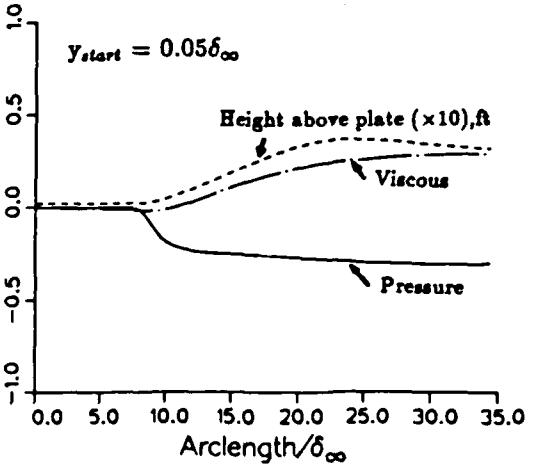

Fig.24 Pressure/Viscous Contribution,Height above plate
Flowfield No.1, Sharp fin interaction

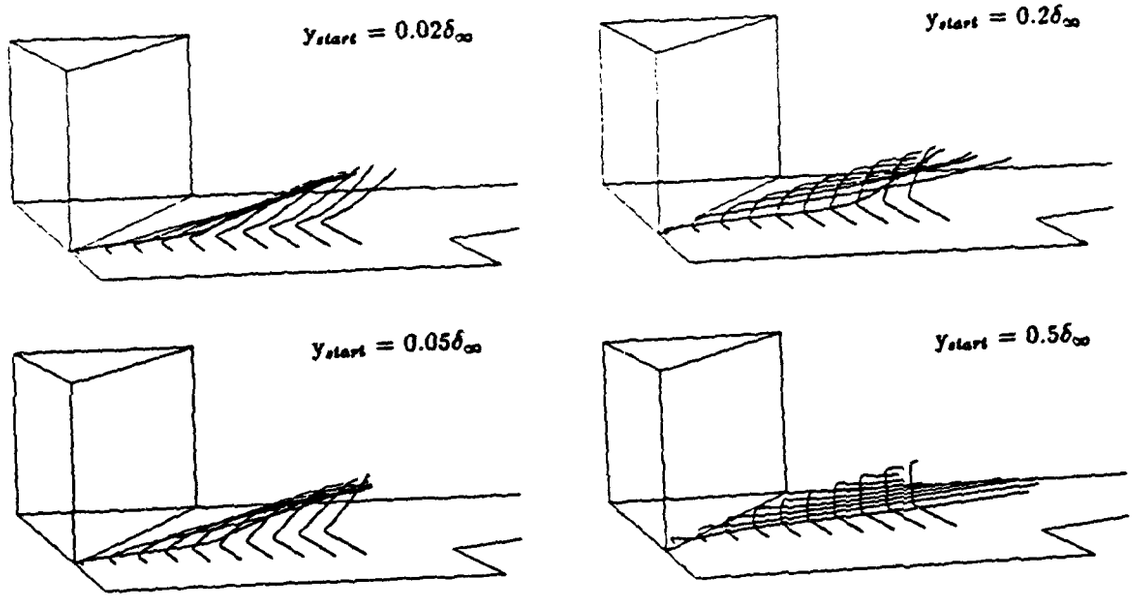

Fig.25 Streamlines for sharp fin configuration
(α =20°) at $Re_{\delta_\infty} = 9.0\times10^6$
Flowfield generated using the Jones-Launder turbulence model

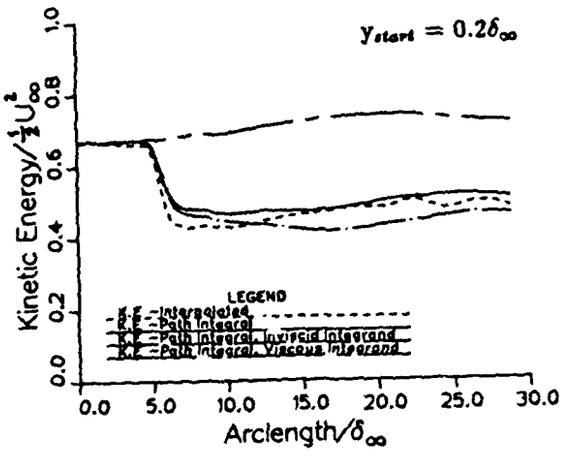

Fig.26 Kinetic energy along streamline
Flowfield No.2, Sharp fin interaction

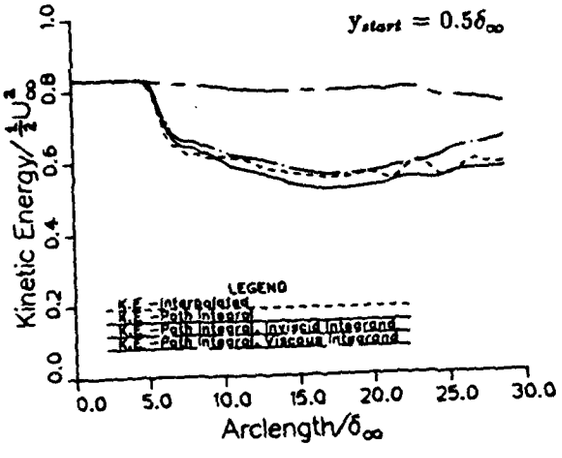

Fig.27 Kinetic energy along streamline
Flowfield No.2, Sharp fin interaction

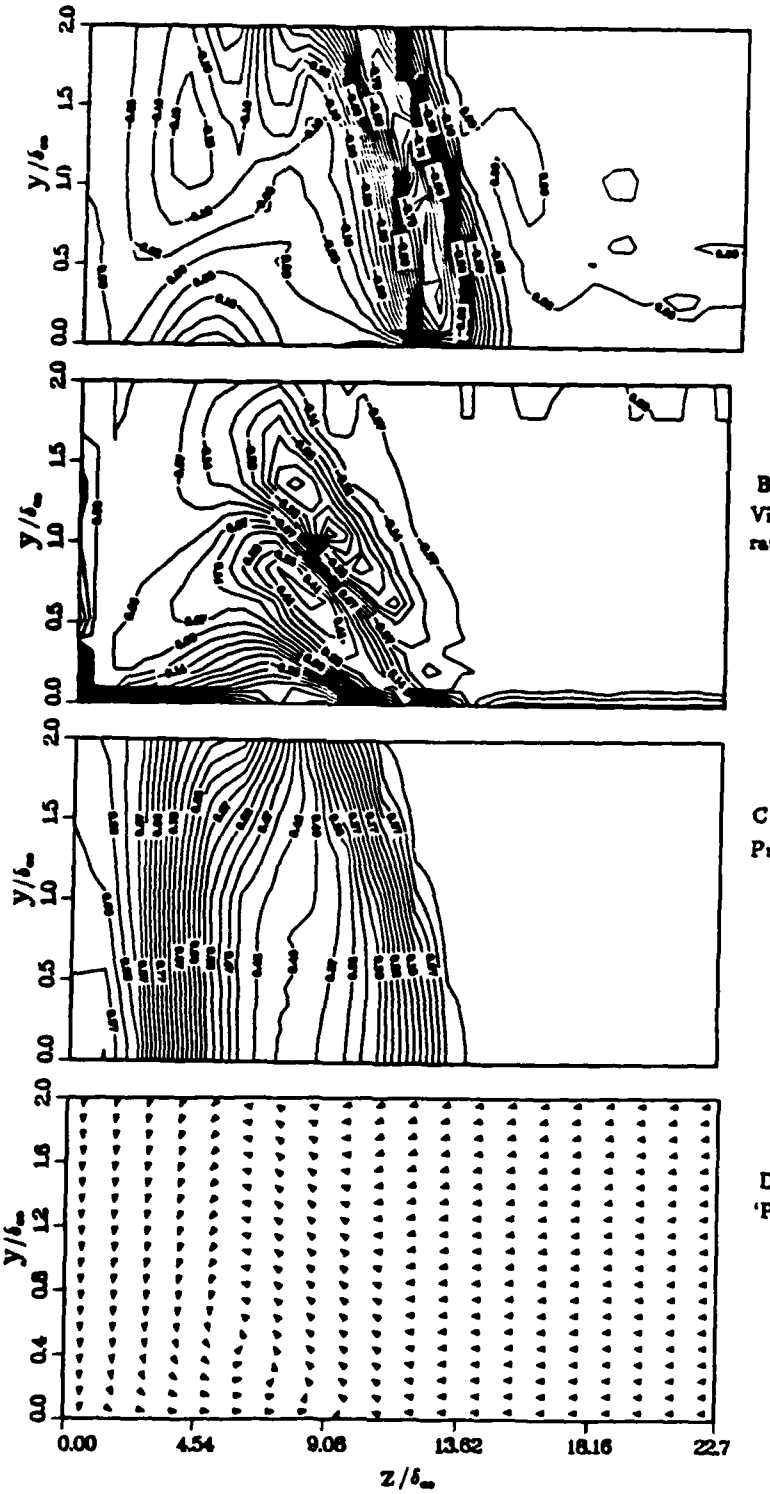

A
Inviscid (pressure) Contribution to rate of change of mean kinetic energy

$$-\left(\frac{u_i}{\rho}\right)\frac{\partial p}{\partial x_i}$$

B
Viscous Contribution to rate of change of mean kinetic energy

$$\left(\frac{u_i}{\rho}\right)\frac{\partial \tau_{ij}}{\partial x_j}$$

C
Pressure contours (p/p_∞)

D
'Polar' Velocity vectors

Fig.28 Inviscid, viscous contribution to rate of change of mean kinetic energy, Pressure contours, 'Polar' velocity vectors at $x = 15\ \delta_\infty$
Flowfield No.1, ($\alpha = 20°$) sharp fin interaction

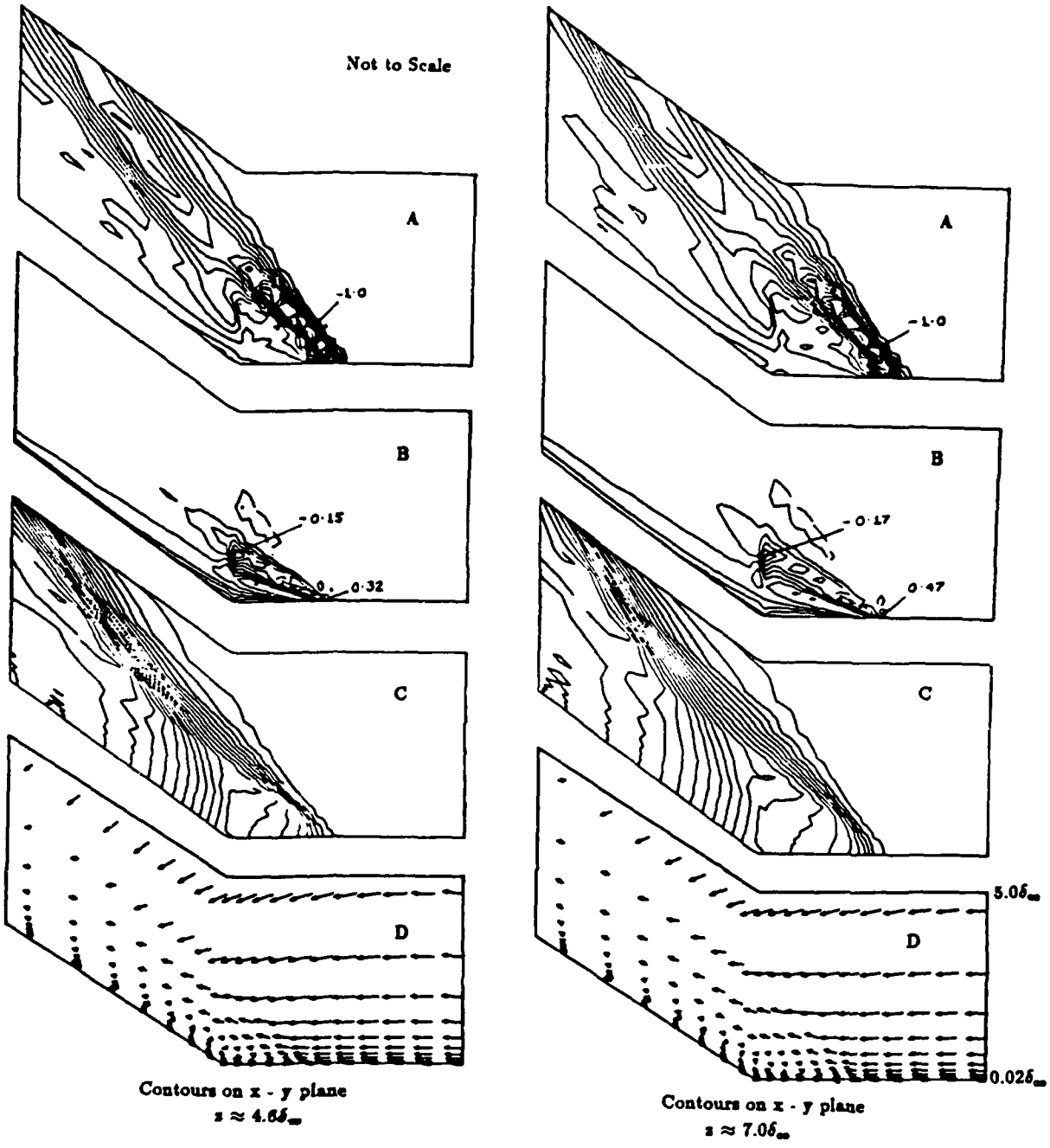

Contours on x - y plane
$z \approx 4.6\delta_\infty$

Contours on x - y plane
$z \approx 7.0\delta_\infty$

A: Inviscid (pressure) Contribution to rate of change of mean kinetic energy

B: Viscous Contribution to rate of change of mean kinetic energy

C: Pressure contours (p/p_∞)

D: 'Polar' Velocity vectors

Fig.29 Inviscid, viscous contribution to rate of change of mean kinetic energy, Pressure contours, 'Polar' velocity vectors
(α,λ)= (24,40)Swept compression corner interaction
Flowfield No.1, Baldwin-Lomax turbulence model

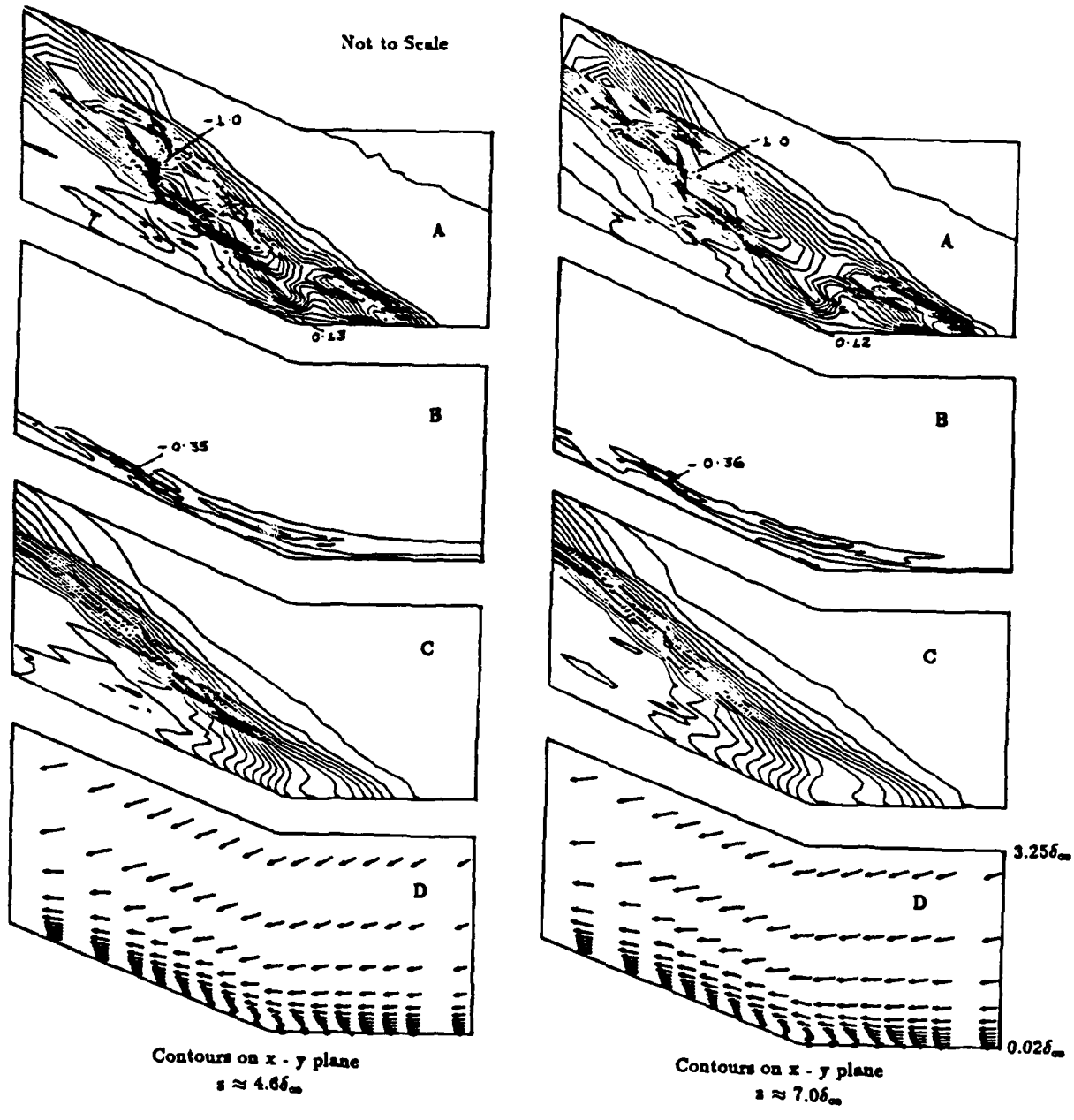

Contours on x - y plane
$z \approx 4.6\delta_\infty$

Contours on x - y plane
$z \approx 7.0\delta_\infty$

A: Inviscid (pressure) Contribution to rate of change of mean kinetic energy

B: Viscous Contribution to rate of change of mean kinetic energy

C: Pressure contours (p/p_∞)

D: 'Polar' Velocity vectors

Fig.30 Inviscid, viscous contribution to rate of change of mean kinetic energy, Pressure contours, 'Polar' velocity vectors
(α,λ)= (24,40)Swept compression corner interaction
Flowfield No.2, Jones-Launder turbulence model